Column base-plates under biaxial bending moment

L. da Silva Seco, Maël Couchaux, Mohammed Hjiaj, L.C. Neves

COLUMN BASE-PLATES UNDER BIAXIAL BENDING MOMENT

Laura DA SILVA SECO[1], Maël COUCHAUX[1,*], Mohammed HJIAJ[1], Luis COSTA NEVES[2]

[1] Structural Engineering Research Group / LGCGM
INSA de Rennes / UEB
20 avenue des Buttes de Coësmes
F – 35708 Rennes
FRANCE

[2] **INESCC** Civil Engineering Department
University of Coimbra,
Coimbra
PORTUGAL

* Corresponding author: Email: mael.couchaux@insa-rennes.fr
Fax: + 33 2 23 23 82 24

Abstract

This paper investigates the behaviour of exposed column base-plates with four outer anchor bolts subjected to monotonic loading. The results of six full-scale tests on steel column base-plate connections subjected to uni/biaxial bending moment are presented. The influence of the base-plate thickness and the bending moment axis orientation on the connection response is thoroughly investigated. In addition to standard measurements, Digital Image Correlation has been used to closely monitor the evolution of the contact area that develops in the tensile and compressive zones. Furthermore, a detailed finite element model has been developed using the software Abaqus and used to explore additional orientations of the bending moment axis. This numerical model allows to investigate the evolution of the anchor bolt forces, the contact pressure distribution and the lever arm, that strongly influence the bending resistance and rotational stiffness. An Analytical model is suggested for the calculation of the bending resistance of a column base-plate connection whatever the orientation of the bending moment axis. The position of the centre of compression directly depends on the base-plate thickness. A plastic redistribution is also considered between the anchor bolt rows when biaxial bending moment is applied to the column base-plate.

1. INTRODUCTION

Column base-plate connections are responsible for transferring loads from the superstructure to the foundations. Their behaviour strongly affect the stiffness and the load bearing capacity of the frames. The column base-plate connection consists of several components: anchor bolts, base-plate, concrete foundation, grouting, stiffeners and shear-lug. All these components interact to produce the connection behavior and have their respective influence on the behavior (strength, ductility ….).

Despite the important role of column base-plate connections and their significant influence on the response of the structure, there has been little interest and less research effort compared to the research work devoted to other types of connections, such as beam-to-column or beam-to-beam. There is an evident lack of information in the litterature on the behaviour of column base-plates subjected to biaxial bending moment. Most of past research studies deal with numerical and/or experimental studies on column base-plates subjected to combined axial force and strong axis bending moment. Only few studies addressed the case of weak axis or biaxial bending moment. Corner column base plates are subjected to biaxial bending moment when seismic/wind loadings are applied to the structure. Gravity loading can also produce this biaxial bending moment particularly in heavy industrial structures.

The first developments on column base-plates started in Europe, early in the 70's. Delesques [1] developed an elastic model to estimate the in-plane bending resistance of column base-plates. Next, Lescouarc'h [2] extended this model to biaxial bending moment. The results of this research work were synthetized in a design guide that has been widely used in France during the last decades. The AISC Steel Design Guide One [3] adopted also an elastic approach for the design of column base-plates under axial force and in-plane bending moment. The new version of Eurocode for mechanical fasteners [4] promotes this elastic design approach too and assumes that the base-plate remain rigid. However, this assumption is realistic only for relatively large base-plate thickness which are not common in practice. Furthermore, the actual contact pressure distribution between concrete and base-plate is far more complex than what has been assumed.

A significant number of research contributions deserve particular attention to a better understanding of the behavior and the performance of column base-plates subjected to major axis bending moment. Picard and Beaulieu [5] carried out an experimental investigation on column base-plates subjected to axial force and bending moment aiming at estimating the influence of the loading on the rigidity of the connection. Jaspart and Vandegans [6] made progresses in the study of the behavior of column base-plates under major axis bending moment by developing a non-linear mechanical model to calculate the moment-rotation curve which was validated against experimental data from the tests performed at University of Liège. Methods that consider plastic distribution for the contact pressure between the base-plate and the concrete block ([7], [8], [9]) were suggested and included in the development of the last generation of design codes for column base-plates ([10], [11]). Ruopp and Kulhmann [12] studied the redistribution between anchor bolts in column base-plates with multiple anchor bolt rows. The above mentioned research and design codes deal with the case of column base-plates under strong axis in-plane bending moment combined with an axial force. During the last two decades, research progress on column base-plates subjected to out-of-plane bending moment has been achieved. Lee et al. ([13], [14]) studied experimentally and numerically column base-plates subjected to weak axis bending moment and highlighted that the application of the Drake and Elkin approach [7] is not adequate for this case. Since failure occurred by elastoplastic local buckling of the column flanges or weld cracking, the test results of Lee et al. [14] cannot be used to calibrate an analytical model that provide the out-of-plane bending resistance of the connection. Bajer et al. [15] performed the first experimental tests on column base-plates subjected to axial force and biaxial bending moment. Unfortunately missing mechanical characteristics of steel components restrict their use in benchmarking analysis. As expected the nature of loading has an influence on the moment resistance and rotational stiffness of the connection. In fact, under biaxial bending moment, the moment resistance and rotational stiffness are inferior to values obtained under strong axis bending moment. However, the failure mode is unchanged and correspond to anchor bolt rupture in tension. Amaral [16] developed a finite element model that was able to reproduce the test results of Bajer et al [15] with good accuracy. She suggested an analytical model based on the component method to evaluate the out-of-plane bending moment resistance in presence of an axial force. It was

assumed that the extend of the compressive area depends on the axial force applied to the connection. In addition, an elliptical interaction curve was proposed for biaxial bending moment. The results of the analytical model were quite conservative compared to their numerical and experimental counterparts. Fasaee et al. [17] performed numerical studies of column base-plates under axial force and biaxial bending moment and confirmed the relevance of the elliptical interaction curve. To fully understand the interaction between strong and weak axis bending moments, a more rigorous and general approach seems necessary.

This paper investigates the behaviour of exposed column base-plates with four outer anchor bolts subjected to monotonic loading and focuses on the bending resistance, initial rotational stiffness and rotation capacity, through a campaign of six experimental tests. The main variables are the base-plate thickness and the loading conditions: major/minor axis bending moment and biaxial bending moment. The following inclinations of the bending moment axis are considered: 0° (strong-axis), 45° and 90° (weak-axis). The effect of the axial force is not investigated in this paper. Image correlation is used to follow the base-plate deformation and thus the modification of contact area in tensile and compressive zones and therefore the evolution of prying effect. In addition, a sophisticated finite element model has been developed in Abaqus to simulate the behaviour of the six connections tested and to get informations that are not accessible. To extend the scope of experimental tests, additional inclinations of the bending moment axis have been considered. Key data obtained numerically are the anchor bolt force, contact pressure distribution and thus position of the centre of compression. Finally, an analytical/design model is proposed to determine the bending resistance of a column base-plate connection whatever the orientation of the bending moment. For biaxial bending moment, a plastic redistribution of out-of-plane bending moment is retained. A particular attention is dedicated to estimate the actual position of the centre of compression for every orientation of the bending moment.

2. EXPERIMENTAL PROGRAMM

The main objective of this research work is to better understand the influence of the base-plate thickness and the bending moment axis orientation on the bending resistance, initial rotational stiffness and rotation capacity of exposed column base-plates. The first phase of this investigation included testing of six full-scale steel column base-plate connections. The tests were performed at the Laboratoire de *Génie Civil et Génie Mécanique* – INSA at Rennes. Base-plates were fastened to the concrete foundation by means of 4 anchor bolts without any addition of grout or embedded plates. Therefore, the base-plates were in direct contact with the concrete block.

2.1. Test set-up

The column base specimen was attached to a concrete block by four anchor bolts and placed horizontally, working as a cantilever beam. The test set-up was designed to accomodate all loading combinations with a single vertical hydraulic jack applying load in the downward direction. The load-jack was placed at a distance of 1250 mm from the concrete block (see Fig. 1). The concrete foundation is maintained at the front and the back by two rectangular steel frames. On the front side, the concrete block is placed directly on two neoprene supports resting on the lower beam of steel frame A. At the back (portal frame B), rollers are welded to a load distribution plate positioned on the concrete block (see Fig. 1). Lateral supports located at mid-length of the column were used to prevent lateral torsional buckling of the steel profile. As discussed above, specimens were subjected to three different loading cases: pure bending moment about the strong axis, pure bending moment about the weak axis and biaxial bending moment with an orientation of the bending moment axis of 45°. To ease the load application for the last two loading cases, a specific test set-up was devised in which the column is divided into equal-length sections along the length. The part of the column attached to the load jack was left as for the case of pure bending moment about the strong axis. To produce pure bending moment about the weak axis or biaxial bending moment, the second part of the column which is attached to the concrete block is rotated by 90º (weak axis bending) and 45º degrees (biaxial bending). These two sections were connected by two bolted circular flanges with eight preloaded bolts HR M20 class 10.9. Lateral plates were placed at the free end of the

column and directly welded to the circular plate. This not only prevents lateral torsional buckling but also transforms the column open cross-section into a closed and stiffer cross-section ensuring effective force transfer to the base plate and preventing local cross-section deformation.

Fig. 1. *Test set-up for uniaxial and biaxial bending moments*

2.2. Geometry of the tested specimens

All specimens consisted in a column steel profile HEA 200 welded to a rectangular base-plate 330×300 mm by fillet welds with 7 mm throat thickness. The base-plate was anchored to a concrete block (1450×900×610) of C25/30 class (EN1992) by means of four outer anchor bolts M16 class 5.6 (see Fig. 2).

Fig. 2. *Tested column base-plate configuration (dimensions in mm)*

The embedded anchor bolts were connected to the concrete block by 50×50×10 mm washers. The geometry and mechanical characteristics of the specimens are given in Table 1. For convenience, a label was given to each specimen in a way that the base-plate thickness and the inclination of the applied bending moment axis with respect to the strong axis can be identified. The label comprises capital letters *SPE* followed by a number indicating the base-plate thickness (1 for 10 mm and 2 for 20 mm). The loading is identified by the letter M followed by a number specifying the inclination of the applied bending moment axis, *M0* for in-plane bending moment, *M90* for an out-of-plane bending moment and *M45* for biaxial bending moment. Considering two base-plates thicknesses (10 and 20 mm) gives the opportunity to evaluate the impact of the base-plate flexibility on the performance of the column-base including the failure mode. The concrete block was adequately reinforced to cope with the applied loads. The steel reinforcement is a mesh ST 25C with 6 HA10 S500 steel grade (EN 1992) placed near the top and bottom surfaces of the concrete block. The concrete cover is 25 mm. Additional C-shape plain round bars were placed in the supports zones to prevent concrete cone failure. Shear reinforcement was also added near the supports. More details about the reinforcement features may be found in [24]. Grout mechanical properties being highly sensitive to the grouting technique and considering that the

objective of the present study was to deeply investigate the behavior of steel components, column base-plates were fastened without grout. Effect of grout is left to future research. Bajer et al [15] performed repeat tests on column base plates involving failure of steel components but also substantial concrete cracking. The bending resistance deviation was close to 5 %. In the present test campaign, concrete block was overdesigned to avoid concrete cracking and we observed pure steel failure modes whose deviation is limited. Repeat tests have thus been excluded.

Table 1 : *Column base-plates tested*

Test ID	Loading conditions	Column profile	Column steel grade	Base-plate thickness t_p (mm)	Base-plate steel grade
SPE1-M0	In-plane bending	HEA 200	S355	10	S275
SPE2-M0	In-plane bending			20	
SPE1-M90	Out-of-plane bending			10	
SPE2-M90	Out-of-plane bending			20	
SPE1-M45	Biaxial bending			10	
SPE2-M45	Biaxial bending			20	

2.3. Instrumentation

Each specimen was instrumented to obtain the strain, displacement and force measurements necessary to accomplish the goals of the experiments. Deformation of the specimen was monitored using seven LVDT's (linear variable differential transducer) placed at several locations on the specimen. The sensor V_1 was placed underneath the load application point at 1085 mm from the concrete surface. In addition, deflections of the column were measured using three potentiometers V_2, V_3 and V_4 located along the length of the specimen and were placed at 685 mm, 285 mm from the concrete surface and immediately at the base-plate, respectively. Potentiometers V_5, V_6 and V_7 were installed below the concrete block at 100 mm, 325 mm and 1125 mm from the front surface of the concrete block, respectively. The measurements provided by these sensors were used to compute the concrete block rotation θ_c. For specimens SPE1-M45 and SPE2-M45, the part of the column steel profile welded to the base-plate is rotated by 45° and sensor V_3 may give inaccurate results because of its location. Therefore the displacement given by sensor V_3 was not considered for this loading case. Horizontal transducers

U_{t1}, U_{t2}, U_{b1} and U_{b2} were placed on the column flanges and measured the uplift displacement of the base-plate in the tensile zone and the crushing deformation in the compressive zone. The location of these devices is depicted in Fig. 3. Vertical forces were applied to the structure by a SCHENCK load-jack with capacity ± 1500 kN (see Fig. 3).

Fig. 3. *Displacement sensors arrangement*

Additionally, for specimens SPE1-M90 and SPE2-M90, a total of eight strain gauges were pasted on the steel profile flange, four on each external face of the HEA 200 flanges. The strain gauges were positioned at a distance of 20 mm from the welds, where high stress concentration due to redistribution of the forces between the compressive and tensile parts was expected. The longitudinal distance between the strain gauges is 50 mm. Fig. 4 shows the the strain gauges locations for tests SPE1-M90 and SPE2-M90.

Fig. 4. *Position and designation of the strain gauges*

Digital image correlation (DIC) is an efficient technique for non-contact full-field strain measurement that has been used to approximate the deformed shape of the base-plate and to evaluate the relative displacement between the concrete block and the base-plate. Automated image registration at every 30 seconds produced a large set of overlaying images that were then processed with the digital image correlation GOM Correlate program. All images were taken from the same viewpoint. The outputs are an estimation of the horizontal displacements of surface points (markers) located over the base-plate. These results were used as supplementary information for the evaluation of the area of the compressive and tensile zones and a better understanding of the development of prying effect. The lateral initial gaps due to heat effect produced by the welding process (see Fig. 6) were also recorded for specimens SPE1-M0/90, SPE2-M0/90 after the erection of the connection.

a- Side of the base-plate *b- Top of the base-plate*

Fig. 5. *Markers placed on the side/top of the base-plate (M90) and at the concrete surface*

The initial imperfections of SPE1-M0 are quite substantial particularly near the free edges as a result of thin base-plates being more sensitive to deformations induced by heat effect during welding process. These important initial uplift deformations will have an impact on the onset of the prying effect. For SPE2-M0, there is no initial gap and the base-plate is initially in full contact with the concrete block. For SPE1/2-M90, the initial imperfections correspond to a rather homogeneous gap between the base-plate and the concrete block. For SPE1-M90, this distribution is less homogeneous.

a- SPE1-M0 and SPE2-M0 *b- SPE1-M90 and SPE2-M90*

Fig. 6. *Initial gaps of the side of the base-plates for SPE test series*

This difference comes from the kinematic constraint enforced by the column flanges. In addition, the displacement at the top surface of the base-plate of specimens SPE1-M90 and SPE2-M90 was measured during the test using image correlation (see section 2.6.3).

2.4. Material properties

Steel coupons cut from the column web/flange, the base-plates and anchor bolts (3 coupons per samples) after completion of tests were tested under monotically increasing displacement until rupture according to EN 10002-1: 2001. Column, base-plate and anchor bolt coupons were extracted from the same batch used to fabricate the connections tested. An extensometer was used at the mid-gage of the samples to read the displacements. The rate of the loading (displacement-controlled) was equal to 1,26mm/min. The reference length for evaluation of elongation was equal to 50 mm. The average mechanical properties of steel components deduced from tensile tests are summarized in Table 2. Regarding concrete material, standard compression test on cylindrical concrete core samples were performed according to EN 12390-3.

Table 2 : *Average material properties of steel components*

Component	Elasticity modulus	Yield strength	Ultimate strength	Necking	Elongation
-	N/mm^2	N/mm^2	N/mm^2	(%)	(%)
Base-plate 10 mm	213122	423,6	512,7	70	37
Base-plate 20 mm	209288	401,3	503,1	71	30
Column web	210000(1)	378,4	457,3	60	25
Column flange	211691	350,1	433,3	69	34
Anchor bolts M16	208295	519,1(2)	626,8	72	9

Note 1. This value corresponds to the nominal one as the measured value was not coherent
Note 2. Defined as the value corresponding to ε = 0,2%.

For both the column and the base-plates, the yield and ultimate strengths are higher than the nominal properties provided by EN 1993-1-1. The tested samples revealed adequate material ductility, fulfilling the minimum requirements established by EN 1993-1-1. Concerning the anchor bolts, the maximum yield strength is higher than the predicted nominal value estimated at 300 MPa. The necking phase was quite substantial and of the same order of magnitude as for the column and base-plates, demonstrating the adequate ductility of the anchor bolts. A concrete class C25/30 was used for the concrete blocks. The concrete compressive strengths are summarized in Table 3.

Table 3 : *Concrete compressive strengths*

Test ID	Time	f_{cm}
-	day	N/mm^2
SPE1-M0	43	28,6
SPE2-M0	41	28,2
SPE1-M90	51	30,4
SPE2-M90	48	29,5
SPE1-M45	79	33,3
SPE2-M45	70	32,3

2.5. Testing procedure

Specimens were subjected to a monotonically increasing vertical force producing either unidirectional bending moment or biaxial bending moment. All specimens were tested under displacement controlled loading. The loading rate was equal to 1mm/min during the elastic stage and increased during the plastic stage. More details about the loading rate may be found in [24]. For a full assessment of the behavior of each connection component and a better understanding of the load transfer between these components during testing, it was decided to di-

vide the loading into an elastic and plastic phases. The magnitudes of the applied load for each phase are reported in Table 4.

Table 4 : *Maximal forces applied during tests*

Test ID	Applied vertical force (kN)		
	Elastic phase 1	Elastic phase 2	Final phase
SPE1-M0	7,5	15,0	37,6
SPE2-M0	10,0	25,0	42,1
SPE1-M90	6,0	12,0	28,9
SPE2-M90	8,5	20,0	35,0
SPE1-M45	7,5	15,0	34,2
SPE2-M45	10,0	20,0	41,1

The load range applied to the specimen during the first phase was estimated by ensuring that the connection remain elastic. The elastic phase consisted in three equal amplitude loading-unloading cycles with the load magnitude being equal to 50% of the design resistance F_{Rd} and a fourth cycle where the load is increased to the full design resistance obtained from EN 1993-1-8. The design resistance F_{Rd} produces a bending moment equal to $2/3M_{j,Rd}$ which corresponds to the theoretical elastic limit in Eurocode 3 Part 1-8. In the final phase, specimens worked in the plastic domain and were loaded until failure of one or more connection components.

2.6. Test results

2.6.1. Failure modes and moment-rotation curves

Test results are now analyzed and major findings from the experimental program in terms of mechanical properties of the connections are discussed. For that, the moment-rotation curves for all specimens are illustrated in Fig. 7. The bending moment M was calculated using the following expression:

$$M = F \times L \tag{1}$$

where F is the vertical force and L the distance between the load application point and the concrete block.

The rotation θ_j of the connection was calculated for M0 and M90 specimens based on the displacements provided by LVDT's as follows:

$$\theta_j = \frac{U_t - U_c}{z_{col}} \tag{2}$$

where U_t is the average of the horizontal displacement measured by U_{t1} and U_{t2} (see Fig. 3), U_b the average of the horizontal displacement measured by U_{b1} and U_{b2} (see Fig. 3), z_{col} the height of the column cross-section for in-plane bending moment and the width of the column flanges for out-of-plane bending moment.

This calculation of θ_j using Equation (2) is no longer valid for cases M45. The values given by U_t and U_b should be replaced with those of U_{t2} and U_{b1}, respectively. The parameter z_{col} is considered as the distance between the corners of the upper and lower column flanges.

Fig. 7. *Moment-rotation curves of the tested connections*

The plastic bending moment $M_{j,pl}$, the ultimate bending moment $M_{j,u}$, the initial rotational stiffness $S_{j,ini,}$ the rotation capacity $\theta_{j,u}$ and the failure modes are summarized in Table 5. To define the yield point and consequently $M_{j,pl}$ and $S_{j,ini}$, the method proposed by ECCS requirements n°45 [18] was used. For that, the tangent to the moment-rotation curve at the origin is drawn, the slope of which is taken as $S_{j,ini}$. Next, a straight line with a slope equal to $S_{j,ini}/10$ and tangent to the moment-rotation curve is drawn. The yield point corresponds to the intersection point between these two straight lines. Values of $\theta_{j,u}$ are obtained by the intersection of the moment-rotation curve in Fig. 7 (after $M_{j,u}$) with a straight horizontal line at $0{,}8M_{j,u}$. For some cases, this intersection point does not exist and $\theta_{j,u}$ is considered to be equal to the maximum value reached during the test.

Table 5 : *Initial rotational stiffness, resistances, failure modes and rotation capacities*

Test	$S_{j,ini}$	Yielded elements	$M_{j,pl}$	$M_{j,u}$	$M_{j,u}/ M_{j,pl}$	$\theta_{j,u}$	Failure mode
-	kNm/rad	-	kNm	kNm	-	mrad	-
SPE1-M0	4117	Anchor bolts/base-plate	37,7	43,2	1,15	44,7	Anchor bolt (one)
SPE2-M0	7190	Anchor bolts	42,9	48,5	1,13	33,2	Anchor bolts (two)
SPE1-M90	2029	Anchor bolts/base-plate	28,2	33,3	1,18	69,5	Anchor bolt (one)
SPE2-M90	3120	Anchor bolts/column	35,9	40,2	1,12	48,1	Anchor bolt (one)
SPE1-M45	2440	Anchor bolts/base-plate	32,0	39,4	1,23	62,7	Anchor bolt (one)
SPE2-M45	3205	Anchor bolts	36,6	47,3	1,29	54,8	Anchor bolt (one)

From the curves depicted in Fig. 7 and Table 5, it can be concluded that the plastic/ultimate bending moments and the initial rotational stiffness strongly depend on the loading case and on the base-plate thickness. For cases with thicker base-plates, the plastic/ultimate bending moments and initial rotational stiffness are higher whatev-

er the orientation of the bending moment axis. Minor-axis bending moment was the most severe loading case in terms of plastic/ultimate bending moments and initial rotational stiffness for both base-plate thicknesses. For this loading case, the difference between the maximum bending moments obtained for each thickness was approximately 20%. Indeed, the initial rotational stiffness for the 20 mm base-plate thickness configuration is approximately twice that of 10 mm base-plate thickness. This is due to the fact that an increase of the base-plate thickness results in a more rigid behavior of the connection. The nature of the base-plate behavior during the tests has a strong influence on the position of the centre of compression. Fig. 8 illustrates the fact that if the base-plate thickness is higher and hence more rigid, the centre of compression tends to move away from the footprint of the compressed column flange towards the edge of the base-plate. On the other hand, for thinner and more deformable base-plates, the compression zone tends to develop near the column flange leading to a shorter distance between $F_{c,Rd}$ and $F_{t,Rd}$. These results will be confirmed quantitatively by the FE model presented in section 3.3.3 and the results of Image Correlation in section 2.6.3.

Fig. 8. *Variation of the position of $F_{t,Rd}$ and $F_{c,Rd}$ according to the base-plate thickness*

The loading case also influences the main characteristics of the moment-rotation curves. Test results revealed that specimens subjected to major-axis bending moment (M0 series) develop greater bending moment resistances and initial rotational stiffness (see Table 5). On the other hand, specimens under minor-axis bending (M90 series) exhibited the lowest bending moment capacity and the initial rotational stiffness are concerned. In all cases, connection failure was trigged by anchor bolt failure in tension with or without base-plate yielding in bending. The main difference lies in the lever arm between the centre of tension and the centre of compression. This lever arm is shorter for M90 series than for M0 series and thus the bending moment resistance decreases for the same tensile resistance of the anchor bolts.

Fig. 9. *Variation of the position of $F_{t,Rd}$ and $F_{c,Rd}$ according to bending moment orientation*

The contribution of the base-plate thickness to the rotation capacity is substantial. In specimens with a thick base-plate, yielding of the anchor bolts may occur before yielding of the base-plate which develops smoothly with the formation of a yield line along the base-plate in the compressive side parallel to the column flange. The direction of application of the bending moment also influences the rotation capacity of the connection. Test results show that despite the larger bending moment resistance and initial rotational stiffness of specimens subjected to major-axis bending (M0 series), lower rotation capacity was observed. On the other hand, specimens subjected to minor-axis bending (M90 series) exhibit the largest rotation capacity.

a- SPE1-M0 *b- SPE1-M90* *c- SPE1-M45*

d- SPE2-M0 *e- SPE2-M90* *f- SPE2-M45*

Fig. 10. *Specimens at failure*

For the six specimens, failure was trigged by rupture of one or two anchor bolts in tension accompanied by yielding of the base-plate in bending for SPE1 series. Substantial necking was observed, contributing to the development of large rotation capacity even for SPE2 series. Prying effect did not develop during the tests of SPE2 connections as the base-plate was rigid. For SPE1-M0 prying effect was not observed mostly due to the initial gap (see Fig. 6-a) and the rotation of the connection. For SPE1-90, this rotation of the connection was not affecting the tensile anchor bolt rows and initial gap was less pronounced. Prying appears during loading and disappear at the necking phase of anchor bolts. The anchor bolt of SPE1-M45 with the highest tensile force was not subjected to prying effect contrary to the others. This difference is explained by the rotation of the connection that impacted mainly the upper anchor bolt.

We can also observe that, for specimens under biaxial bending moment, the ratio between the ultimate bending resistance and the plastic bending resistance is larger than that for specimens subjected to unidirectional bending. This difference results from the redistribution of the anchor bolt forces that favor strain hardening. The strain hardening branch is longer for these specimens (see Fig. 7).

2.6.2. Column flange strain distribution

The evolution of the longitudinal strains measured on the column flanges of specimens SPE1-M90 and SPE2-M90 is presented in Fig. 11. The positions of the strain gauges along the column flanges with their corresponding labels and the location of the plastic neutral axis are given in Fig. 4. Strains obtained from strain gauges SG_l4, SG_r4 of specimen SPE1-M90 and SG_r4 of specimen SPE2-M90 are negative as they are located in the compressive zone of each column flanges. Concerning SG_r3 of specimen SPE2-M90, negative values of the strain were measured for forces below 30 kN whereas positive values were recorded for larger values of the applied force corresponding to anchor bolt yielding. This change of the stress sign is the result of the evolution of the relative stiffness between the tensile and compressive parts of the connection. With the yielding of anchor bolts, the tensile parts become more flexible and thus the size of the compressive area decreases. It can also be noticed that this decrease of the compressive area increases the stress concentration and favour yielding of the compressed cross-section corners. The assumption of linear strain distribution of the beam theory seems more or less valid at the beginning of the loading.

a- SPE1-M90 *b- SPE2-M90*

Fig. 11. *Strain evolution at the bottom of the column flanges*

A similar phenomena is observed with SG_l3 of specimen SPE1-M90 but the strain became positive for a lower force level (10 kN). The initial preloading of anchor bolts favors this initial distribution of stresses. Once the effect of preloading is mitigated, ¾ of the column width works under tension. This phenomena appears earlier in specimen SPE1-M90 than in specimen SPE2-M90 as the tensile part of the former is more flexible. Even if the tensile area increases during the test, yielding of its edge is observed. This effect is a consequence of the low flexibility of the base-plate. The tensile stresses are thus located around the upper anchor bolts.

a- SPE1-M90

b- SPE2-M90

Fig. 12. *Strain and stress distribution along the column flange*

2.6.3. Lateral displacements

The evolution of the lateral displacements is presented for connections tested under in-plane and under out-of-plane bending moments in Fig. 13 and Fig. 14, respectively. For SPE1-M0, the displacement of the base-plate is quite substantial in the tensile area (see Fig. 13-a) and a yield line develops close to the tensile beam flange. After failure, bending residual deformations of the base-plate were clearly observed which confirm the yielding of the base-plate. Once F_{max} is reached, the anchor bolts began to elongate excessively until failure. This phenomenon can be captured from the evolution of the base-plate deformation. In the lower part, the initial gap was closing during loading until full contact with the concrete foundation was achieved. At the beginning of the loading, uplift initiates somewhere between 90 mm and 120 mm from the bottom of the base-plate, the bottom beam flange being at 70 mm from this point. The contact area developed also over the entire area of the bottom extended base-plate but also over about 25% of the column cross-section depth. This uplift point moves down when yielding starts to develop in both the base-plate and the anchor bolt as a result of the modification of the ratio between the stiffness of compressive components and the stiffness of the tensile components. Once the maximum force is reached, the contact area extends towards the base-plate edges. It can also be observed that in the tensile area the inflection point is not located at the weld toe as preconized in EN 1993-1-8 but behind the upper beam flange.

a- SPE1-M0 *b- SPE2-M0*

Fig. 13. *Evolution of the lateral displacement under in-plane bending moment*

In the tensile area, the base-plate of specimen SPE2-M0 remains rigid during the whole test (see Fig. 13-b). One may conclude that the base-plate remained elastic throughout the test. At the end of loading, the extend of the contact area is comprised between 40 and 50 mm. Accordingly, the assumption of EN 1993-1-8 on the position of the centre of compression is quite conservative.

a- SPE1-M90 *b- SPE2-M90*

Fig. 14. *Evolution of the lateral displacement under out-of-plane bending moment*

For specimen SPE1-M90, the deformation of the base-plate was also very significant (see Fig. 14-a and Fig. 15). The drawn deformed shapes indicate that a yield line has developed around the tensioned anchor bolts row and at the level of the column flange in compression. Since the bottom anchor bolt row was above the contact area, the contribution of these anchor bolts to the load carrying capacity is confirmed. The base-plate remains in contact with the concrete surface behind the upper anchor bolts. This confirms the development of prying effect. The contact is lost when the maximal force is reached due to the excessive anchor bolt elongation. The negative displacement obtained in this tensile part is due to closing of the initial gap caused by the welding process.

From the drawn deformed shapes, it can be concluded that at the end of the test contact between the base-plate and the concrete block in the compressive zone was effective over an area of 60 mm from the bottom of the base-plate. However, at early stages of loading, this contact length was 90 mm comprising a portion of the column width. The deformed shape of the top of the base-plate was concave. After failure, the base-plate kept the same deformed shape confirming yielding of the element.

Fig. 15. *Evolution of the top displacement of SPE1-M90*

Similarly to SPE2-M0 specimen, the base-plate of specimen SPE2-M90 exhibits a rigid behavior and anchor bolts were the only source of deformation. A maximum uplift displacement of 10 mm was recorded at the upper free edge of the base-plate. The displacements of the base-plate in the lower part were essentially due to initial gap closure. This results in full contact of the bottom edge of the base-plate with the concrete surface.

2.7. Conclusion on experimental tests

The tests performed on six exposed column base-plates with different base-plate thicknesses and bending moment axis orientations allowed to gain further insight into the behavior of this type of connection. The main conclusions are:

- the bending moment resistances and the initial rotational stiffness of the connection increase with increasing value of the base-plate thickness whatever the orientation of the bending moment axis;
- the bending moment resistances and the initial rotational stiffness of the connection increase as the distance between the centres of compression and tension z increases (longer for major-axis bending moment and shorter for minor-axis bending moment),
- the rotation capacity of the connection increases for decreasing values of the base-plate thickness and decreasing values of the lever arm,
- the base-plate thickness and the orientation of the bending moment axis have limited influence on the behavior of the connection after the maximum force was reached as necking of the anchor bolts develops in these cases. The final failure mode is also not affected by these parameters,
- the orientation of the bending moment axis has an effect on the development of prying forces. Hence for SPE1-M90, prying effect was observed during the tests (and disappeared at failure) whereas prying effect was absent during the whole SPE1-M0 test. This difference is due to the effect of the global rotation of the connection that limits the development of prying effect for an outer anchor row and thus in the case of an strong-axis bending moment,
- the spread of the compressive area is strongly dependent on the base-plate thickness and on the orientation of the applied bending moment.

3. *FINITE ELEMENT ANALYSIS*

3.1. Introduction

The behaviour of column base-plates is known for being highly complex involving multiple phenomena such as geometrical, material and contact non-linearities resulting from the interaction of the different joint components. Due to several technical limitations inherent to the experimental tests, FE models were developed to provide further insight into the behaviour of the connection components by analysing the different stress states to which the connection is subjected when statically loaded. Transfer of internal forces, contact interactions between connection components, performance of the anchoring system, damage of the concrete foundation and yielding/failure of steel elements are examples of situations that can be easily and quite accurately predicted by numerical models. Moreover some phenomena such as contact pressure, cannot be measured during experimental tests but the numerical model provides these informations which are crucial for the development of an accurate analytical model.

3.2. Finite element model

All components (base-plate, column, weld, concrete, anchor bolts …) except the reinforcing bars are modelled as three-dimensional deformable solids using eight-node linear brick elements (see Fig. 16-a and b). Two-node linear truss elements are used for the concrete reinforcing bars (see Fig. 16-c).

a- Connection, concrete block and column b- Anchor bolts c- Concrete block reinforcement

Fig. 16. *Type of elements*

The measured dimensions of the tested specimens have been considered in the finite element model. The anchoring system consists in four M16 anchor bolts which are modelled with nuts and washers, and assuming a constant cross section throughout their length equal to the threaded area A_s.

The material non-linearity was considered and the experimental stress-strain relationship obtained from steel coupon tests was adopted. The elasto-plastic behavior of steel components is described by the von-Mises yield criterion with strain hardening. As suggested by Couchaux et al [19], the stress-

strain relationship introduced in the numerical models is multi-linear (see Fig. 17) and built using the following stress-strain pairs: (f_y;ε_y), (f_y;ε_h), (f_m;ε_m) and (f_u;ε_u) taken from the tensile coupon tests. The behavior is elastic up to the yield strength f_y. Next, the behavior is elastic-plastic up to ε_u. Material failure is simply characterized by an abrupt decrease of the stress to 10 N/mm^2. This approach is appropriate to model the rupture of bolts in tension [19]. The material properties are summarized in Table 6.

.

Fig. 17. *Stress-strain curve for steel*

Table 6 : *Material properties introduced in the FE models*

Elements	f_y	ε_h	f_m	ε_m	f_u	ε_u
	N/mm^2	%	N/mm^2	%	N/mm^2	%
Base-plate 10 mm	423,6	2,6	599,8	15,7	1146,1	121,9
Base-plate 20 mm	401,3	1,7	581,6	14,5	1196,9	125,4
Column web	378,4	2,7	525,3	13,9	1048,0	92,6
Column flange	350,1	2,6	504,4	15,2	1240,0	116,3
Anchor bolt M16	520,4	0,1	626,8	1,4	1367,9	127,5

To validate the material parameters, standard tensile tests (see Fig. 18) were simulated with the FE program and the numerical results were compared against the corresponding experimental data. Cross-sections of the samples are modelled with a total of 20 elements for the round coupons and 24 elements for the rectangular samples. A good agreement was found between the numerical and experimental results for tensile tests (see Fig. 18).

a- Anchor bolts *b- Base-plates*

Fig. 18. *Modelling of coupon tests of anchor bolts and base-plates*

The compressive equivalent stress-strain curve proposed in EC2-1-1 was used to simulate the compressive behaviour of concrete. In this model, linear elastic behaviour is assumed for stress levels below 40% of the maximum compressive strength f_{cm}. Beyond that value, the behavior becomes nonlinear and is governed by the following relationship:

$$\frac{\sigma_c}{f_{cm}} = \frac{k\eta - \eta^2}{1 + (k-2)\eta} \tag{3}$$

with

$f_{cm} = f_{ck} + 8$

f_{ck} : the characteristic compressive cylinder strength of concrete,

$\eta = \varepsilon_c / \varepsilon_{c1}$

$k = 1{,}05 E_{cm} \varepsilon_{c1} / f_{cm}$

Concrete Damaged Plasticity model available in Abaqus material library is used to simulate concrete behavior in compression and tension. Concrete material parameters required by the model include elastic modulus E_{cm}, Poisson's ratio ν_c, flow potential eccentricity, viscosity parameter, dilation angle ψ, shape factor for yield surface K_c and the ratio between initial equi-biaxial compressive yield stress and initial uniaxial compressive yield stress f_{b0}/f_{c0}. The young modulus is evaluated according to EN1992-1-1 [20] and the adopted Poisson's ratio is equal to 0,2. The expression for the strain ε_{c1} associated with f_{cm} is given by Eurocode. The parameter ε_{cu1} is also a function of f_{cm}. Its expression is also given by Eurocode 2. The recommended value for the flow potential eccentricity is 0,1. The dilation angle, ψ, is equal to 36°. As suggested by Szczecina and Winnicki [21], the viscosity parameter is assumed to be equal to zero. The ratio f_{b0}/f_{c0} is equal to 1,16. Finally, the value of the factor K_c which governs the shape of the yield function in the deviatoric plane is determined to be 0.667. The value of the CDP model parameters are reported in Table 7. Concrete behaviour in tension and in compression is depicted in Fig. 19. Nominal values suggested in EN 1992-1-1 are used to define the stress-displacement relationship in tension. This relationship involves the fracture energy.

Table 7 : *Concrete properties introduced in the FE model*

Concrete	f_{cm} (MPa)	ε_{c1} (‰)	f_{ctm} (MPa)	δ_{t1} (mm)
C25/30	see Table 3	2,1	2,6	0
Dilation angle (°)	Eccentricity	f_{b0}/f_{c0}	K_c	Viscosity parameter
36	0,1	1,16	0,667	0

Fig. 19. *Stress-strain curves for concrete*

The loading was applied in two subsequent steps. The first step was defined to initiate contact interactions between the connection components. In the second step, the experimental loading conditions were reproduced. A displacement perpendicular to the centre line of the column steel profile was incrementally applied at the location of the load-jack. As a consequence, the base-plate was subjected to an increasing bending moment with an arbitrary orientation until failure was reached. Boundary conditions were applied to the concrete foundation and the column base-plate connection to reproduce the same support conditions as in the experimental tests described in Section 2. Displacements in the vertical direction were blocked at the neoprene supports in the portal frame A and at the rollers attached to portal frame B. To simulate the support conditions provided by the lateral steel plates placed in both portal frames, displacements in the horizontal direction are restrained. The failure was considered to be attained once the von-Mises strain reached the ultimate strain of the material ε_u in one component, the anchor bolts in the present study. Several contact interactions between elements are created in the models. Kinematic constraints and contact interaction models adopted are listed below:

- "rigid body" constraint: this type of constraint is used to create a rigid cross-section at the top of the column where the load is applied. The reference point is located at the geometric centre of the column cross-section for all models. This constraint allows to guarantee the uniformity of imposed displacement throughout the section. According to Fig. 20, this constraint corresponds to constraint 1,
- "tie" constraint: this type of constraint is used to tie two surfaces in contact during the simulation. Constraints involving two surfaces connected by a weld as 2, 3 and 6 in Fig. 20 are created using "tie" constraint,
- steel-steel interaction: to model the contact between two steel surfaces (4, 5 and 7 in Fig. 20), a surface-to-surface discretization method with finite sliding formulation is adopted considering a friction coefficient equal to 0,3. For normal behavior, the hard contact is selected allowing separation and preventing penetration of surfaces in contact,
- steel-concrete interaction (8 in Fig. 20): same as above with a friction coefficient equal to 0,5,

- steel-concrete with bonding interaction: to model the contact between the lateral surface of the anchor bolts and the concrete block (9 in Fig. 20), a surface-to-surface contact type is selected with finite sliding formulation. For normal behavior, the hard contact option is selected,
- "embedded region" constraint: aims to create the contact interaction between the concrete and the steel reinforcement. An "Embedded region" type constraint is adopted, with the steel reinforcement as embedded elements and the concrete foundation as the host element (constraint 11 in Fig. 20).

Fig. 20. *Interactions considered for the column base-plate models*

Bond properties of the embedded anchor bolts were defined by a local bond-slip relationship. This bond-slip law, for monotonic loading conditions, is taken from FIP Model Code 2010 [22] and is expressed by the following equations. Shear stress τ, developed at the interface between the anchor bolt and the concrete, depends on the relative displacement (slip) s between these two elements.

Fig. 21. *Bond stress-slip law from FIP Model Code 2010*

The bond stress-slip expression is:

$$\tau = \tau_{max} s / s_1 \quad (4)$$

where :

$s_1 = 0{,}1$ mm

$\tau_{max} = 0{,}36\sqrt{f_{ck}}$

With the objective of reducing the computing time needed for the simulation, different mesh sizes were adopted according to the importance of the elements. To simulate the complex stress distributions taking place in anchor bolts during the load history up to failure, a refined mesh was adopted considering the same number of elements for the cross-section as those used in the tensile tests simulations.

To produce reasonable and physically sound stress distributions at the interface between the anchor bolts and the concrete, a smaller mesh size was selected for the layer of concrete material in contact

with the anchor bolts. For the remaining part of the concrete block, a coarser mesh was considered as this zone is of little interest. In regions with high stress concentrations, such as welds, mesh size needed to be reduced. For this reason, four elements were used throughout the thickness. In regions were buckling and/or severe bending were expected such as column flanges and base-plates, it was decided to assign three elements across the wall thickness of these thin elements and four for the 20 mm thickness base-plates. A sensitivity analysis confirmed that this meshing was adequate [24].

3.3. Comparison to tests results

3.3.1. Moment rotation curves and failure modes

The plastic bending moment and the initial rotational stiffness given by the numerical model are compared against their experimental counterparts in Table 8. The plastic bending moment and the initial rotational stiffness obtained with the numerical simulations for all specimens are found to be in good agreement with the experimental data. The values of the plastic bending moment predicted by the numerical models are very satisfactory, with an error less than 7%. The numerical value of the initial rotational stiffness for specimen SPE2-M45 is less satisfactory although acceptable. This discrepancy between the experimental and numerical results is likely due to the simplified and rather conservative model adopted for the adherence (τ_{max}) between the concrete and the anchor bolts. It has a strong effect on the initial rotational stiffness $S_{j,ini}$. In addition, the initial gaps of the base-plates have not been considered in the FE models. This approximation of the base-plate initial geometry may have an impact on the connection deformation mode in the elastic regime and consequently, on the initial rotational stiffness and plastic bending moment values.

Table 8 : *Comparison of the plastic bending resistances and initial rotational stiffness*

Test	Experimental		Numerical		Exp/Num	
	$S_{j,ini,exp}$	$M_{j,pl,exp}$	$S_{j,ini,num}$	$M_{j,pl,num}$	$S_{j,ini}$	$M_{j,pl}$
-	kNm/rad	kNm	kNm/rad	kNm	-	-
SPE1-M0	4117	37,7	4163	35,1	0,99	1,07
SPE2-M0	7190	42,9	7536	46,2	0,95	0,93
SPE1-M90	2029	28,2	2061	26,4	0,98	1,07
SPE2-M90	3120	35,9	2712	37,9	1,15	0,95
SPE1-M45	2440	32,0	2853	32,5	0,86	0,98
SPE2-M45	3205	36,6	4571	38,2	0,70	0,96

A comparison between the yielded elements and the failure modes predicted numerically and those observed experimentally is given in Table 9. For all specimens, the FE model was fairly successful in predicting the yielded components which coincide quite well with those observed experimentally. For specimens SPE1-M0, SPE1-M90 and SPE1-M45, numerical simulations allow to conclude that the column steel profile had a slight incursion in the plastic regime. In contrast to specimen SPE1-M90, this incursion in the plastic regime could not be observed in specimens SPE1-M0 and SPE1-M45 during experimental tests due to missing strain gauges. Local yielding of the welds was also observed as a result of the high deformability of the thinner base-plate and consequently high deformation of the assembly under bending. In all cases, anchor bolts yield as a consequence of tension and local bending moment. For the six models, it was observed that yield lines develop on the base-plate and at the bottom of the column flanges. von-Mises plastic strain distributions in the base-plates are depicted in Fig. 22. Yield lines parallel to the column flanges develop at the base-plate of specimen SPE1-M0 in both compressive and tensile sides. In the tensile side, plastic deformation takes place behind the welds. The latter is also significantly deformed. In contrast to specimen SPE1-M0, the base-plate in specimen SPE2-M0 behaves as a rigid body in the tensile side. In the compressive side, a yield line develops between the anchor bolt row and the column flange. Due to high deformability of the base-plate in specimen SPE1-M90, the development of yield lines occur in both tensile and compressive sides. This is in contrast with specimen SPE2-M90 in which the base-plate remained elastic in the tensile side. For specimen SPE1-M45, a yield line parallel to the column flange develops similarly to that observed in specimen SPE1-M0.

Table 9 : *Comparison of the yielded elements and failure modes*

Test	Experimental		Numerical	
	Yielded elements*	Failure mode	Yielded elements*	Failuremode
SPE1-M0	AB/BP/W	AB	AB/BP/C/W	AB
SPE2-M0	AB	AB	AB/BP	AB
SPE1-M90	AB/BP/C/W	AB	AB/BP/C/W	AB
SPE2-M90	AB/C	AB	AB/BP/C	AB
SPE1-M45	AB/BP/W	AB	AB/BP/C/W	AB/W
SPE2-M45	AB	AB	AB/W	AB

*AB: anchor bolts yielding due to tension and bending; BP: base-plate yielding due to local bending; C: column yielding due to bending; W: weld yielding due to local bending.

The yield line pattern observed in specimen SPE1-M45 suggests a local yielding of the base-plate. Similarly to specimen SPE2-M0 and as a result of the base-plate thickness in specimen SPE2-M45, the yield line occurs only in the compressive side.

a- SPE1-M0 *b- SPE2-M0*

c- SPE1-M90 *d- SPE2-M90*

e- SPE1-M45 *f- SPE2-M45*

Fig. 22. *Yield line patterns obtained from the numerical simulations*

Table 10 : *Comparison of the maximum bending resistances and rotation capacities*

Test	Experimental		Numerical		Exp/Num	
	$M_{j,u,exp}$	$\theta_{j,max,exp}$	$M_{j,u,num}$	$\theta_{j,max,num}$	$M_{j,u}$	$\theta_{j,max}$
-	kNm	mrad	kNm	mrad	-	-
SPE1-M0	43,2	44,7	41,5	45,1	1,04	0,99
SPE2-M0	48,5	33,2	50,8	35,3	0,95	0,94
SPE1-M90	33,3	69,5	32,4	63,4	1,03	1,10
SPE2-M90	40,2	48,1	41,1	45,7	0,98	1,05
SPE1-M45	39,4	62,7	39,0	60,1	1,01	1,04
SPE2-M45	47,3	54,8	45,7	52,2	1,04	1,05

Depending on the orientation of the applied bending moment axis, it is concluded that for all specimens failure predicted numerically and observed experimentally is due to rupture of one or two anchor bolts in tension. The agreement between the numerical and experimental results regarding the maximum bending resistance and the ultimate rotation capacity is also satisfactory (see Table 10). The ratio between experimental and numerical values points out a less satisfactorily estimation of the ultimate rotation capacity with an error of about 10%. In general, the numerical models underestimate the ultimate rotation capacity with an error which can be considered as acceptable. This is a consequence of several factors that compromise the accuracy of this parameter estimation: variability of the material properties; difficulty in defining the exact failure point in simple models and, the accuracy of the computation of the connection rotation during tests. Moment-rotation curves obtained from finite element analyses and the experimental curves are compared in Fig. 23.

a- SPE1-M0 *b- SPE2-M0*

c- SPE1-M90 *d- SPE2-M90*

e- SPE1-M45 *f- SPE2-M45*

Fig. 23. *Moment-rotation curves : comparison between experimental tests and numerical simula-*

tions

As can be seen, the shape of the numerical and experimental curves are quite the same from the starting of the loading (elastic domain) until the end of the test (failure). The moment-rotation characteristics (resistance, initial rotational stiffness and rotation capacity) retrieved from the experiments and those obtained from finite element analyses are in good agreement.

Fig. 24. *Connections at failure : comparison between experimental tests and numerical simulations*

The FE models are therefore able to capture the overall behavior of the tested column base-plates. Furthermore, the deformed shapes produced by the FE models are in good agreement with the those observed experimentally (see Fig. 24). To widen the scope of the present study, the response of specimens SPE1 and SPE2 under biaxial bending moment with different axis orientation is considered. Two additional cases are considered: an applied bending moment with an axis inclination of 30º with respect to the strong axis direction and an inclination of 60º with respect to the same axis. Although these results cannot be compared against experimental data, the ability of the numerical models to simulate the actual response of the connections has been proven. Interaction curves M_0-M_{90} obtained from experimental data and numerical results are drawn and compared in Fig. 25. Results suggest that for these specimens, the evolution of the bending resistance can be accurately predicted by an elliptical curve.

Fig. 25. *Interaction curve M_0-M_{90}*

3.3.2. Anchor bolt forces

The evolution of the tensile force in the anchor bolts with versus the applied bending moment predicted by the FE model is depicted in Fig. 26. These curves allow to evaluate the redistribution of tensile forces in the anchor bolts up to the maximal bending moment. Due to the symmetry of the loading for specimens SPE1-M0, SPE2-M0, SPE1-M90 and SPE2-M90, the evolution of the tensile forces is represented only for the most tensioned anchor bolts. As explained in section 2, a redistribution of inter-

nal forces from the upper to the lower anchor bolt rows is observed for specimen SPE1-M90 and specimen SPE2-M90. Thus, for these cases the evolution of the tensile force in the anchor bolts comprises the lower anchor bolt row.

a- SPE1/2-M0 *b- SPE1/2-M90*

c- SPE1-M45 *d- SPE2-M45*

Fig. 26. *Tensile force in the anchor bolts versus applied bending moment*

For specimens SPE1-M45 and SPE2-M45, anchor bolts AB1, AB2 and AB3 contribute to resist to the applied loads. The evolution of the tensile forces is compared in these three components. Regarding specimens SPE1-M0 and SPE2-M0, it is confirmed that the evolution of the tensile force in the most tensioned anchor bolt (upper row) is almost linear until the bending moment reaches 30-40 kNm. At the end of the loading of specimen SPE1-M0, a slight decrease of the slope is observed. This is a consequence of the modification of the lever arm due to base-plate yielding (see subsection 3.3.3). As mentioned earlier, the configuration of the anchoring system limits the redistribution of internal forces from the upper to the lower anchor bolts rows, the latter remaining inactive (compression side). It can also be concluded that the great flexibility of the base-plate in specimen SPE1-M0 leads to a smaller lever arm z. Consequently, for a given bending moment, the anchor bolts are more loaded than in specimen SPE2-M0. For specimen SPE2-M90, the tensile force in the upper anchor bolt increases linearly until a bending moment of 30-35 kNm. For specimen SPE1-M90 a slight decrease of the slope of the curve is visible at about 25 kNm. In addition, the slope of the lower anchor bolts start to increase at the same load level. This indicates the beginning of the plastic redistribution of tensile forces between upper and lower anchor bolt rows. For specimen SPE2-M90, yielding of the upper row in tension and consequently redistribution occurs for an applied bending moment greater than 30 kNm. At the same time, the lever arm z is altered (see section 3.3.3). This phenomenon is intensified when the upper anchor bolts enter in the necking phase. At the maximum bending moment, the force resisted by the lower anchor bolts corresponds to a quarter of the force sustained by the upper anchor bolts for connection SPE1-M90. For SPE2-M90, the lower anchor bolts are less loaded due to the reduced ductility of SPE2-M90 comparatively to SPE1-M90. The evolution of the tensile force in anchor bolts AB1, AB2 and AB3 for specimens SPE1-M45 and SPE2-M45 is depicted in Fig. 26 c) and

d). As a result of AB4 being located in the compressive zone, the latter remain inactive during the simulation for both cases. It can be observed that AB2 is the most tensioned anchor bolt. For specimen SPE1-M45, the slope of the curve of AB2 starts to decrease for a bending moment close to 30 kNm. At the same load level, the force in anchor bolts AB1 and AB3 starts to increase and plastic redistribution is activated. Anchor bolt AB3 is located immediately under AB2 and contribute to the load carrying mechanism nearly from the beginning of the loading. The tensile forces resisted by anchor bolts AB2 and AB3 have the same magnitude at the end of the simulation. AB1 being located near the compressive zone, its contribution to the load carrying mechanism is the lowest. At the end of the loading, AB1 withstand approximately 3/4 of the maximum tensile force in AB2.

3.3.3. Contact area

In contrast to the assumption of EN 1993-1-8, the position of the centre of compression is not fixed at the column flange in compression (for in-plane bending moment). In reality, as mentioned earlier, contact zones vary with the loading due to the continuously changes of the relative flexibility of the different components. The evolution of the centre of compression location z_c is depicted in Fig. 27 along with the constant value given by EN 1993-1-8.

a- SPE1/2-M0 *b- SPE1/2-M90*

c- SPE1/2-M45 *d- Position of the centre of compression*

Fig. 27. *Evolution of the position of the centre of compression obtained from the numerical models*

The comparison between the positions of the centre of compression obtained numerically with those given by the Component method in EN 1993-1-8 for specimens SPE1-M0 and SPE2-M0 suggests that the approach adopted in the Eurocode is quite conservative for thick flanges. From the numerical simulations, it can be concluded that z_c is not constant. In fact, z_c remains nearly constant during early stage of loading characterized by a value of the bending moment below 10-15 kNm. However, z_c increases with increasing values of the applied bending moment. This evolution is a consequence of the modification of the relative stiffness between the tensile and the compressive areas caused by the yielding of base-plates.

Regardless of the loading case (M0, M90 or M45), the centre of compression for thicker base-plates (20 mm) tends to move away from the footprint of the column flange towards the base-plate free

edge. This trend is apparently less pronounced for the cases with a thinner base-plate (10 mm), for which z_c does not vary substantially and remains nearly constant, close to the column flange.

For SPE1-M0, the centre of compression at the end of the analysis is located above the lower anchor bolt row. For specimen SPE2-M0, it can be seen that z_c moved towards the base-plate edge, and near collapse, z_c is located between the lower anchor bolt row and the base-plate free edge. For specimen SPE1-M90, the evolution of z_c is insignificant. Consequently, the centre of compression remains at the level of the column flange corners, with all the anchor bolts located in the tensile side. For the specimen SPE2-M90 the evolution is more pronounced than in the previous case and, at the end of the loading z_c is located close to the base-plate edge.

a- SPE1-M0 (elastic regime) *b- SPE1-M0 (failure)*

c- SPE2-M0 (elastic regime) *d- SPE2-M0 (failure)*

Fig. 28. *Contact pressures on the base-plates for SPE1/2-M0 (in N/mm^2)*

a- SPE1-M90 (elastic regime) *b- SPE1-M90 (failure)*

c- SPE2-M90 (elastic regime) *d- SPE2-M90 (failure)*

Fig. 29. *Contact pressures on the base-plates for SPE1/2-M90 (in N/mm^2)*

Contour plot of the contact pressure acting on the base-plate bottom surface (in contact with the concrete) in the elastic regime and at failure are depicted in Fig. 28 to Fig. 30. According to the evidences presented above, contact pressures tend to move towards the lower edge for thicker base-plates, with a more or less uniform distribution over the base-plate width. Conversely, for more deformable base-plates (10 mm), contact pressures are located close to the column flanges. For M0, M90 and M45, the development of prying effects at an initial stage of the loading may be observed for SPE1 test series. For specimen SPE1-M0, contact pressure develops between the lower column flange and the lower anchor bolt row during the elastic regime. Near collapse, contact pressures are located around the lower anchor bolts in the compressive area. Prying effect disappears as a result of the excessive anchor bolt elongation. During experimental tests prying effects did not develop as consequence of initial gaps. For specimen SPE2-M0, contact pressure develops between the lower anchor bolt row and

the free edge of the base-plate during the elastic regime. Near collapse, pressures are located at the lower free edge of the base-plate.

For specimen SPE1-M90, contact pressure develops locally around the column flanges in the compressive area during the elastic regime and near failure. At the beginning of the loading, prying forces develop in the tensile area and disappear near collapse. A similar trend was observed during tests. For specimen SPE2-M90, contact pressures are located around the column flange and the free edge of the base-plate at the beginning of the loading. At collapse, contact stresses move closer to the free edge. For specimens SPE1-M45 and SPE2-M45, contact pressure distribution does not significantly change between the elastic and plastic regimes and are located close to the column flange corner.

a- SPE1-M45 (elastic regime) *b- SPE1-M45 (failure)*

c- SPE2-M45 (elastic regime) *d- SPE2-M45 (failure)*

Fig. 30. *Contact pressures on the base-plates for SPE1/2-M45 (in N/mm^2)*

3.4. Conclusions on the simulations

The results of the experimental tests on column base-plates presented in section 2 are enriched with results of the detailed finite elements models. The following conclusions can be drawn:

- the resistance, initial rotational stiffness and rotation capacity predicted by the FE models are very close to those derived from the experimental tests on the six specimens. The yielded elements and obtained failure modes are well reproduced. Additionally, the numerical model confirms yielding of the column and the welds in specimens SPE1-M0, SPE1-M90 and SPE1-M45,
- the numerical models allow the evaluation of the contribution of the anchor bolts to the load carrying mechanism. For M90 and M45 series, a redistribution between the anchor tension forces is observed between the most tensioned anchor bolts and the remaining active anchor bolts,
- the position of the centre of compression z_c varies with the applied bending moment which contrast with the assumption made in the Component Method, the latter approach being quite conservative,

- for all test series (M0, M90 and M45), the lever arm of the centre of compression is higher for thicker base-plates. Consequently, z_c strongly depends on the flexibility of the base-plate.
- For the two investigated geometries, the numerical model confirmed that the interaction curve can be described by an ellipse as suggested by Amaral [16] and Fasae et al [17].

4. ANALYTICAL MODEL

The behaviour of column base-plate connections under biaxial bending moment was thoroughly investigated via testing FE analyses. The numerical study demonstrated that the extend of the contact area is influenced by the thickness of the base-plate. This aspect will be integrated in the analytical model for the evaluation of the connection resistance when subjected to in-plane or out-of-plane bending moment. In the proposed analytical model, we account for the plastic redistribution between anchor bolt tension forces observed in the Finite Element analyses of connections subjected to bi-axial bending moment.

4.1. General assumptions

The connections explored in this work consist in a rigid/semi-rigid extended base-plates welded to a I or H steel column. The extended base-plate is fastened to the concrete foundation by means of four outer anchor bolts. The design of the connection ensure that failure does not occur in the welds or the concrete block and that rupture of the connection is triggered by yielding of the base-plate and/or failure of the anchor bolts. Good contact conditions are assumed at the interface between the concrete block and the embedded length of the anchor bolts. The axial force is neglected.

The components considered in the analytical model are the following:

- The components ensuring transfer of tensile force due to the bending are the base-plate in bending and the anchor bolts in tension;
- The components ensuring transfer of the compressive force due to bending are the concrete in compression, the base-plate in bending under bearing pressure exerted by the foundation and the column in compression.

The ultimate resistance of the abovementioned components in tension $F_{T,u}$ is calculated according to EC3-1-8 and corresponds to the lowest resistance between Modes 1, 2 and 3 (with prying effect) or Modes 1-2 and 3 (without prying effect). For Mode 1, the ultimate tensile strength f_u is used instead of the yield strength f_y. Additionally, for Mode 2, the base-plate yield strength f_y is replaced with $(2f_y+f_u)/3$ [23] to include strain hardening of this component before anchor bolt failure in tension. The

ultimate resistance of the components in compression $F_{C,u}$ is calculated based on rules given in EN1992. In the Component Method, the effective bearing area is calculated based on an additional effective width derived from the expression of the elastic bending resistance of the base-plate. The proposed model suggest a modified effective width c that takes into account the plastic limit of the bending moment resistance of the base-plate as well as the width of the fillet welds which contribute to transfer the compressive forces to the concrete block:

$$c = t_p \sqrt{\frac{f_{y,p}}{2 f_{jd,max}}} + \sqrt{2} a \tag{5}$$

with

t_p: base-plate thickness,

$f_{y,p}$: base-plate yield strength,

$f_{jd,max}$: concrete compressive strength,

a: weld throat thickness.

4.2. Bending resistance

We derive closed form expressions for the bending resistance considering separately uniaxial bending and biaxial bending moment.

4.2.1. In-plane bending resistance

In-plane bending moment produces contact stresses between the base-plate and the concrete block at the outer edge for thick base-plates and rather close to the column flange for thin base-plates (see Fig. 28). In the present model, the position of the compressive force depends on the thickness of the base-plate. The compressive force is assumed to be uniformly distributed under the flanges in a length denoted $x_{c,in}$ and an effective length l_{eff}. The contact area is bounded by the additional effective width c (see Fig. 31). The total compressive force is:

$$F_{c,u,in} = x_{c,in} l_{eff} f_{jd,max} \tag{6}$$

where l_{eff} is the effective length of the compressive area :

$$l_{eff} = 2c + b_{fc} \leq b_p$$

The axial force being equal to zero, the forces acting in the tensile and the compressive parts are equal in magnitude and thus:

$$x_{c,in} = \frac{F_{T,u}}{l_{eff} f_{jd,max}} \leq t_{fc} + 2c = b_{eff} \tag{7}$$

Basic equilibrium condition provide the expression of the in-plane bending resistance:

$$M_{ip,u,0} = F_{T,u} \left(z_T + z_C \right) \tag{8}$$

With:

$$z_C = h_c / 2 + c - x_{c,in} / 2$$

Fig. 31. *Force distribution in presence of in-plane bending moment*

4.2.2. Out-of-plane bending resistance

Numerical simulations have shown that applying an out-of-plane bending moment to the connection produces contact stresses over an area located behind the corner of the column flange (see Fig. 29). The compressive stress distribution is assumed to be uniformly distributed over a rectangular area below both flanges. The length and the width of this area are denoted $x_{c,op}$ and $b_{eff,}$ respectively (see Fig. 32). With these assumptions, the total compressive force is:

$$F_{c,u,op} = 2 x_{c,op} b_{eff} f_{jd,max} \tag{9}$$

where b_{eff} is the effective width of the compressive zone :

$$b_{eff} = 2c + t_{fc}$$

Since the connection is loaded by a pure bending moment, the compressive and the tensile forces are equal in magnitude:

$$F_{c,u,op} = F_{T,u} \tag{10}$$

Combining (9) and (10), it comes:

$$x_{c,op} = \frac{F_{T,u}}{2 b_{eff} f_{jd,max}} \tag{11}$$

Bending equilibrium gives the expression of the out-of-plane bending resistance:

$$M_{op,u,0} = F_{T,u} \left(z_{T,op} + z_{C,op} \right) \tag{12}$$

with:

$$z_{\mathrm{T,op}} = p_2 / 2,\ z_{\mathrm{C,op}} = l_{\mathrm{eff}} / 2 - x_{\mathrm{c,op}} / 2.$$

Fig. 32. *Force distribution in presence of out-of-plane bending moment*

4.2.3. Biaxial bending resistance

The FE analyses of connections subjected to biaxial bending moment revealed a substantial plastic redistribution of tensile forces between anchor bolts before failure. The mechanical model selected for the evaluation of the resistance under biaxial bending moment assumes a redistribution of the out-of-plane bending moment generating two bending moments on both side of the strong axis $M_{\mathrm{op,l}}$ and $M_{\mathrm{op,r}}$. Subscripts 'l' and 'r' stands for left an right, respectively (see Fig. 33). The in-plane bending moment generates axial forces on these both sides that can be calculated straightforwardly by simple equilibrium equations.

Considering the compressive lever arm of Eq (8) results:

$$F = \frac{M_{\mathrm{ip,u}}}{z_{\mathrm{T}} + z_{\mathrm{C}}} = \frac{M_{\mathrm{ip,u}}}{z_{\mathrm{in}}} \tag{13}$$

These forces are applied on each side of the connection along with the out-of-plane bending moments $M_{\mathrm{op,l}}$ and $M_{\mathrm{op,r}}$. These two bending moments balance the total out-of-plane bending moment applied to the connection:

$$M_{\mathrm{op,u}} = M_{\mathrm{op,r}} + M_{\mathrm{op,l}} \tag{14}$$

Fig. 33. *Force distribution in presence of bi-axial bending moment*

The resistance of both sides of the connection depends on the magnitude of the force F. For the left side, F is a tensile force and two types of behaviour can be expected:

- The out-of-plane bending moment is dominant and both compressive and tensile forces develops,
- The tensile force F is dominant resulting in the two anchor bolts being under tension

For the right side, F is a compressive force and two types of behavior can be expected:

- The out-of-plane bending moment is dominant and compressive and a tensile forces develop,

- The compressive force F is dominant and only compressive forces develop. Anchor bolt do not transmit any tensile force .

Overall, three behaviors will be considered for the evaluation of the resistance in presence of biaxial bending moment:

- The two sides develop compressive and tensile sides, the force F (caused by in-plane bending moment) is less important compared to the out-of-plane bending moment. The out-of-plane governs the connection behavior and will be analyzed in section 4.2.3.1.
- Both anchor bolts of the left side are under tension whereas compressive and tensile forces develop on the right side. This mixed behavior is presented in section 4.2.3.2.
- The left anchor bolts work in tension while the right side works in compression. The in-plane bending moment is dominant and this behavior will be presented in section 4.2.3.3.

4.2.3.1. Dominant out-of-plane bending moment

- **Out-of-plane bending moment of the left side**

In the left side, anchor bolt reach its ultimate resistance as it is the most loaded tensile side (see Fig. 34). A compressive area also develops. The compressive force is:

$$F_{c,op,l} = x_{c,op,l} b_{eff} f_{jd,max} \tag{15}$$

Axial equilibrium gives:

$$F = F_{T,u}/2 - F_{c,op,l} \tag{16}$$

The length of the compressive area is thus:

$$x_{c,op,l} = \frac{F_{T,u}/2 - F}{b_{eff} f_{jd,max}} \tag{17}$$

The out-of-plane bending moment of the right side is thus:

$$M_{op,l} = z_{T,op} F_{T,u}/2 + F_{c,op,l} \cdot \left(l_{eff}/2 - x_{c,op,l}/2 \right) \tag{18}$$

- **Out-of-plane bending moment of the right side**

In the right side, it is also assumed that the anchor bolt reach its ultimate resistance (see Fig. 34). The compressive force is:

$$F_{\mathrm{c,op,r}} = x_{\mathrm{c,op,r}} b_{\mathrm{eff}} f_{\mathrm{jd,max}} \tag{19}$$

Axial equilibrium gives:

$$F = F_{\mathrm{c,op,r}} - F_{\mathrm{T,u}} / 2 \tag{20}$$

The length of the compressive area is thus:

$$x_{\mathrm{c,op,r}} = \frac{F_{\mathrm{T,u}} / 2 + F}{b_{\mathrm{eff}} f_{\mathrm{jd,max}}} \tag{21}$$

The out-of-plane bending moment of the right side is thus:

$$M_{\mathrm{op,r}} = z_{\mathrm{T,op}} F_{\mathrm{T,u}} / 2 + F_{\mathrm{c,op,r}} . \left(l_{\mathrm{eff}} / 2 - x_{\mathrm{c,op,r}} / 2 \right) \tag{22}$$

Fig. 34. *Force distribution in presence of dominant out-of-plane bending moment*

Inserting (18) and (22) in (14), one obtains the total out-of-plane bending resistance:

$$M_{\mathrm{op,u}} = M_{\mathrm{op,u,0}} - \frac{M_{\mathrm{ip,u}}^2}{b_{\mathrm{eff}} f_{\mathrm{jd,max}} z_{\mathrm{in}}^2} \tag{23}$$

4.2.3.2. Mixed behavior

On the left side, both anchor bolts are loaded in tension and failure is reached in the most tensioned anchor bolt, the out-of-plane bending moment of this side is:

$$M_{\mathrm{op,l}} = z_{\mathrm{T,op}} \left(F_{\mathrm{T,u}} - F \right) \tag{24}$$

Fig. 35. *Force distribution for mixed behaviour*

On the right side, only one bolt is loaded in tension. Experimental tests and numerical simulations confirmed that this bolt did not fail. Numerical simulations performed on column bases subjected to axial force and out-of-plane bending moment highlighted [24] that anchor bolt failure was not obtained in presence of a compressive force. This result is considered for the evaluation of the tensile force assuming :

$$F_{\mathrm{T}} = \frac{F_{\mathrm{T,u}}}{2} \left(1 - \frac{x_{\mathrm{c,op,r}} - x_{\mathrm{c,op,I}}}{\Delta x_{\mathrm{c,op}}} \right) \tag{25}$$

with

$$\Delta x_{c,op} = l_{eff}/2 + z_{T,op} - x_{c,op,I}$$

$$x_{c,op,I} = \frac{F_{T,u}}{b_{eff} f_{jd}}$$

In addition, considering the bearing strength equal to the concrete compression strengths leads to an overestimation of the resistance when substantial in-plane bending moment is applied. At the end of the loading, the total compressive force should not exceed $F_{T,u}$, the equivalent bearing strengh is thus:

$$f_{jd,0} = \frac{F_{T,u}}{b_{eff} l_{eff}} \tag{26}$$

During the mixed behavior and in-plane dominant bending moment, the following expression will be assumed for the bearing strength :

$$f_{jd} = f_{jd,max} - \left(f_{jd,max} - f_{jd,0}\right)\frac{F - F_{T,u}/2}{F_{T,u}/2} \tag{27}$$

The compressive force is:

$$F_{c,op,r} = x_{c,op,r} b_{eff} f_{jd} \tag{28}$$

Axial equilibrium gives:

$$F_{c,op,r} - F_T = F \tag{29}$$

The length of the compressive area is thus:

$$x_{c,op,r} = \frac{\alpha F_{T,u}/2 + F}{b_{eff} f_{jd} + \dfrac{F_{T,u}}{2\Delta x_{c,op}}} \tag{30}$$

with

$$\alpha = 1 + \frac{x_{c,op,I}}{\Delta x_{c,op}}$$

The out-of-plane bending moment of the right side is thus:

$$M_{op,r} = F_T z_{T,op} + F_{c,op,r}.\left(l_{eff}/2 - x_{c,op,r}/2\right) \tag{31}$$

Inserting (29) and (30) in (31), one obtain the out-of-plane bending resistance of the right side:

$$M_{\mathrm{op,r}} = z_{\mathrm{T,op}}\left(F_{\mathrm{c,op,r}} - F\right) + F_{\mathrm{c,op,r}}.\left(l_{\mathrm{eff}}/2 - \frac{F_{\mathrm{c,op,r}}}{2b_{\mathrm{eff}} f_{\mathrm{jd}}}\right) \tag{32}$$

Finally, the out-of-plane bending resistance is:

$$M_{\mathrm{op,r}} = z_{\mathrm{T,op}}\left(F_{\mathrm{T,u}} + F_{\mathrm{c,op,r}} - 2F\right) + F_{\mathrm{c,op,r}}.\left(l_{\mathrm{eff}}/2 - \frac{F_{\mathrm{c,op,r}}}{2b_{\mathrm{eff}} f_{\mathrm{jd}}}\right) \tag{33}$$

4.2.3.3. Dominant in-plane bending moment

On the left side, both anchor bolts are loaded in tension and failure is reached in the most tensioned anchor bolt (see Fig. 36), the out-of-plane bending moment of this side is:

$$M_{\mathrm{op,l}} = z_{\mathrm{T,op}}\left(F_{\mathrm{T,u}} - F\right) \tag{34}$$

Fig. 36. *Force distribution under dominant in-plane bending moment*

The right side is purely under compression (see Fig. 36). By axial equilibrium, the length of the compressive area is simply:

$$x_{\mathrm{c,op,r}} = \frac{F}{b_{\mathrm{eff}} f_{\mathrm{jd}}} \tag{35}$$

The out-of-plane bending of the right side is thus:

$$M_{\mathrm{op,r}} = F.\left(l_{\mathrm{eff}}/2 - \frac{F}{2b_{\mathrm{eff}} f_{\mathrm{jd}}}\right) \tag{36}$$

The total bending out-of-plane bending moment is finally :

$$M_{\mathrm{op,r}} = z_{\mathrm{T,op}}\left(F_{\mathrm{T,u}} - \frac{M_{\mathrm{ip,u}}}{z_{\mathrm{in}}}\right) + \frac{M_{\mathrm{ip,u}}}{z_{\mathrm{in}}}.\left(l_{\mathrm{eff}}/2 - \frac{M_{\mathrm{ip,u}}}{2b_{\mathrm{eff}} f_{\mathrm{jd}} z_{\mathrm{in}}}\right) \tag{37}$$

4.2.4. Comparison to experimental tests and numerical simulations

The ultimate bending resistances predicted by this analytical proposal are compared against their experimental counterparts in Table 11. The results obtained with the proposed analytical model are in very good agreement with the test results whatever the orientation of the bending moment or the

thickness of the base-plate. The mean value of the ratio $M_{j,u,ana}/M_{j,u,test}$ is 0,96. Moreover, the analytical model predicts failure of anchor bolts in tension according to failure mode 2 for SPE1 specimens and to failure mode 3 for SPE2 specimens. The M_{op}-M_{ip} diagram obtained by the analytical model is compared to experimental/numerical results in Fig. 37. The results are in good agreement.

Table 11 *Ultimate resistance comparison to experimental tests*

Specimen	$M_{j,u,test}$	$M_{j,u,ana}$	$M_{j,u,ana}/M_{j,u,test}$
	kNm	kNm	-
SPE1-M0	43,2	40,4	0,94
SPE2-M0	48,5	49,2	1,01
SPE1-M90	33,3	31,7	0,95
SPE2-M90	40,2	38,7	0,96
SPE1-M45	39,3	36,4	0,93
SPE2-M45	47,3	46,8	0,99

a- SPE1

b- SPE2

Fig. 37. *Interaction curve M_0-M_{90} : Comparison of analytical and experimental/Numerical results*

5. CONCLUSION

In the present paper, the behavior of exposed column base-plates under biaxial bending moment has been studied experimentally, numerically and analytically. A particular attention was dedicated to the impact of the base-plate thickness on the behavior of the connection. The major findings of this work are listed below:

- the bending moment resistances and the initial rotational stiffness of the connections increase for thick base-plates whatever the orientation of the bending moment. On the other hand, increasing the base-plate thickness leads to a drop in the rotation capacity. Also, the distribution of the internal forces in the base-plates is strongly affected by this parameter. For thinner base-plates and out-of-plane bending moment, a considerable stress concentration occurs at the footprint of the column flange in compression and at the level of the tensioned anchor bolt row. The same was not observed for the specimens with thick base-plates. Finally, it was also found that the base-plate thickness governs the redistribution of the internal forces within the anchoring system as well as the development of prying forces,

- the direction of the applied bending moment also influences the bending resistances and initial rotational stiffness. The lowest mechanical characteristics of the moment-rotation curve are obtained for out-of-plane bending moment and the largest for in-plane bending moment. The distance between the centres of compression and tension is at the origin of this difference. The development of prying effect is also influenced by the orientation of the bending as observed for SPE1 series. Image correlation revealed appearance and disappearance of prying effect, and the potential expansion of the compression area. However, the failure mode was not impacted by the orientation of the bending moment. The latter is rather driven by anchor bolt failure in tension.
- the numerical results were validated and compared against the experimental tests data. From this confrontation, it was concluded that the agreement between the results obtained numerically and from the experimental tests in terms of resistance, initial rotational stiffness, rotation capacity and strain distribution is satisfactory. Besides the fact that the yielded elements and the obtained failure modes were the same, the numerical analyses allowed to validate the assumptions of yielding of the column and the welds in specimens SPE1-M0, SPE1-M90 and SPE1-M45. In addition, the FE analyses allowed to confirm experimental observations such as the spread of the contact area and the redistribution of the tensile force between anchor bolts for out-of-plane and biaxial bending moments. It was possible to precisely estimate the position of the centre of compression that strongly depends on the base-plate thickness and can be far away from the conservative assumptions of Eurocode 3 part 1-8 for in-plane bending moment.
- An analytical model was proposed for the evaluation of the bending resistance whatever the orientation of the bending moment. The resistance of the tensile area is based on the T-stub concept. The position of the centre of compression is evaluated considering axial equilibrium and simple contact pressure distribution. This position strongly depends on the base-plate stiffness. For biaxial bending moment, a redistribution of the out-of-plane bending moment is considered. The results obtained with the analytical model are in good agreement with experimental tests whatever the orientation of the bending moment.

Finally, it is important to mention that in the present study the axial force was not considered although

it has preponderant influence on the connection response. Further investigations and additional FE analyses have been performed to assess the effect of axial load on the connection behavior [24] and will be presented in a future paper.

REFERENCES

[1] Delesques R., Resistance of column base-plates, Revue Construction Métallique, N°3, 1971 (in French).

[2] Lescouarc'h Y., Rigid steel column bases, CTICM, 1988 (in French).

[3] DeWolf J.T., Ricker D.T., Column Base-plates, Steel Design Guide Series, AISC, 1991.

[4] EN 1992-4 (Eurocode 2): Design of concrete structures – Part 4: Design of fastenings for use in concrete, October 2018.

[5] Picard A., Beaulieu D., Behaviour of a simple column base connection, Canadian Journal of Civil Engineering, Vol.12, p.126-136, 1984.

[6] Jaspart J.P., Vandegans D., Application of the component method to column bases. Journal of Constructional Steel Research, Vol.48, p.89-106, 1998.

[7] Drake R. M., Elkin, S. J., Beam-Column Base-plate Design - LRFD Method, Engineering Journal, AISC, Vol.36, No. 1, p.29-38, 1999.

[8] Wald F., Sokol Z., Steenhuis M., Jaspart, J.P., Component method for steel column bases, Heron, Vol.53, p.3-20, 2008.

[9] Stamatopoulos G., Ermopoulos J., Experimental and analytical investigation of steel column bases, Journal of Constructional Steel Research, Vol.67, p.1341-1357, 2011.

[10] EN 1993-1-8 (Eurocode 3): Design of steel structures - Part 1-8: Design of joints. Brussels, December 2005.

[11] Fisher J.M., Kloiber L.A., Base-plate and anchor rod design, Steel Design Guide Series, AISC, 2006.

[12] Ruopp J., Kuhlmann U., Steel-to-concrete joints with large anchor plates under shear loading, Steel Construction, Vol.10, p.115–124, 2017.

[13] Lee D. Y., Goel S., Stojadinovic B., Exposed column-base-plate connections bending about weak axis: I. Numerical parametric study, Steel Structures, Vol.8, p.11–27, 2008a.

[14] Lee D. Y., Goel S., Stojadinovic B., Exposed column-base-plate connections bending about weak axis: II. Experimental study, Steel Structures, Vol.8, p.29–41, 2008b.

[15] Bajer M. , Vild M., Barnat J., Holomek J., Influence of selected parameters on design optimization of anchor joint, 12th International Conference on Steel, Space and Composite Structures, Prague, 28-30 May 2014, p.149-158, 2014.

[16] Amaral P., Steel column bases under biaxial loading conditions (master degree dissertation), Porto: University of Porto, 2014.

[17] Fasaee M. A. K., Banan M. R., Ghazizadeh S., Capacity of exposed column base connections subjected to uniaxial and biaxial bending moments, Journal of Constructional Steel Research, Vol.148, p.361–370, 2018.

[18] ECCS, Recommended testing procedures for assessing the behavior of structural elements under cyclic loads, European Convention for Constructional Steelwork, Technical Committee 1, TWG 13 – Seismic Design, No45, 1986.

[19] Couchaux M., Hjiaj M., Ryan I., Bureau A., Tensile resistances of L-stubs, Journal of Constructional Steel Research, Vol.138, p.131–149, 2017.

[20] European Committee for Standardisation (2004) CEN, Eurocode 2, ENV 1992-1-1:2004, Eurocode 2: Design of concrete structures - Part 1-1: General rules and rules for buildings. Brussels.

[21] Szczecina M., Winnicki A., Calibration of the CDP model parameters in Abaqus, Advances in Structural Engineering and Mechanics, 2015.

[22] International Federation for Structural Concrete (fib) FIP Model Code 2010. Lausanne, 2010.

[23] Packer J., Bruno L., Birkemoe P., Limit analysis of bolted RHS flange plate joints, Journal of Structural Engineering, Vol.115, p.2226-2242, 1989.

[24] Seco L., Column base-plates under 3D loading, Doctoral thesis, INSA Rennes, 2019.

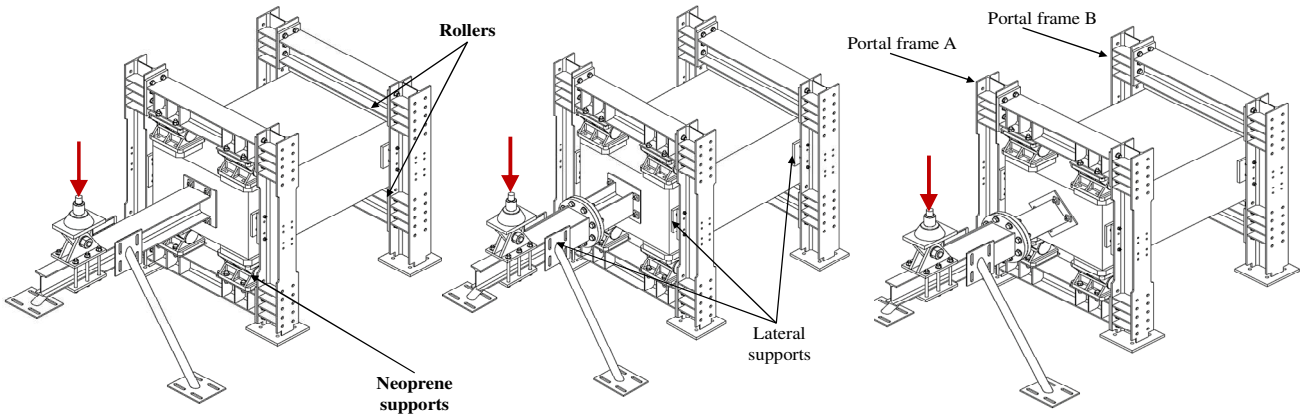
Rollers
Neoprene supports
Lateral supports
Portal frame A
Portal frame B

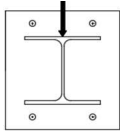
M0°

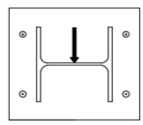
M90°

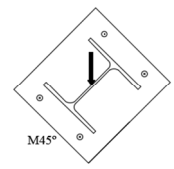
M45°

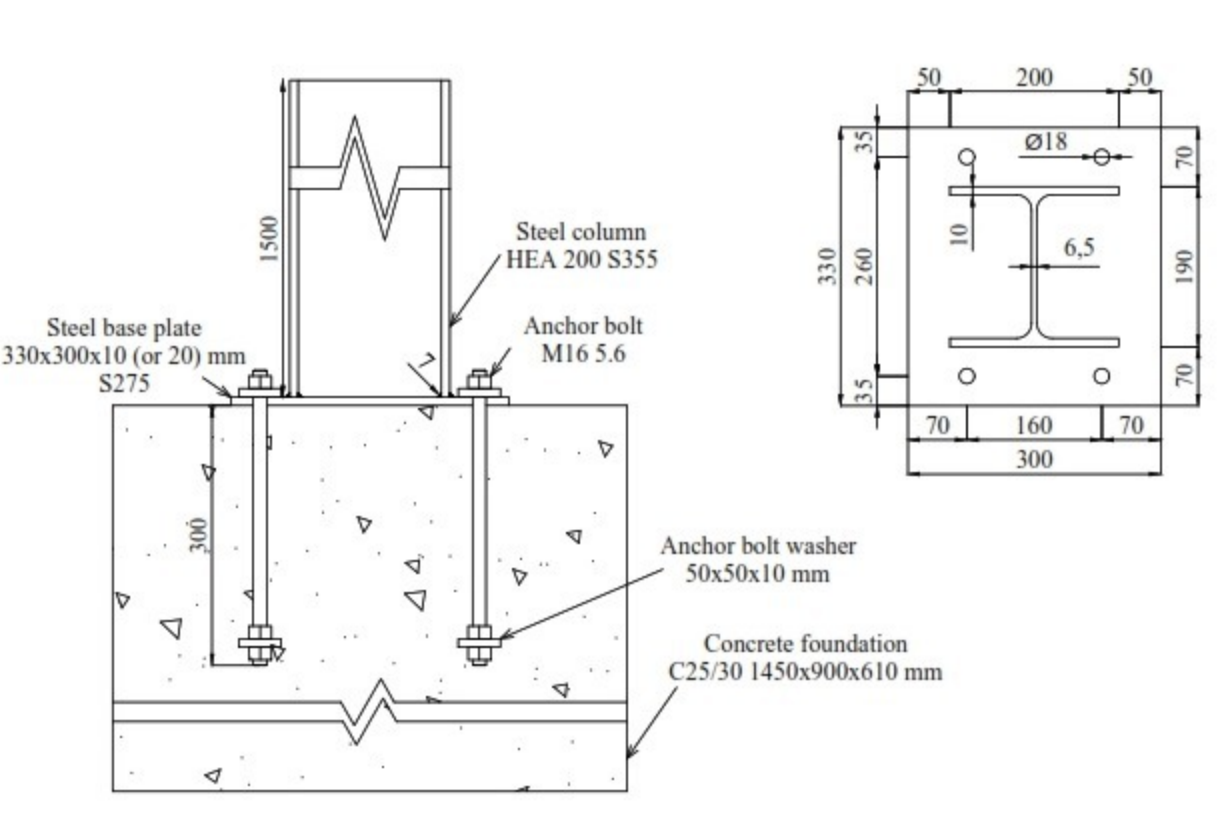
1500
Steel column
HEA 200 S355
Steel base plate
330x300x10 (or 20) mm
S275
Anchor bolt
M16 5.6
300
Anchor bolt washer
50x50x10 mm
Concrete foundation
C25/30 1450x900x610 mm
50
200
50
Ø18
35
70
10
6,5
330
260
190
35
70
70
160
70
300

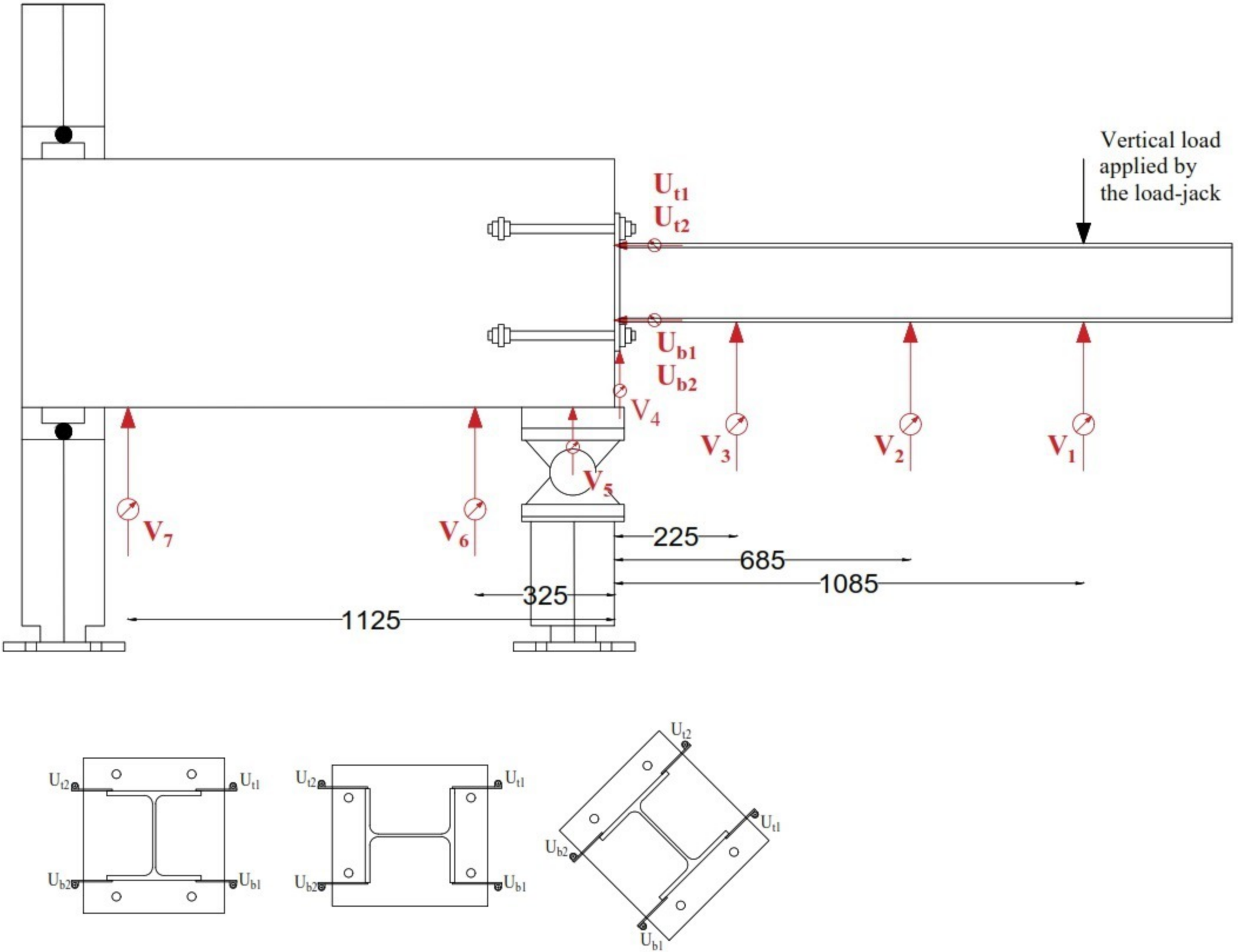
Vertical load
applied by
the load-jack
U_{t1}
U_{t2}
U_{b1}
U_{b2}
V_1
V_2
V_3
V_4
V_5
V_6
V_7
225
685
1085
325
1125
U_{t2}
U_{t1}
U_{b2}
U_{b1}

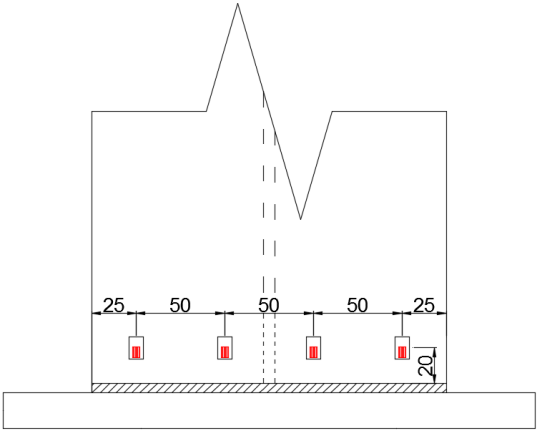
25
50
50
50
25
20

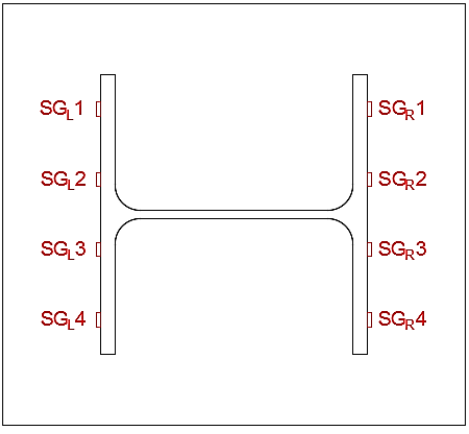
SG_L1
SG_L2
SG_L3
SG_L4
SG_R1
SG_R2
SG_R3
SG_R4

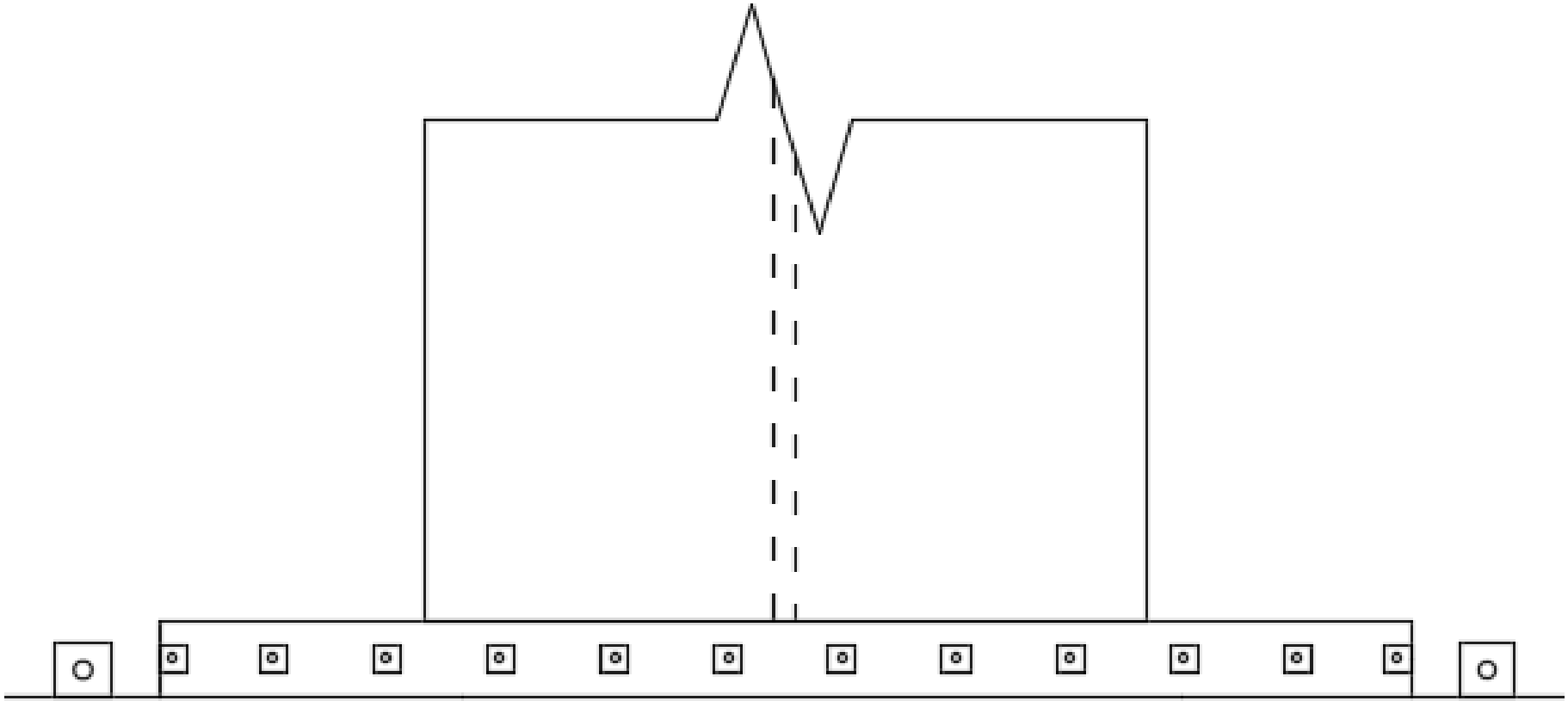

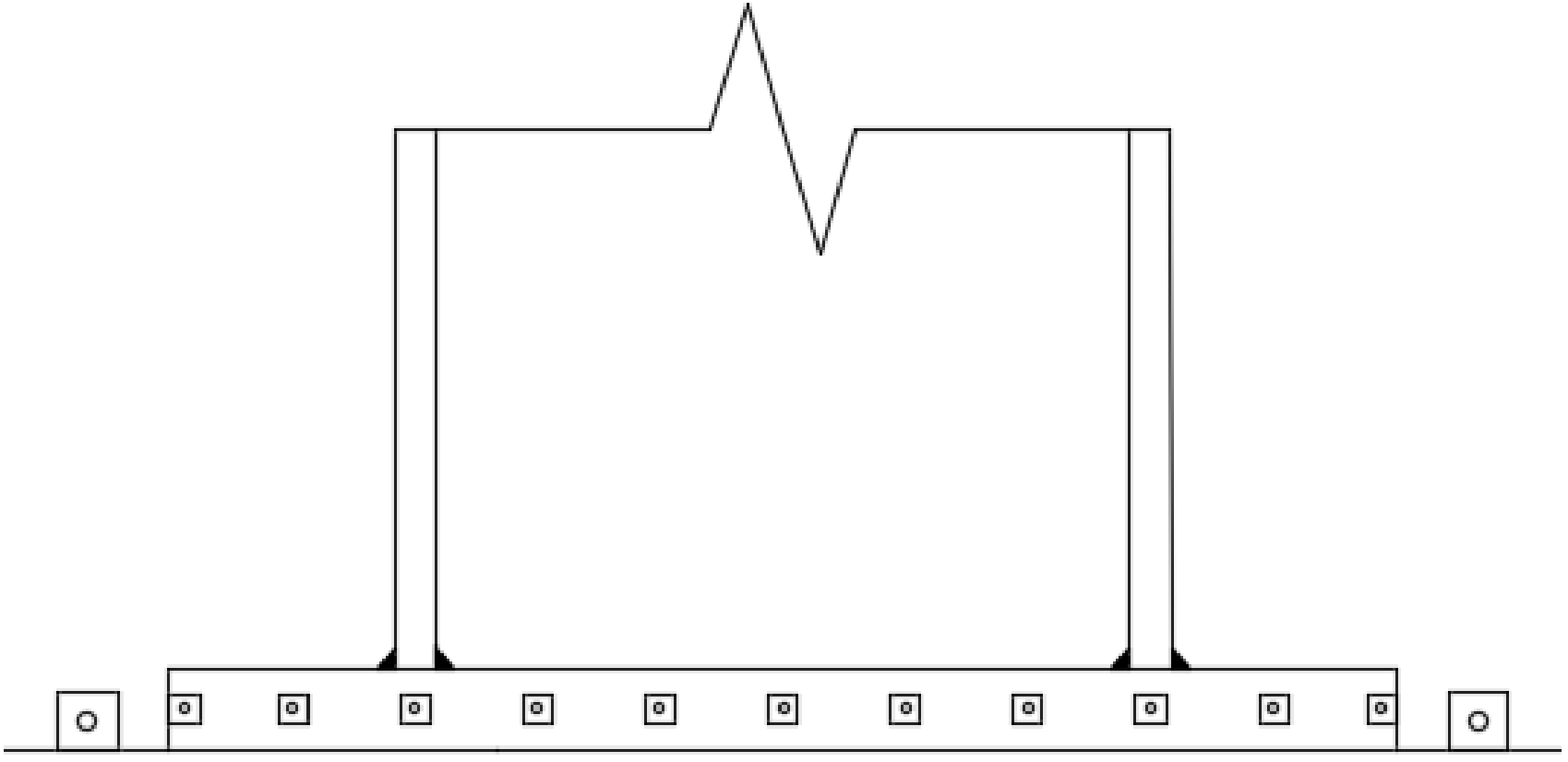

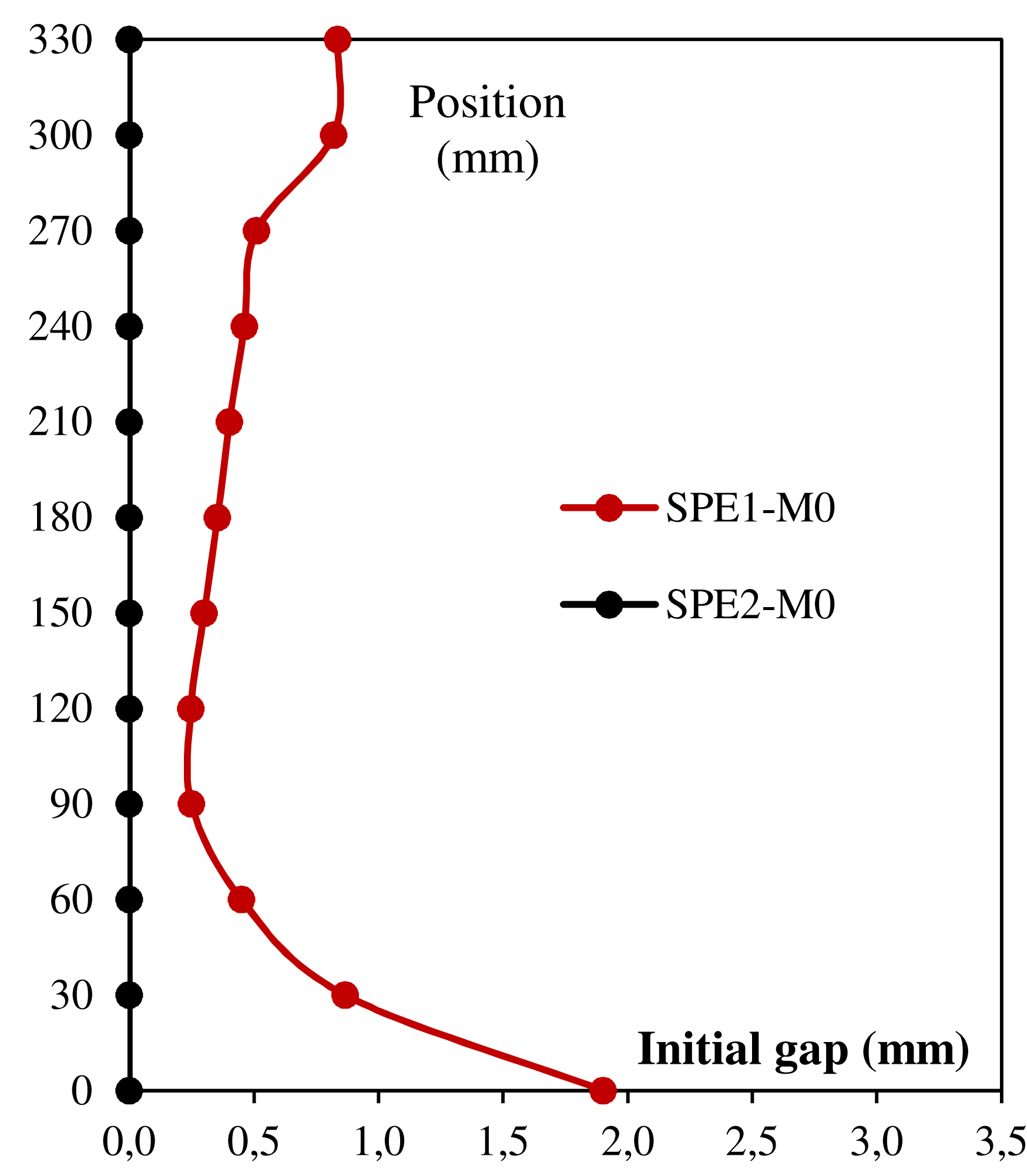
330
300
270
240
210
180
150
120
90
60
30
0
Position
(mm)
SPE1-M0
SPE2-M0
Initial gap (mm)
0,0
0,5
1,0
1,5
2,0
2,5
3,0
3,5

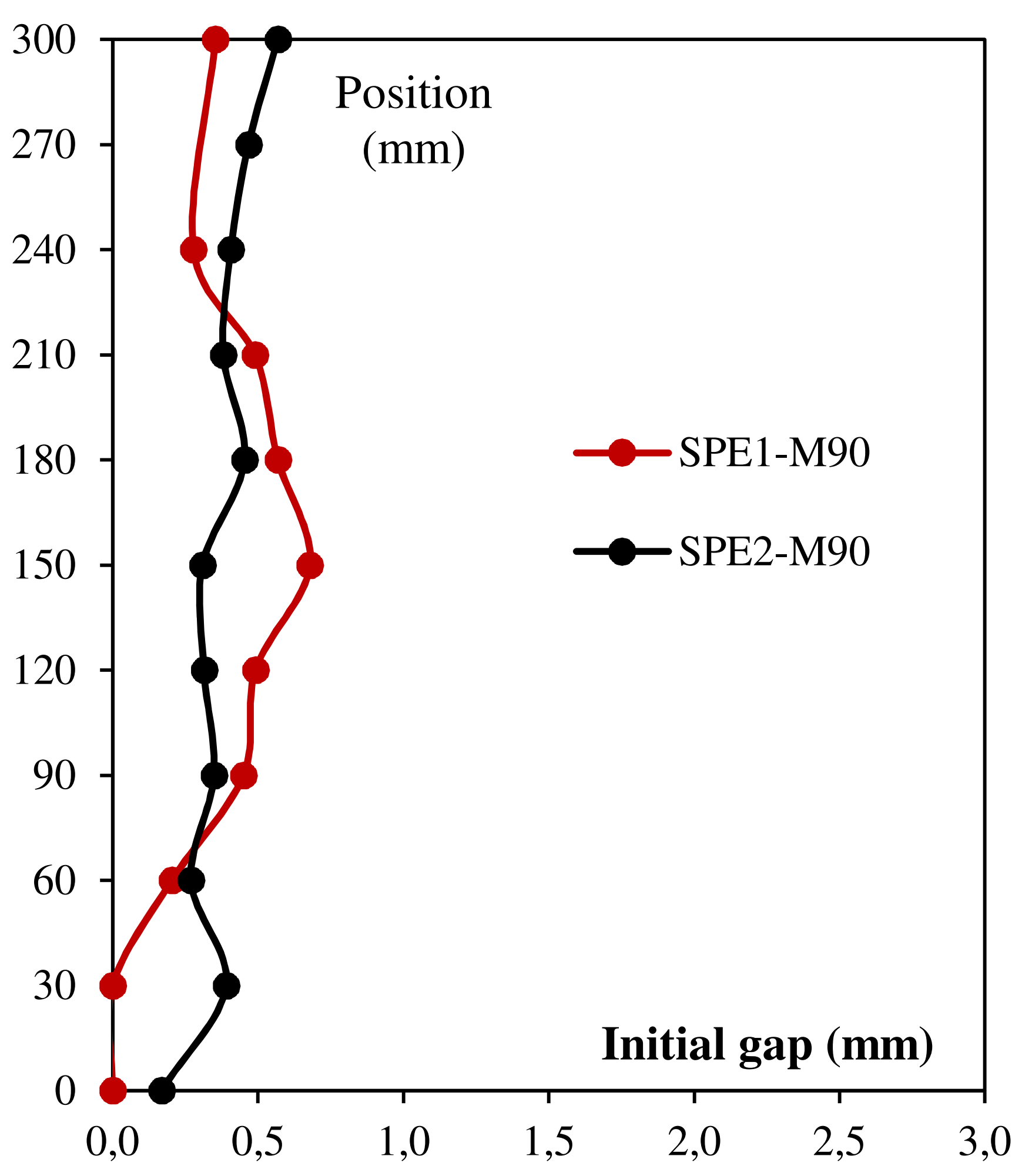
Position
(mm)
300
270
240
210
180
150
120
90
60
30
0
SPE1-M90
SPE2-M90
Initial gap (mm)
0,0
0,5
1,0
1,5
2,0
2,5
3,0

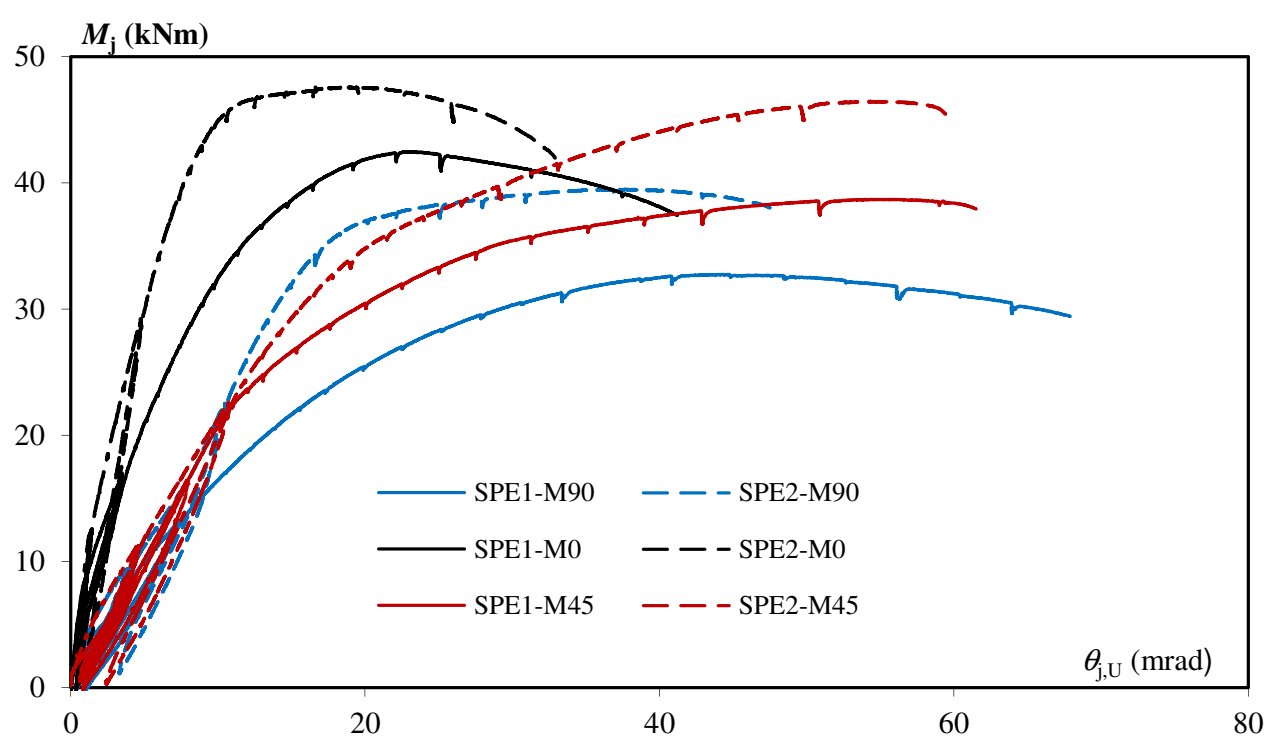
M_j (kNm)
50
40
30
20
10
0
0
20
40
60
80
SPE1-M90
SPE2-M90
SPE1-M0
SPE2-M0
SPE1-M45
SPE2-M45
$\theta_{j,U}$ (mrad)

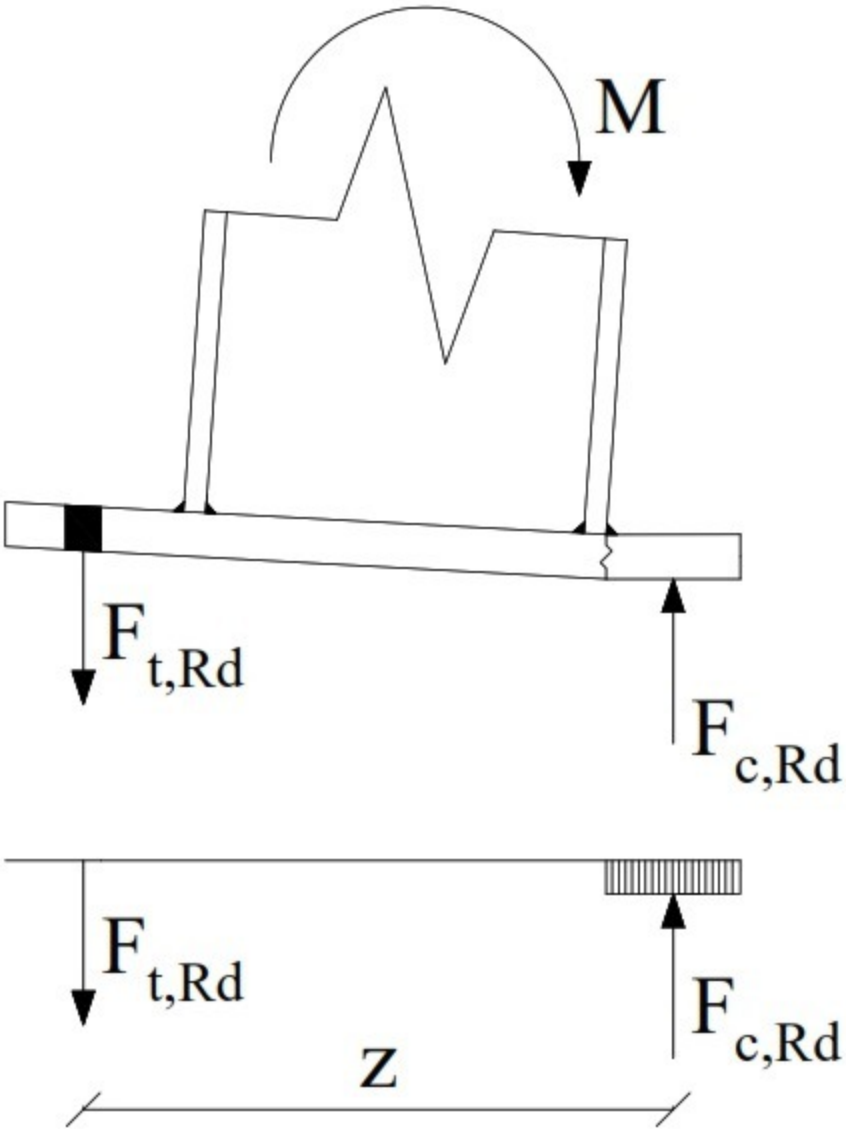
M
F t,Rd
F c,Rd
F t,Rd
F c,Rd
z

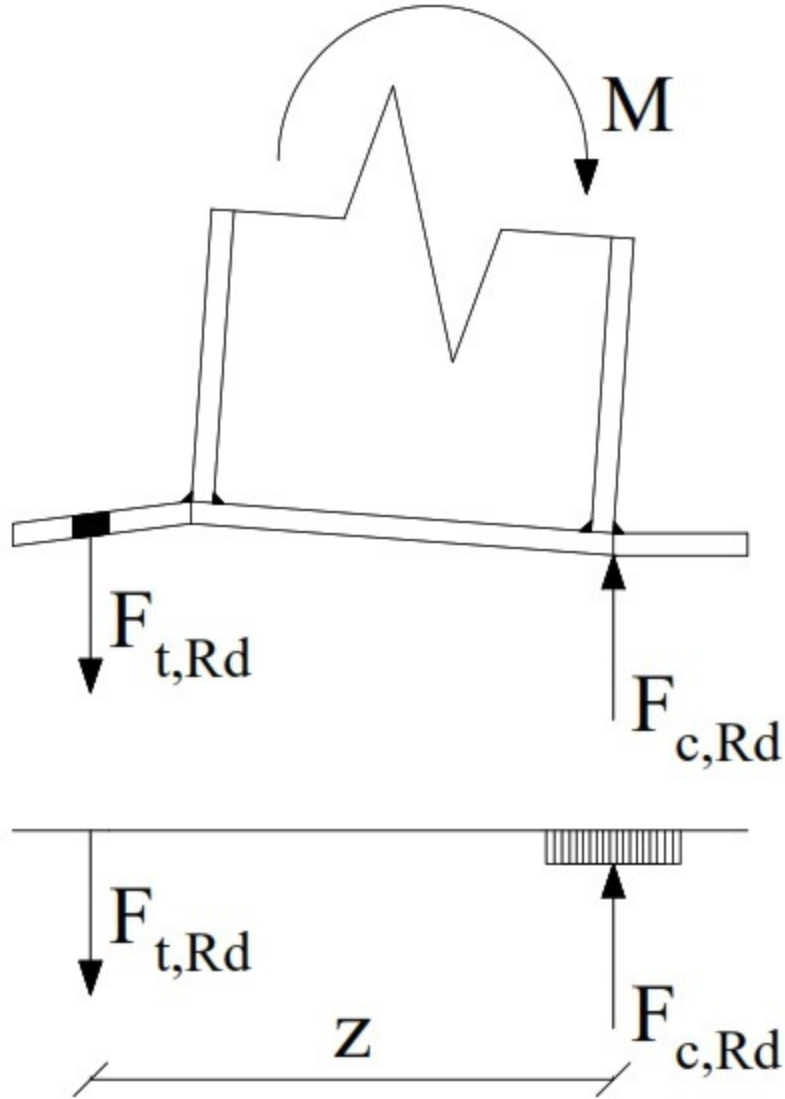
M
F t,Rd
F c,Rd
F t,Rd
F c,Rd
z

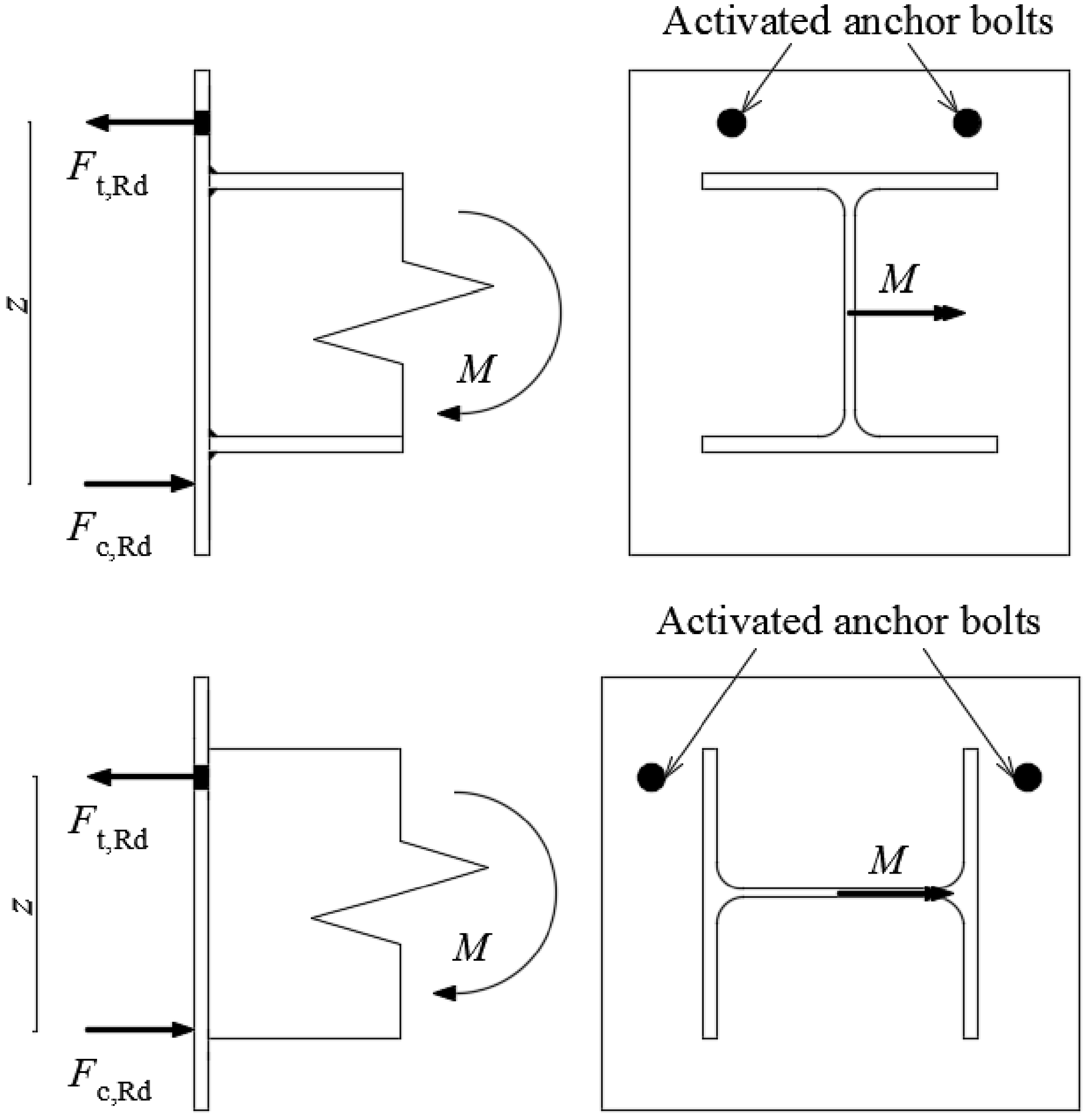
Activated anchor bolts
$F_{t,Rd}$
z
M
$F_{c,Rd}$
M
Activated anchor bolts
$F_{t,Rd}$
z
M
$F_{c,Rd}$
M

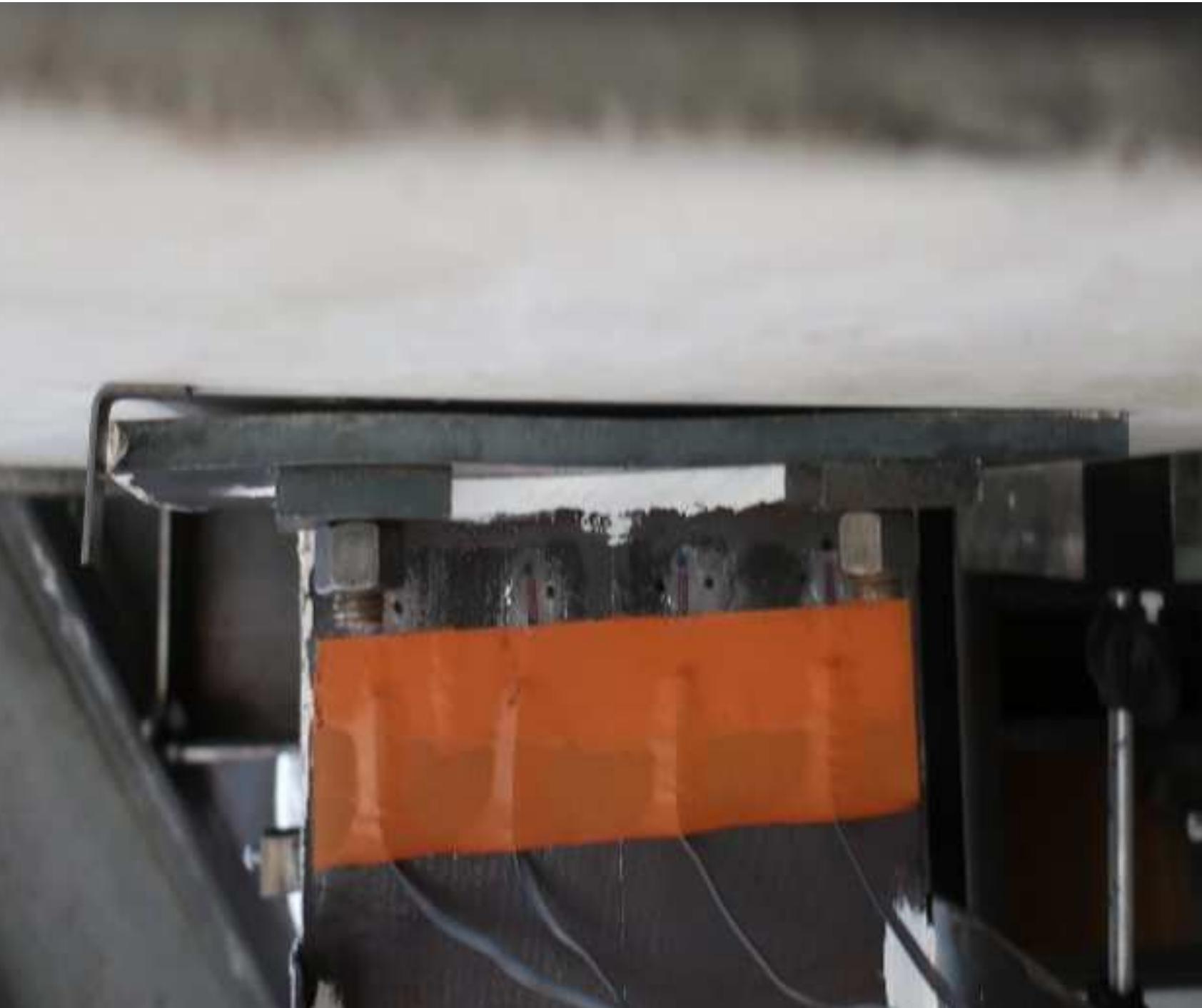

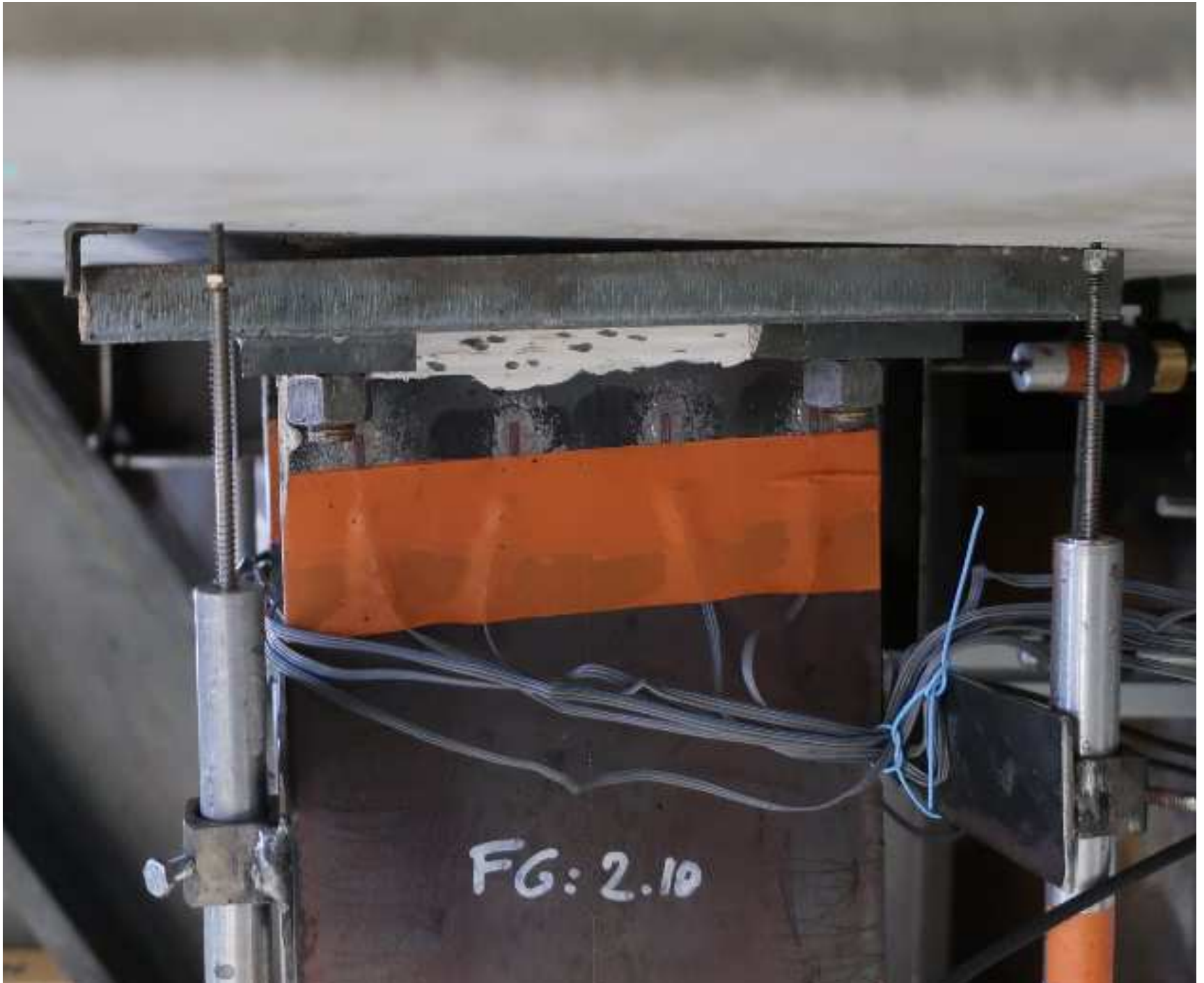
FG: 2.10

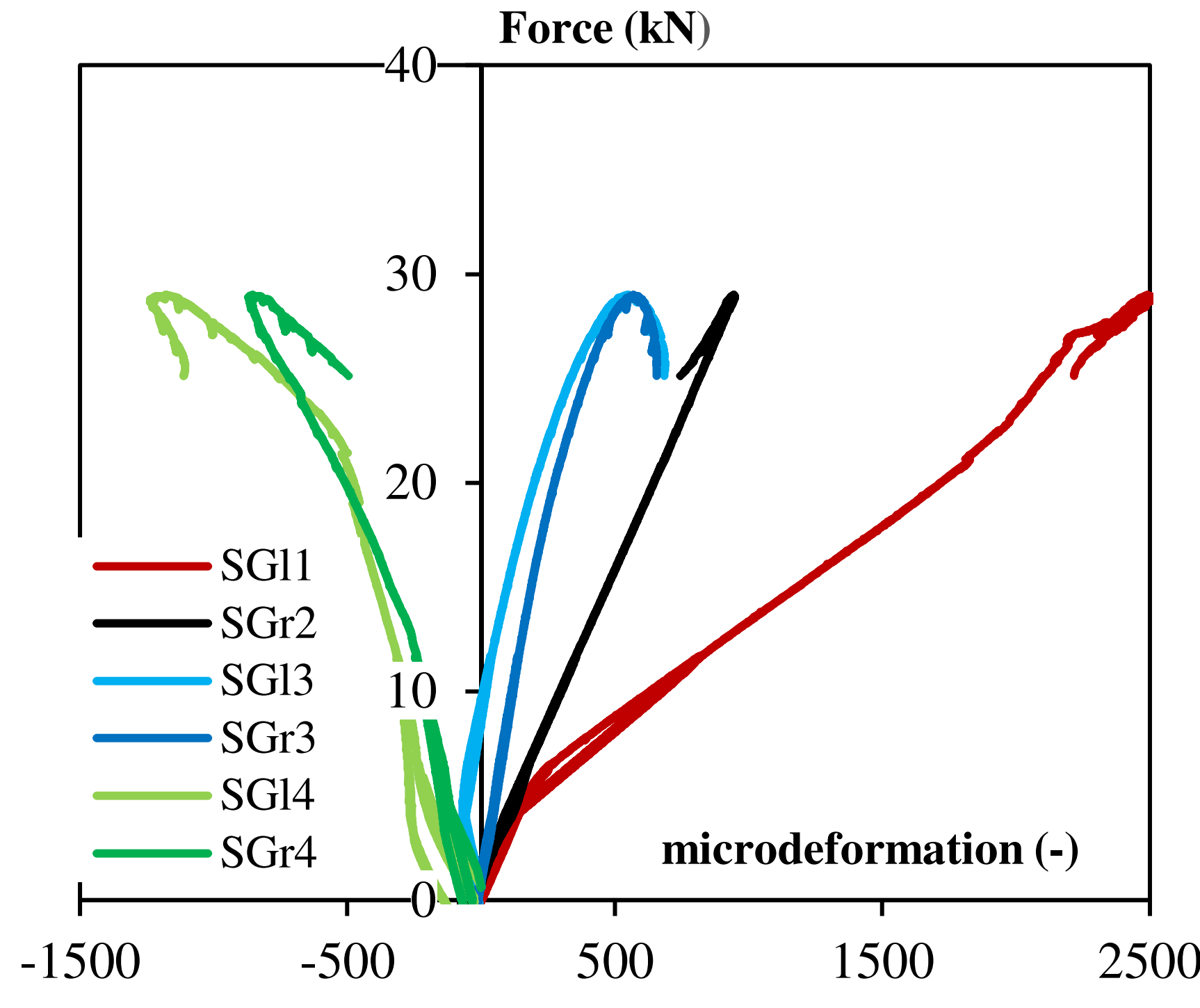
Force (kN)
40
30
20
10
0
-1500
-500
500
1500
2500
SGl1
SGr2
SGl3
SGr3
SGl4
SGr4
microdeformation (-)

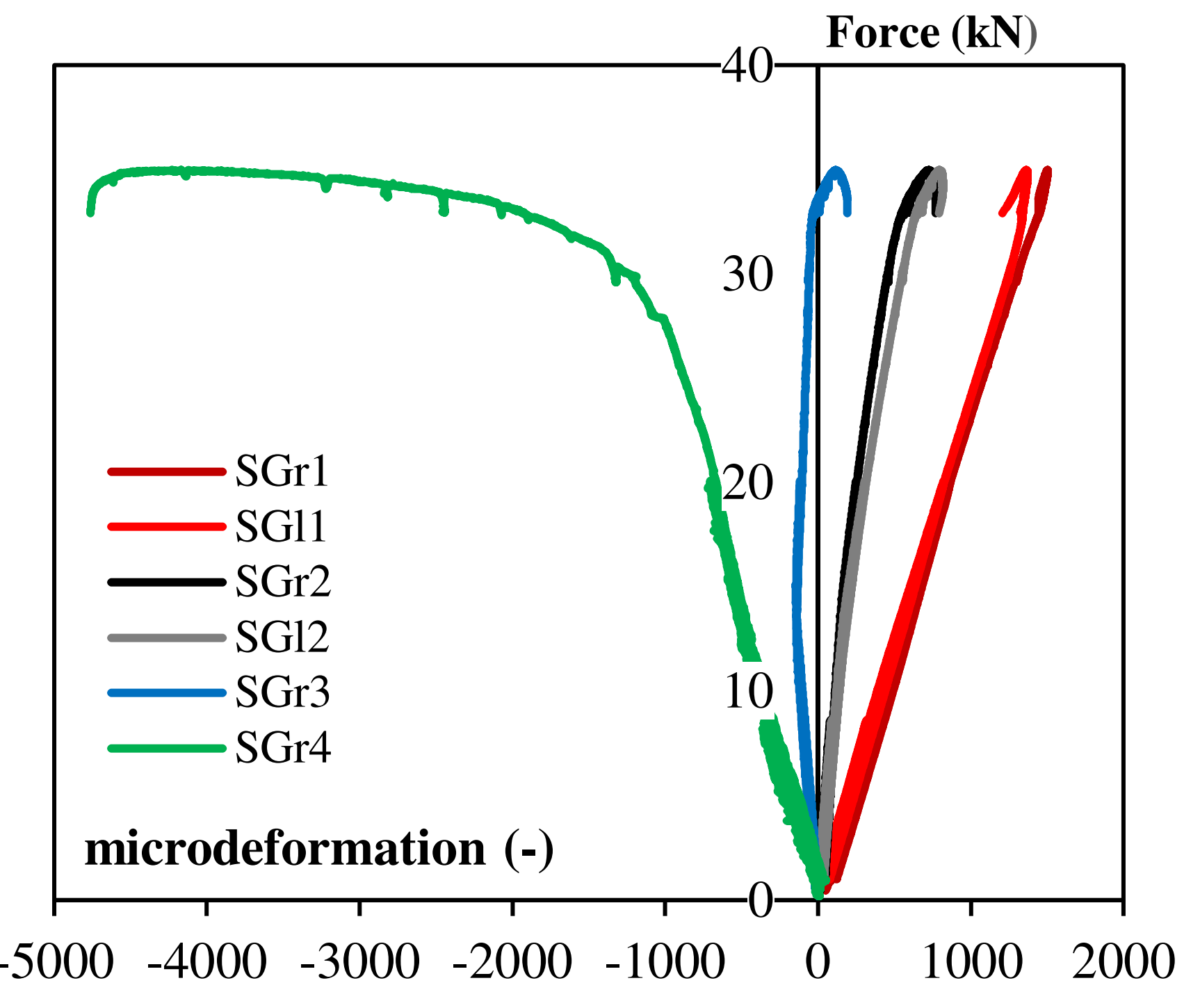
Force (kN)
40
30
20
10
0
SGr1
SGl1
SGr2
SGl2
SGr3
SGr4
microdeformation (-)
-5000
-4000
-3000
-2000
-1000
0
1000
2000

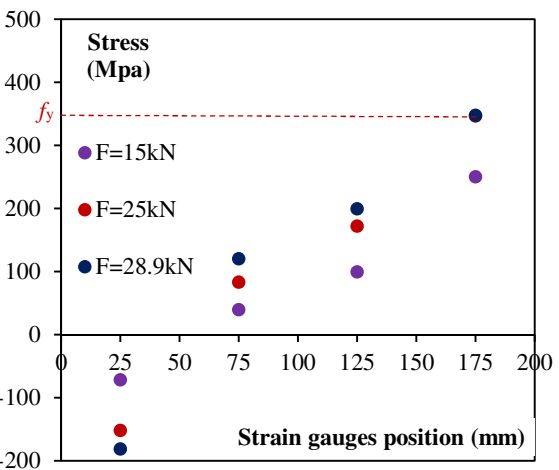
Stress
(Mpa)
f_y
F=15kN
F=25kN
F=28.9kN
500
400
300
200
100
0
-100
-200
0
25
50
75
100
125
150
175
200
Strain gauges position (mm)

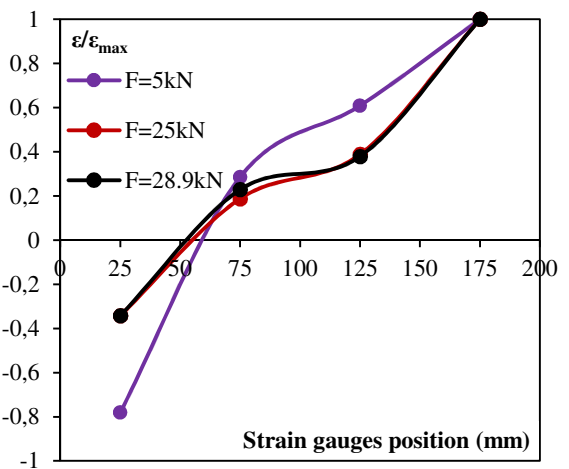
$\varepsilon/\varepsilon_{max}$
F=5kN
F=25kN
F=28.9kN
1
0,8
0,6
0,4
0,2
0
-0,2
-0,4
-0,6
-0,8
-1
0
25
50
75
100
125
150
175
200
Strain gauges position (mm)

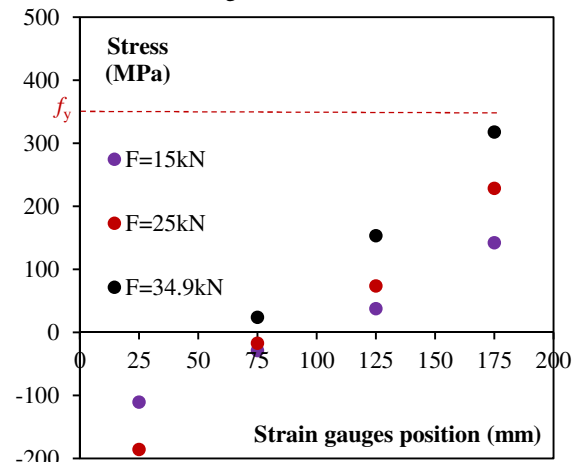
Stress
(MPa)
f_y
F=15kN
F=25kN
F=34.9kN
500
400
300
200
100
0
-100
-200
0
25
50
75
100
125
150
175
200
Strain gauges position (mm)

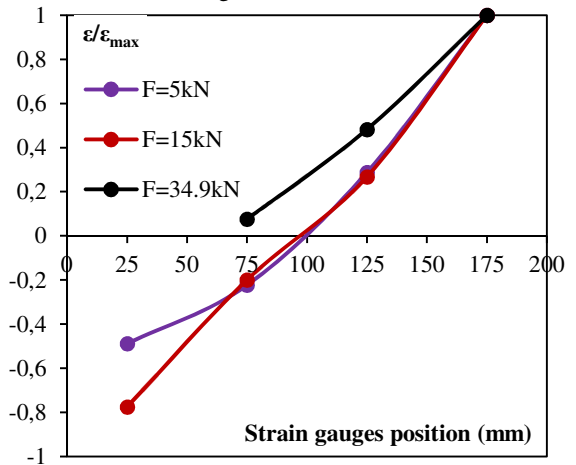
$\varepsilon/\varepsilon_{max}$
F=5kN
F=15kN
F=34.9kN
1
0,8
0,6
0,4
0,2
0
-0,2
-0,4
-0,6
-0,8
-1
0
25
50
75
100
125
150
175
200
Strain gauges position (mm)

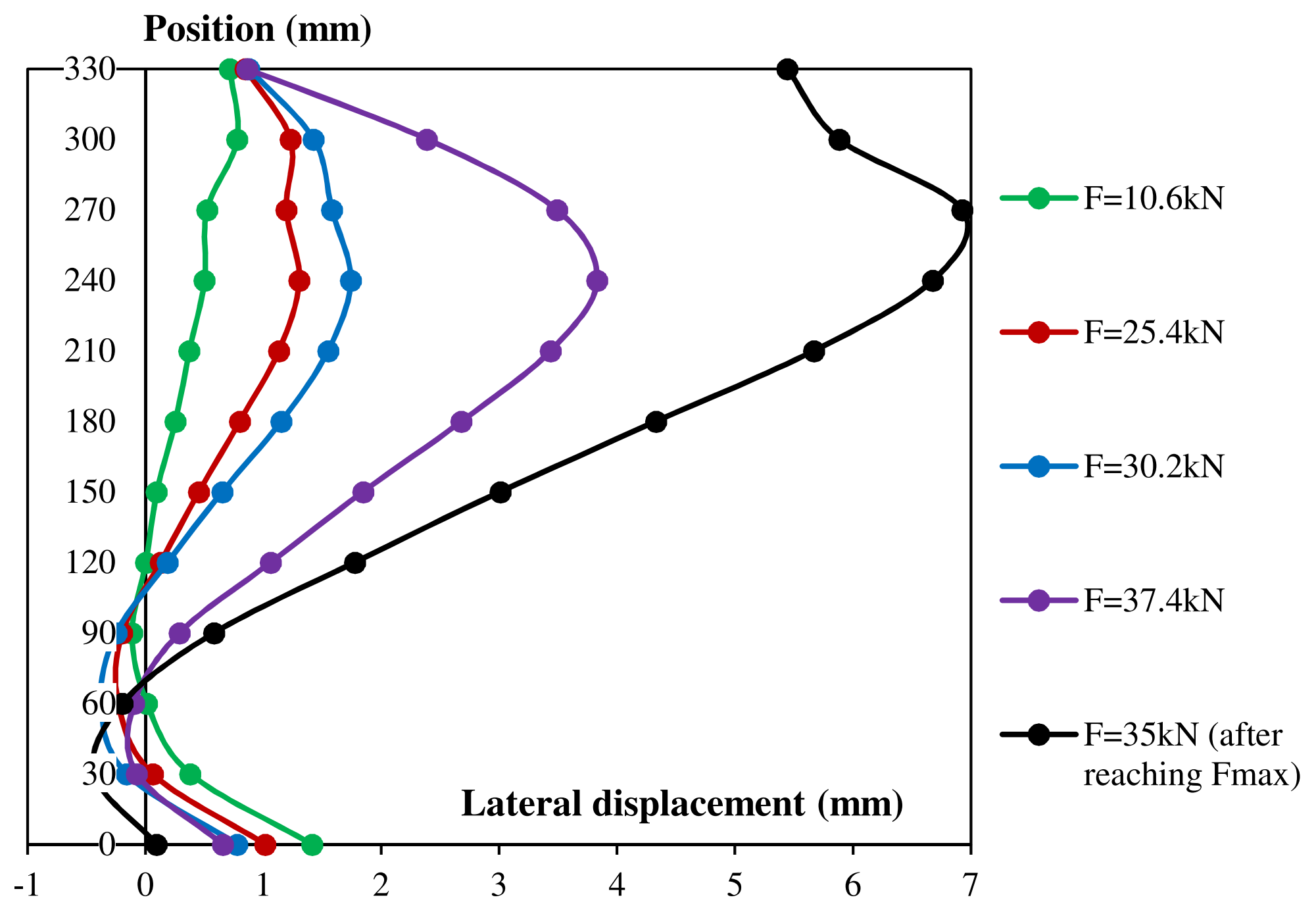
Position (mm)
330
300
270
240
210
180
150
120
90
60
30
0
-1
0
1
2
3
4
5
6
7
Lateral displacement (mm)
F=10.6kN
F=25.4kN
F=30.2kN
F=37.4kN
F=35kN (after reaching Fmax)

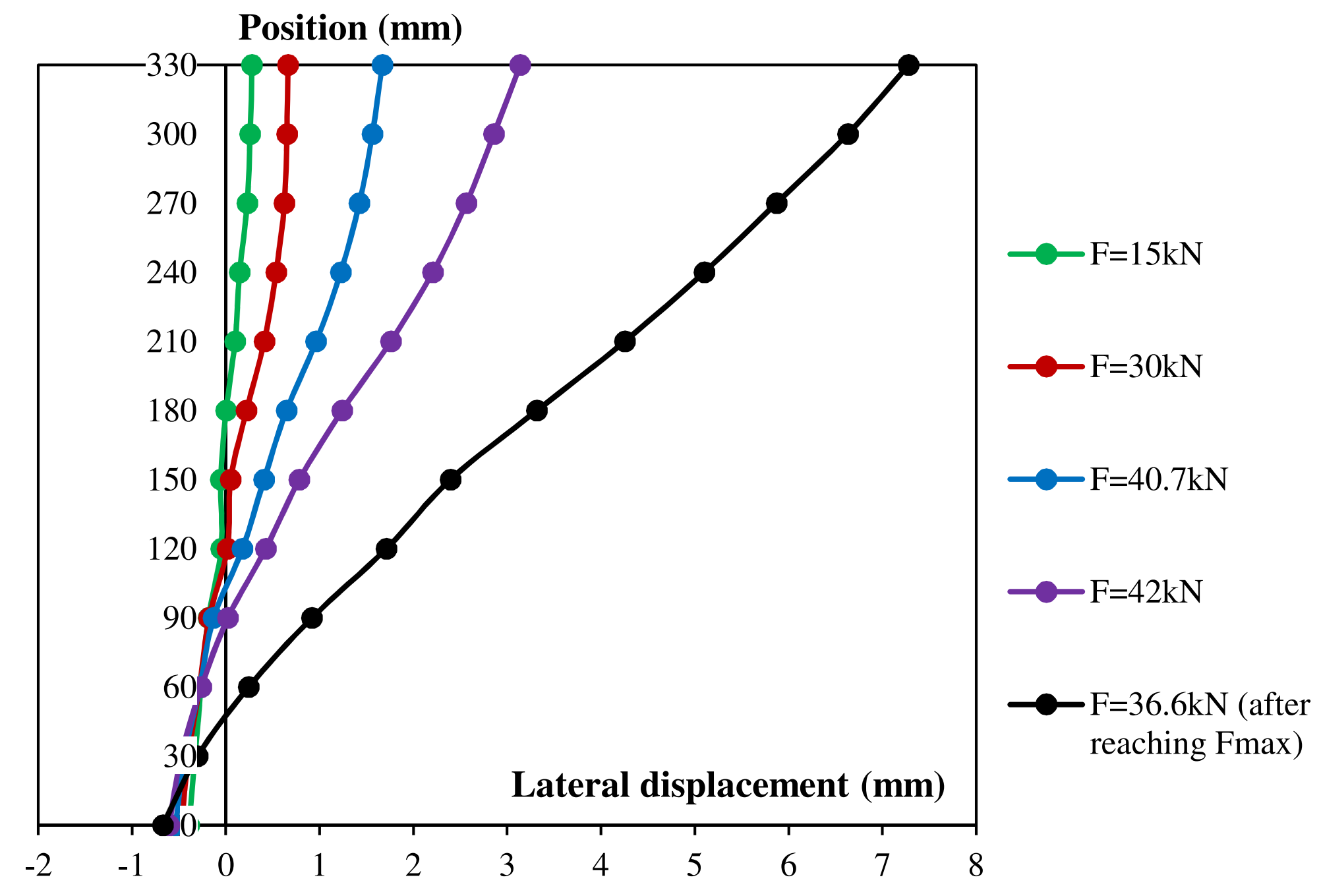
Position (mm)
330
300
270
240
210
180
150
120
90
60
30
0
-2
-1
0
1
2
3
4
5
6
7
8
Lateral displacement (mm)
F=15kN
F=30kN
F=40.7kN
F=42kN
F=36.6kN (after reaching Fmax)

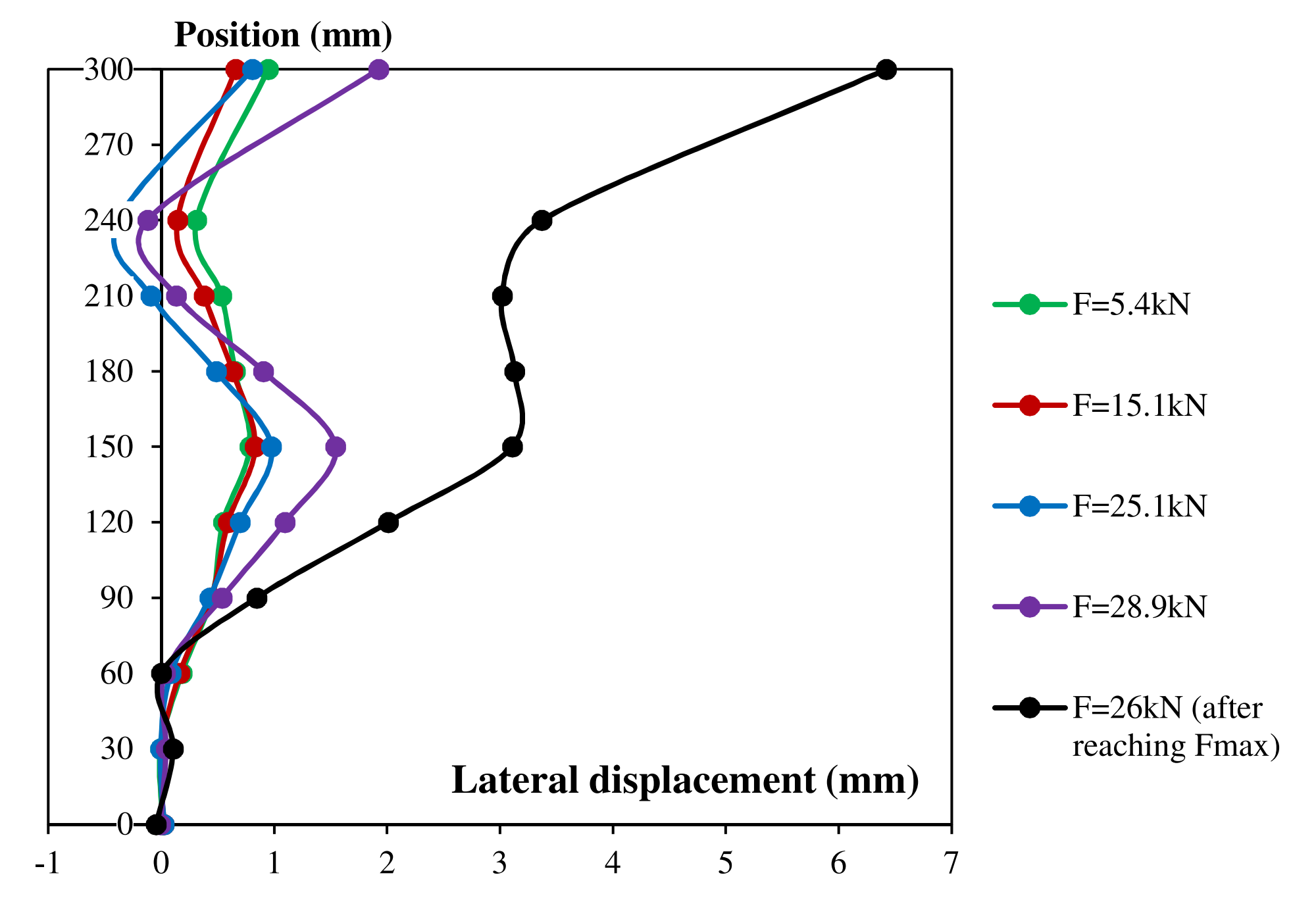
Position (mm)
300
270
240
210
180
150
120
90
60
30
0
-1
0
1
2
3
4
5
6
7
Lateral displacement (mm)
F=5.4kN
F=15.1kN
F=25.1kN
F=28.9kN
F=26kN (after reaching Fmax)

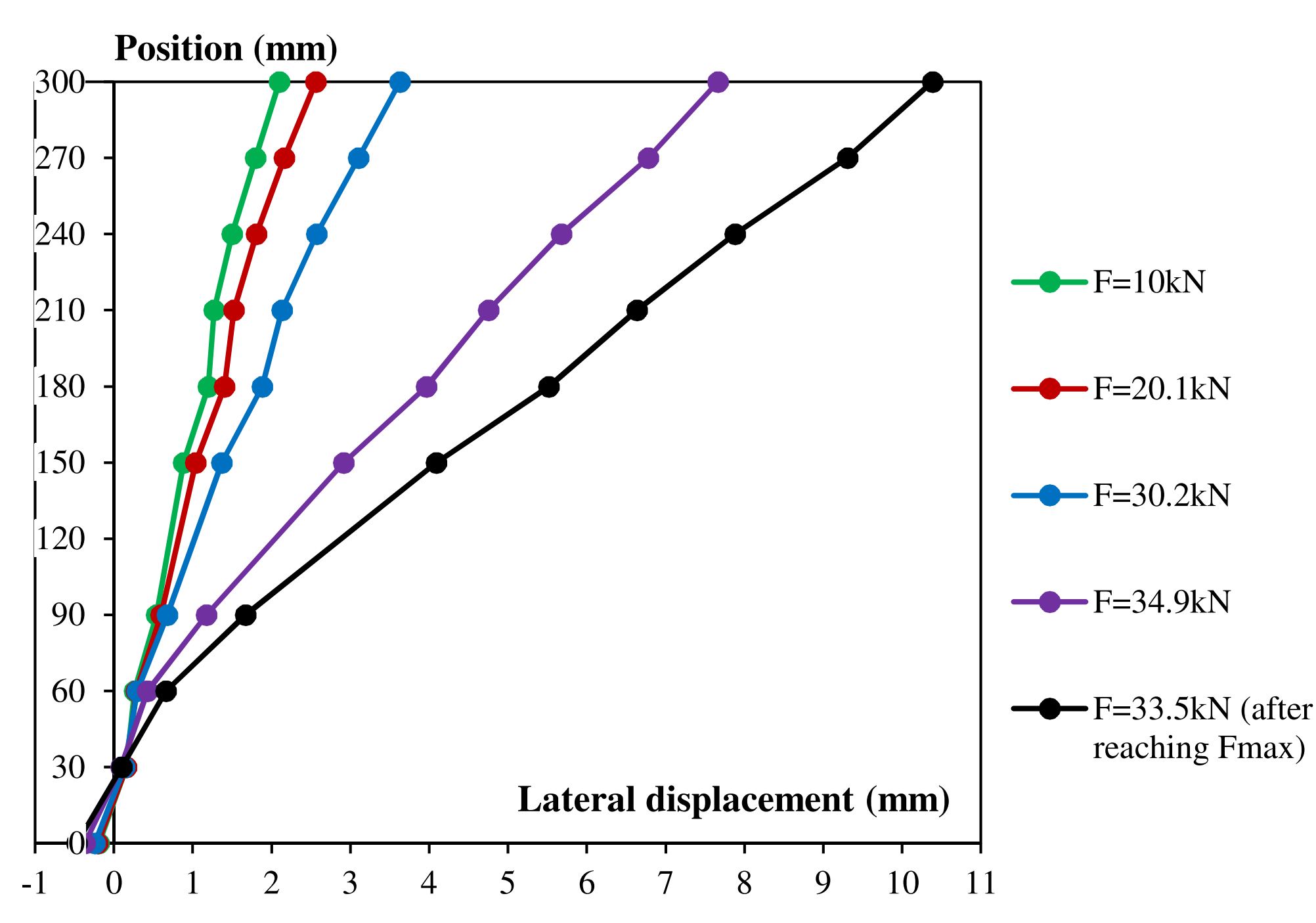
Position (mm)
300
270
240
210
180
150
120
90
60
30
0
-1
0
1
2
3
4
5
6
7
8
9
10
11
Lateral displacement (mm)
F=10kN
F=20.1kN
F=30.2kN
F=34.9kN
F=33.5kN (after reaching Fmax)

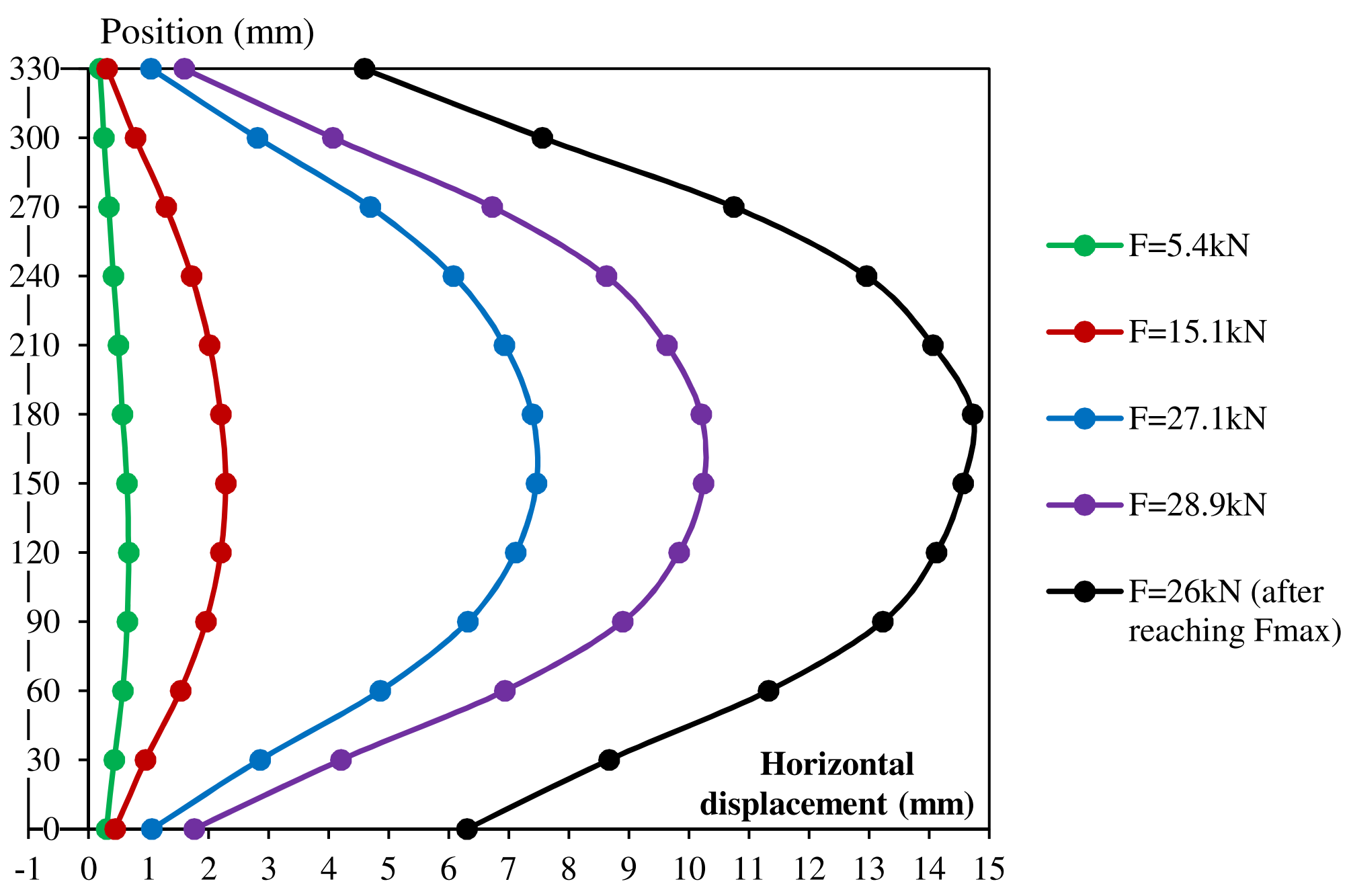
Position (mm)
330
300
270
240
210
180
150
120
90
60
30
0
-1
0
1
2
3
4
5
6
7
8
9
10
11
12
13
14
15
Horizontal displacement (mm)
F=5.4kN
F=15.1kN
F=27.1kN
F=28.9kN
F=26kN (after reaching Fmax)

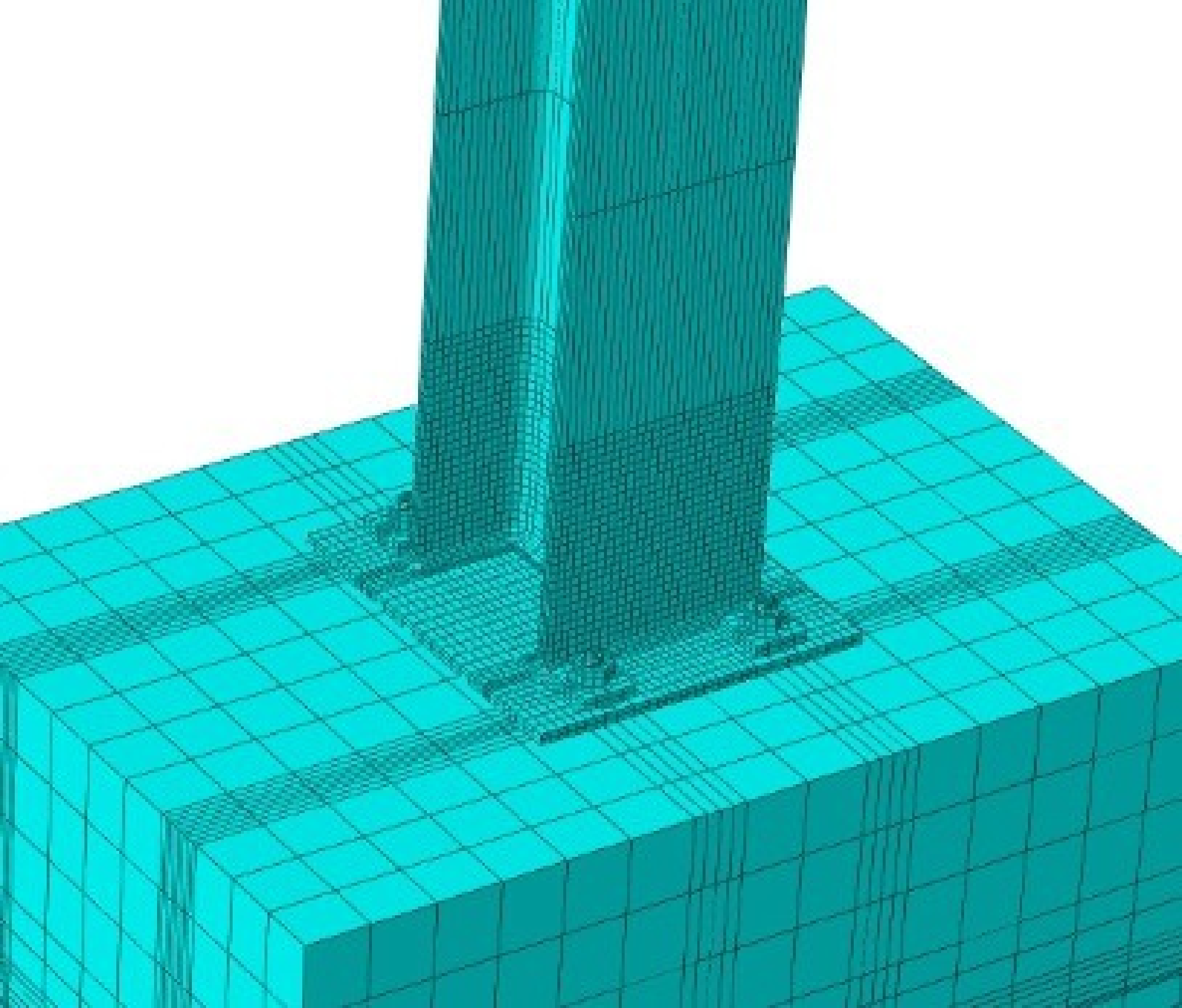

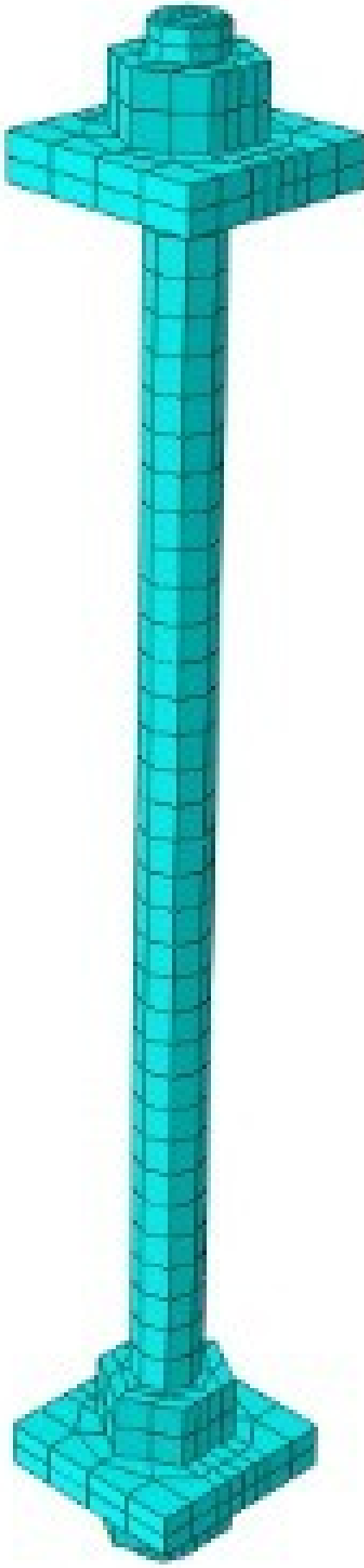

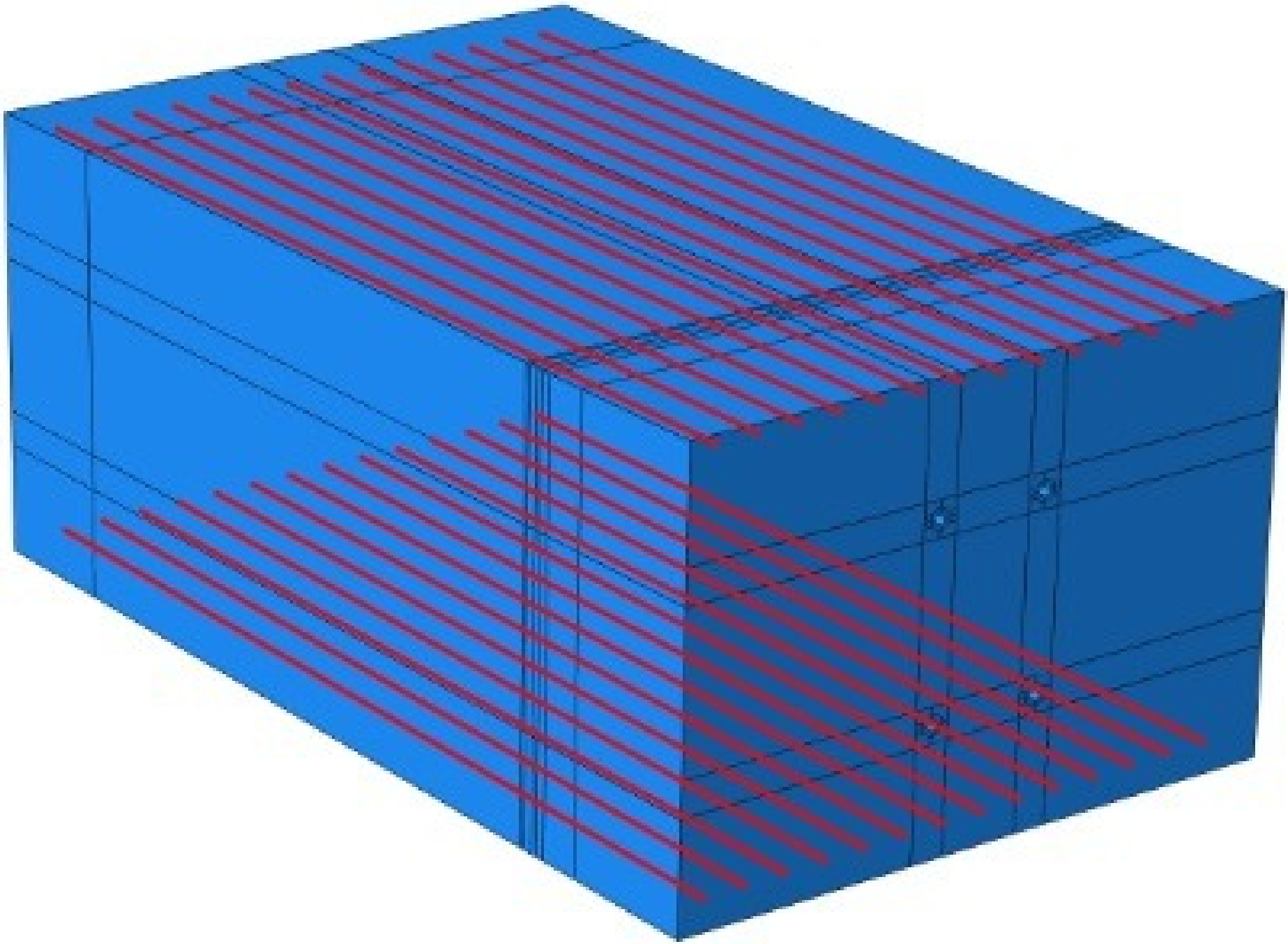

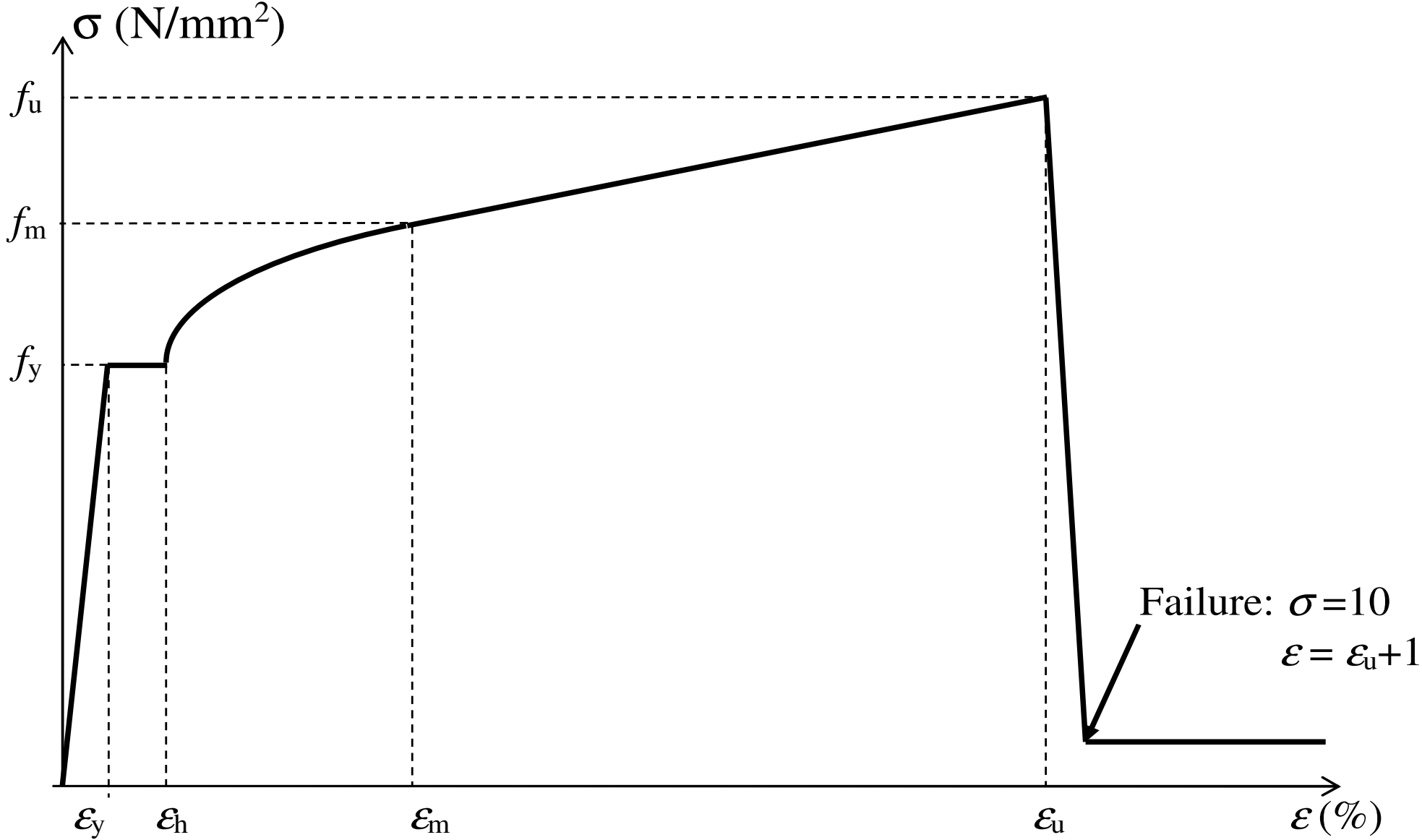
σ (N/mm²)
f_u
f_m
f_y
Failure: σ=10
$\varepsilon = \varepsilon_u$+1
ε_y
ε_h
ε_m
ε_u
ε (%)

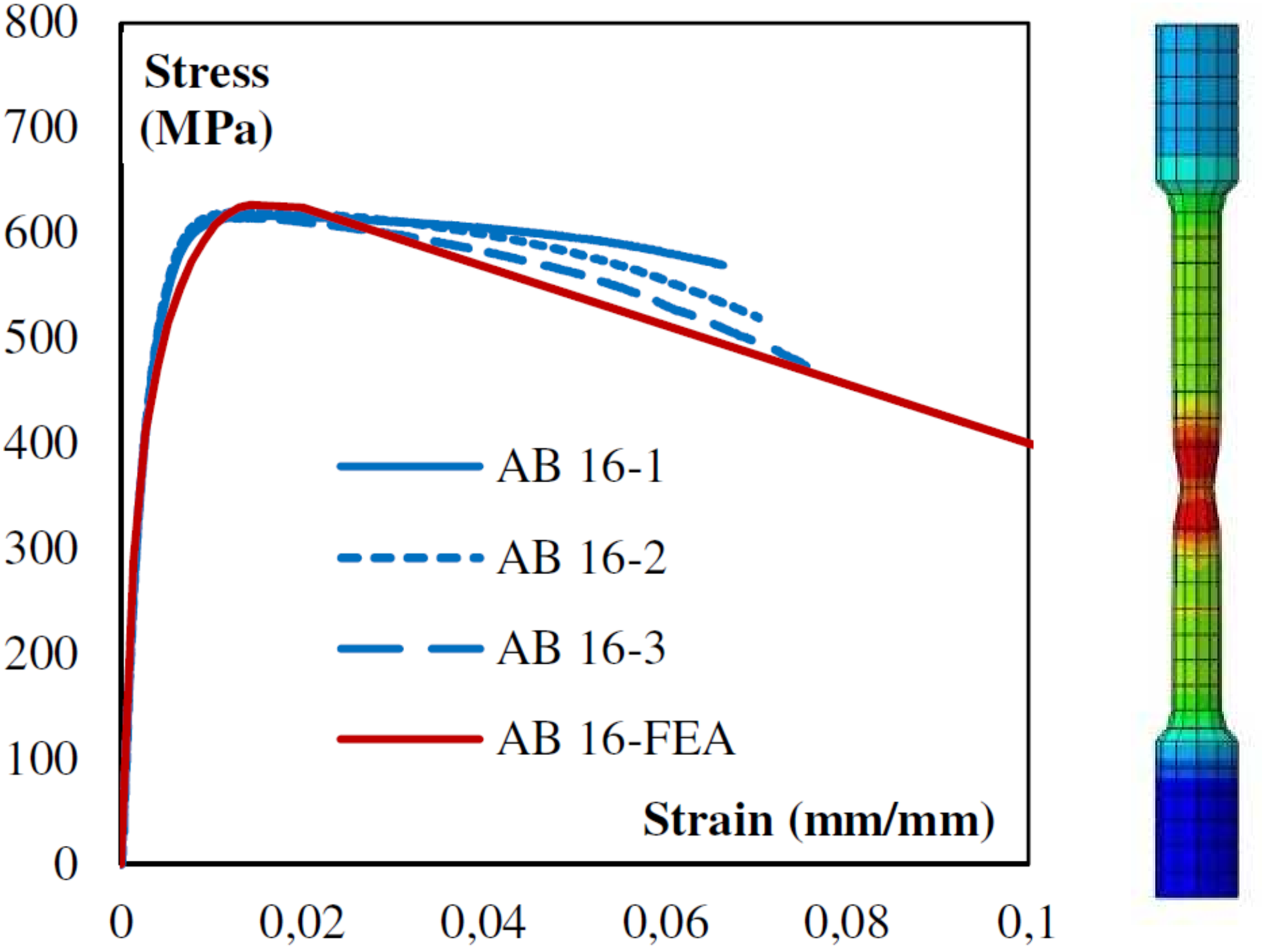
800
700
600
500
400
300
200
100
0
Stress
(MPa)
AB 16-1
AB 16-2
AB 16-3
AB 16-FEA
Strain (mm/mm)
0
0,02
0,04
0,06
0,08
0,1

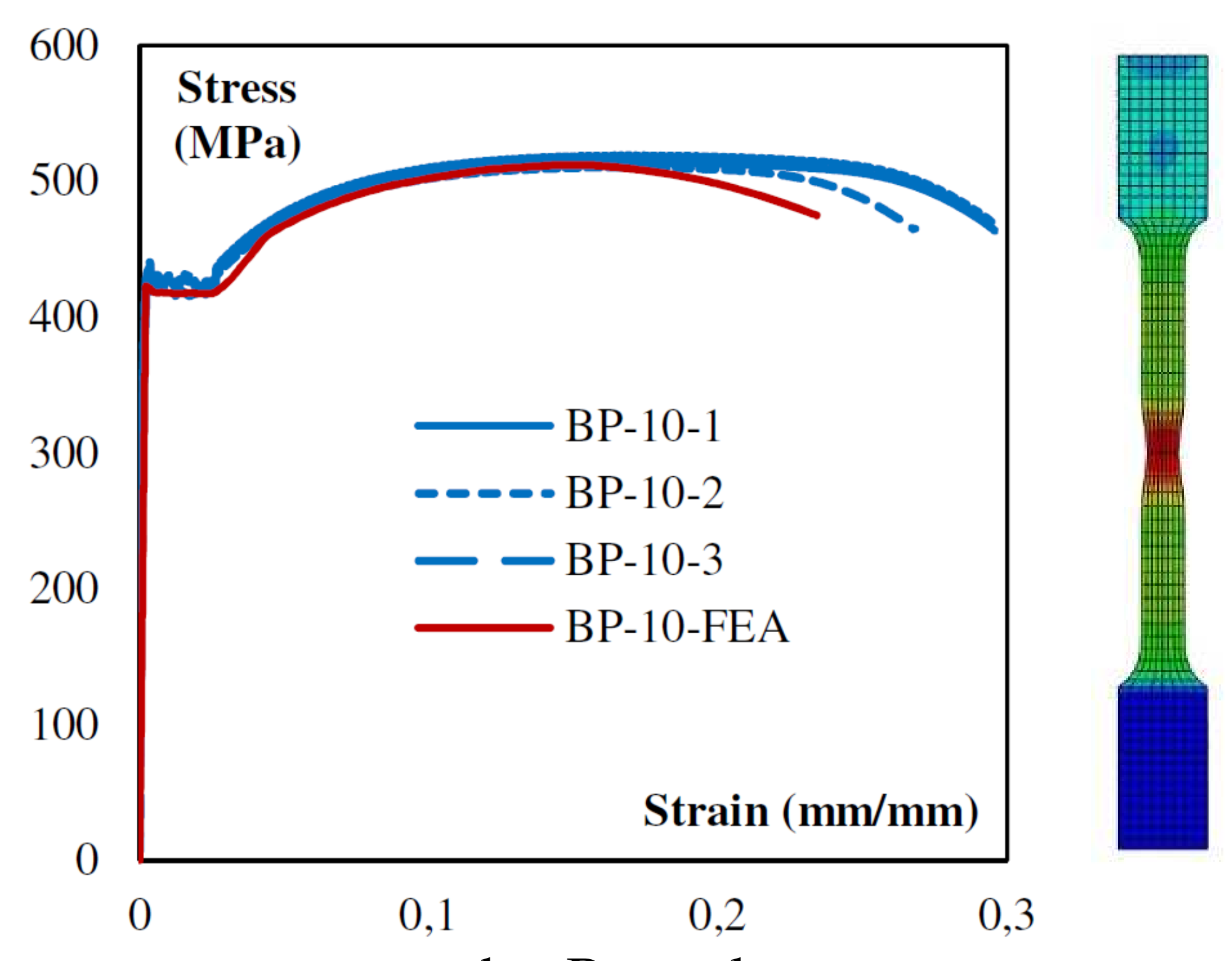
600
500
400
300
200
100
0
Stress
(MPa)
BP-10-1
BP-10-2
BP-10-3
BP-10-FEA
Strain (mm/mm)
0
0,1
0,2
0,3

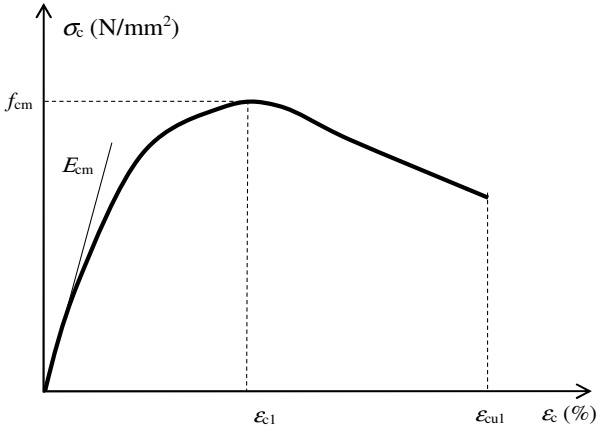
σc (N/mm2)
fcm
Ecm
εc1
εcu1
εc (%)

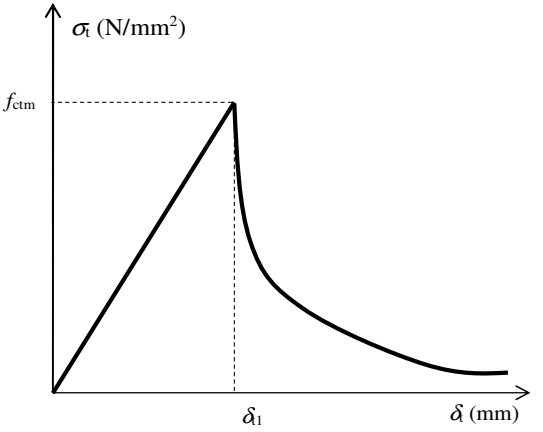
σt (N/mm2)
fctm
δ1
δ (mm)

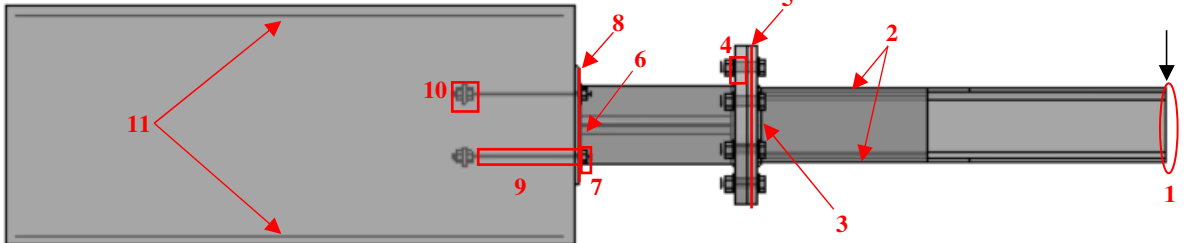
11
10
8
6
9
7
4
5
2
3
1

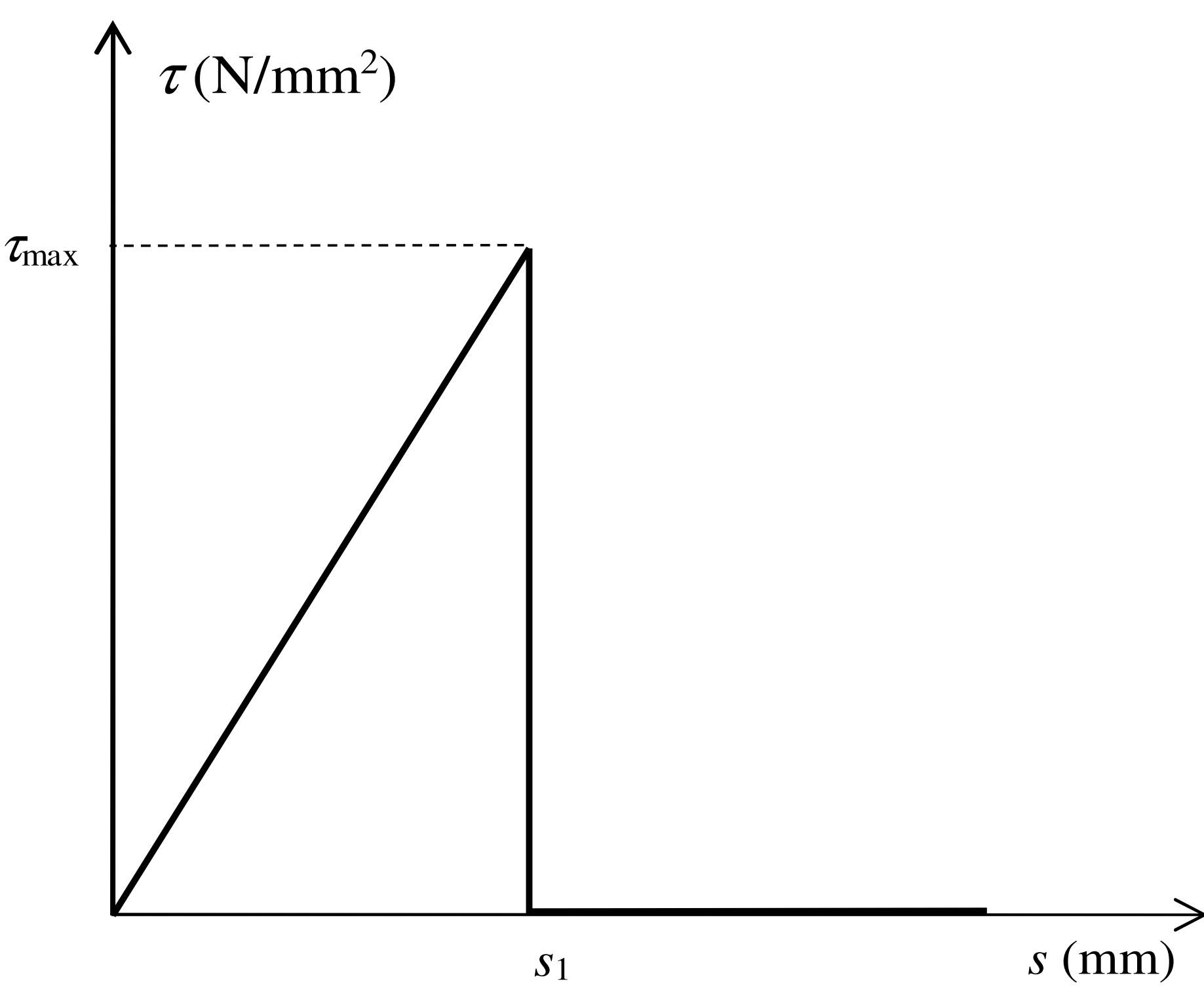
τ (N/mm^2)
τ_{max}
s_1
s (mm)

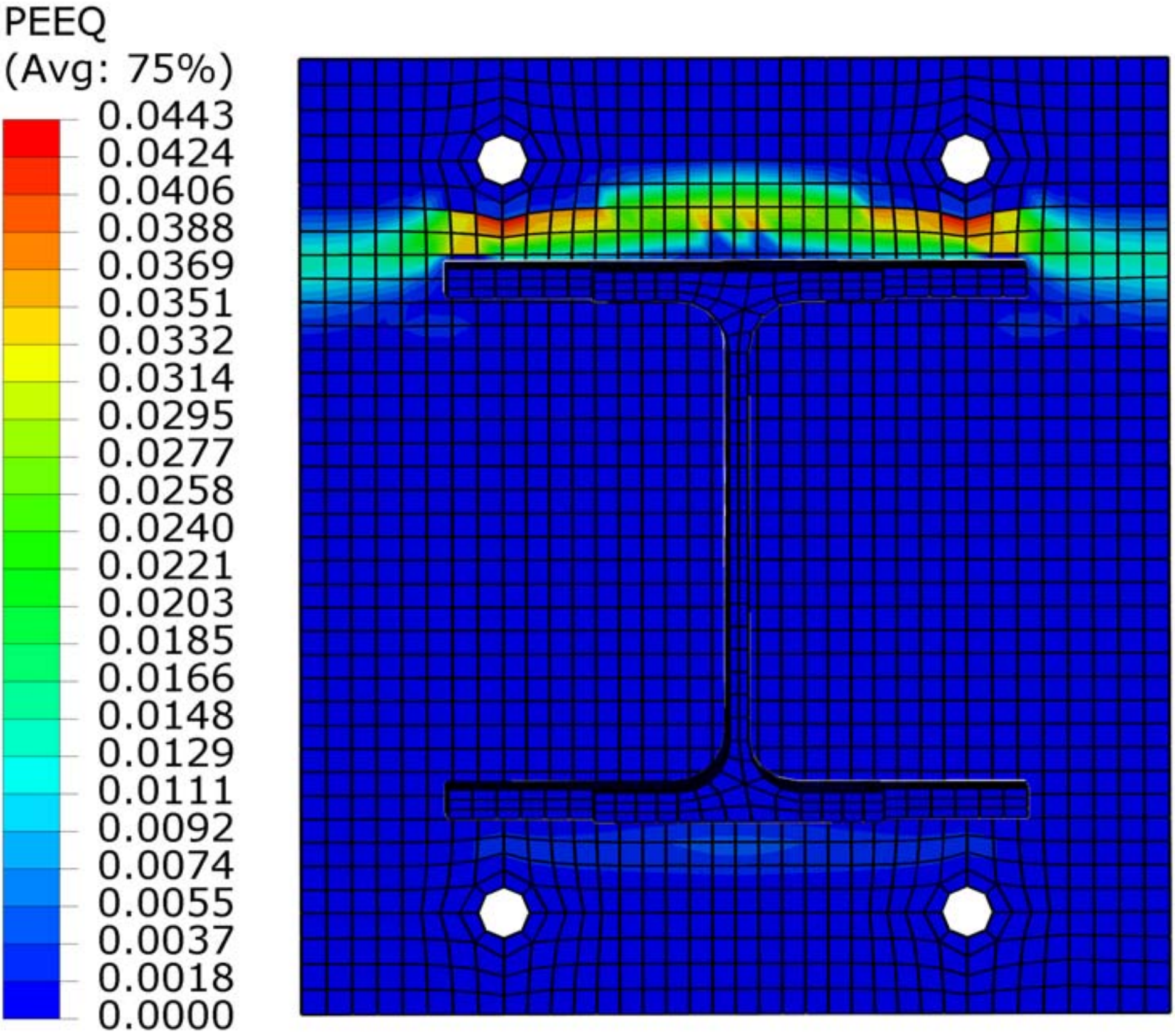
PEEQ
(Avg: 75%)
0.0443
0.0424
0.0406
0.0388
0.0369
0.0351
0.0332
0.0314
0.0295
0.0277
0.0258
0.0240
0.0221
0.0203
0.0185
0.0166
0.0148
0.0129
0.0111
0.0092
0.0074
0.0055
0.0037
0.0018
0.0000

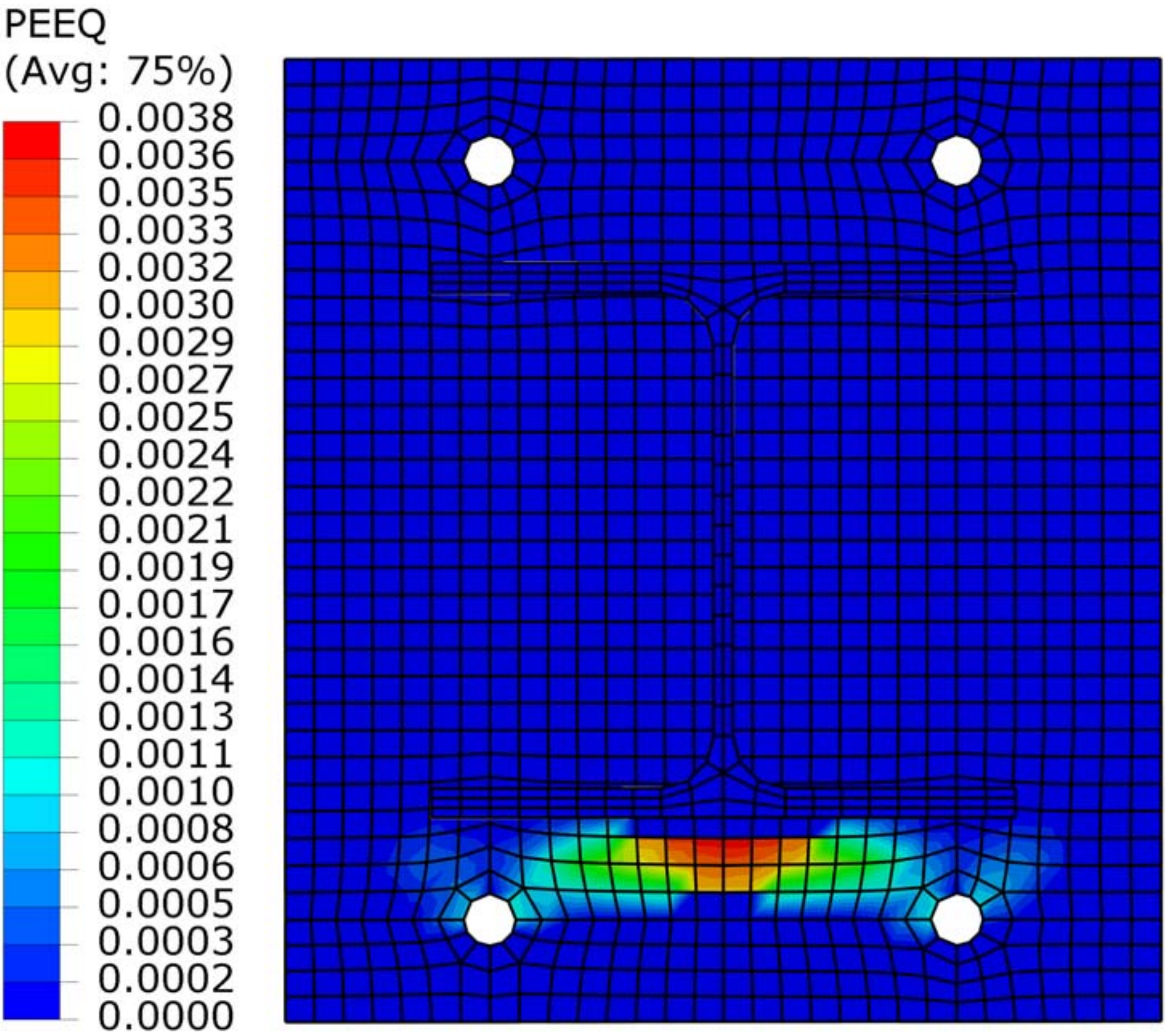
PEEQ
(Avg: 75%)
0.0038
0.0036
0.0035
0.0033
0.0032
0.0030
0.0029
0.0027
0.0025
0.0024
0.0022
0.0021
0.0019
0.0017
0.0016
0.0014
0.0013
0.0011
0.0010
0.0008
0.0006
0.0005
0.0003
0.0002
0.0000

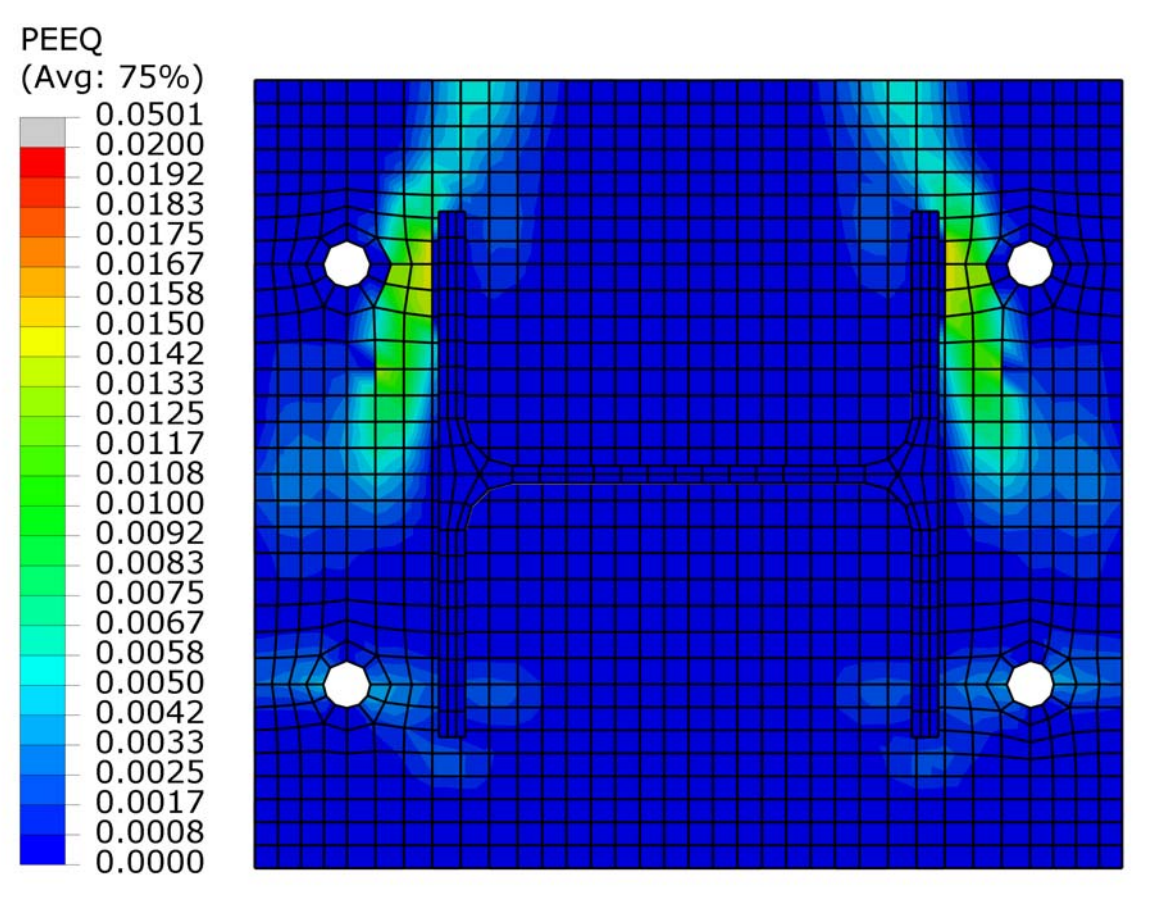
PEEQ
(Avg: 75%)
0.0501
0.0200
0.0192
0.0183
0.0175
0.0167
0.0158
0.0150
0.0142
0.0133
0.0125
0.0117
0.0108
0.0100
0.0092
0.0083
0.0075
0.0067
0.0058
0.0050
0.0042
0.0033
0.0025
0.0017
0.0008
0.0000

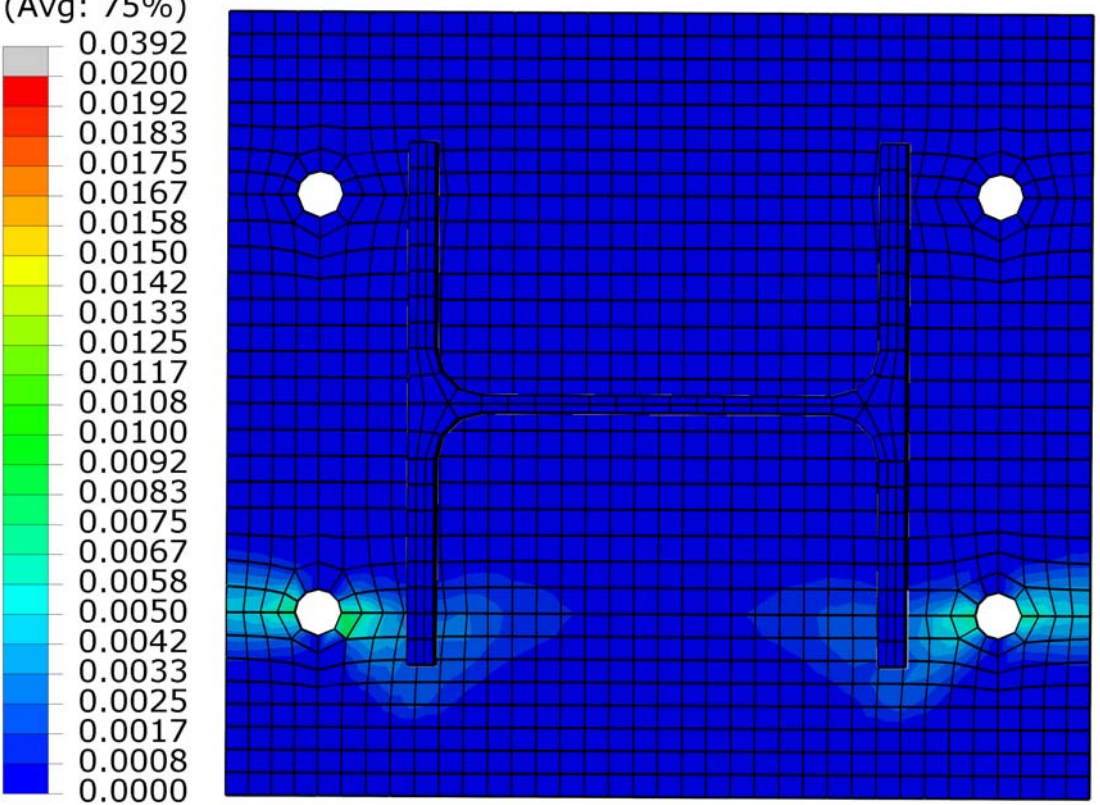
PEEQ
(Avg: 75%)
0.0392
0.0200
0.0192
0.0183
0.0175
0.0167
0.0158
0.0150
0.0142
0.0133
0.0125
0.0117
0.0108
0.0100
0.0092
0.0083
0.0075
0.0067
0.0058
0.0050
0.0042
0.0033
0.0025
0.0017
0.0008
0.0000

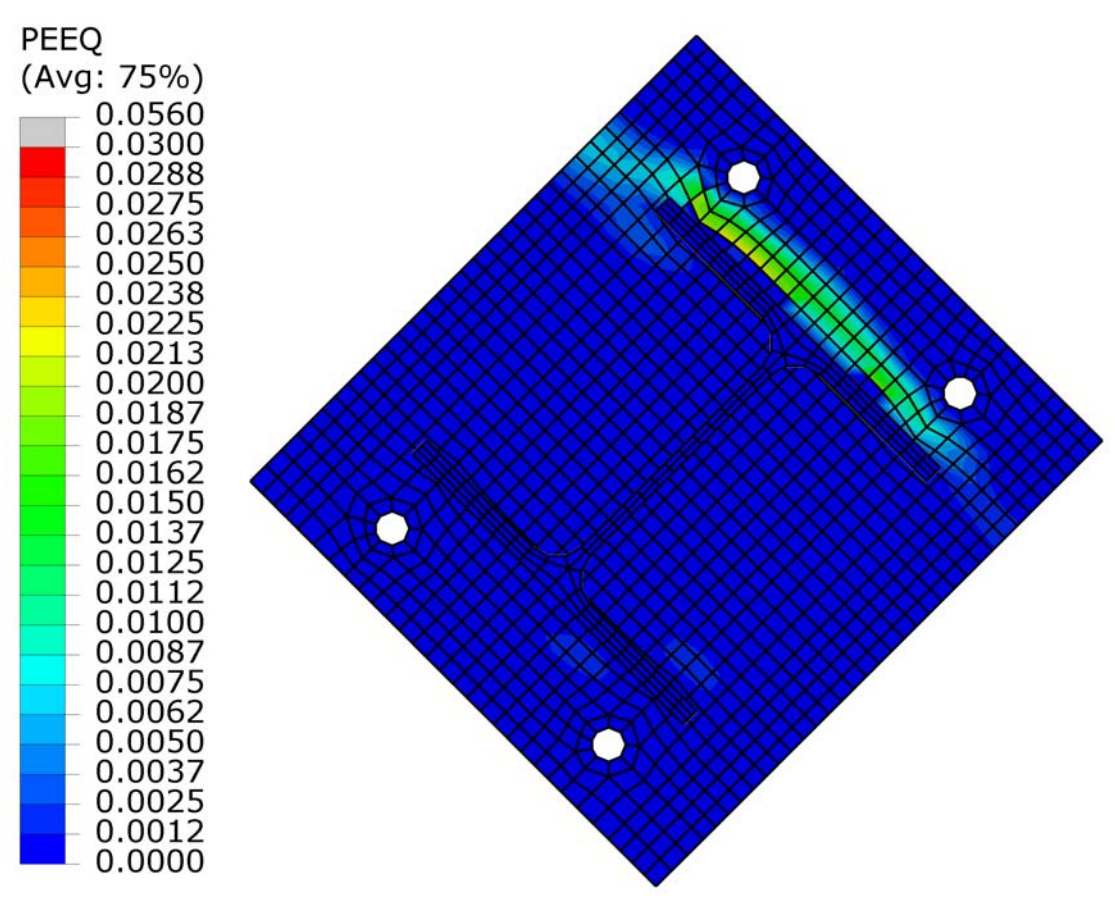
PEEQ
(Avg: 75%)
0.0560
0.0300
0.0288
0.0275
0.0263
0.0250
0.0238
0.0225
0.0213
0.0200
0.0187
0.0175
0.0162
0.0150
0.0137
0.0125
0.0112
0.0100
0.0087
0.0075
0.0062
0.0050
0.0037
0.0025
0.0012
0.0000

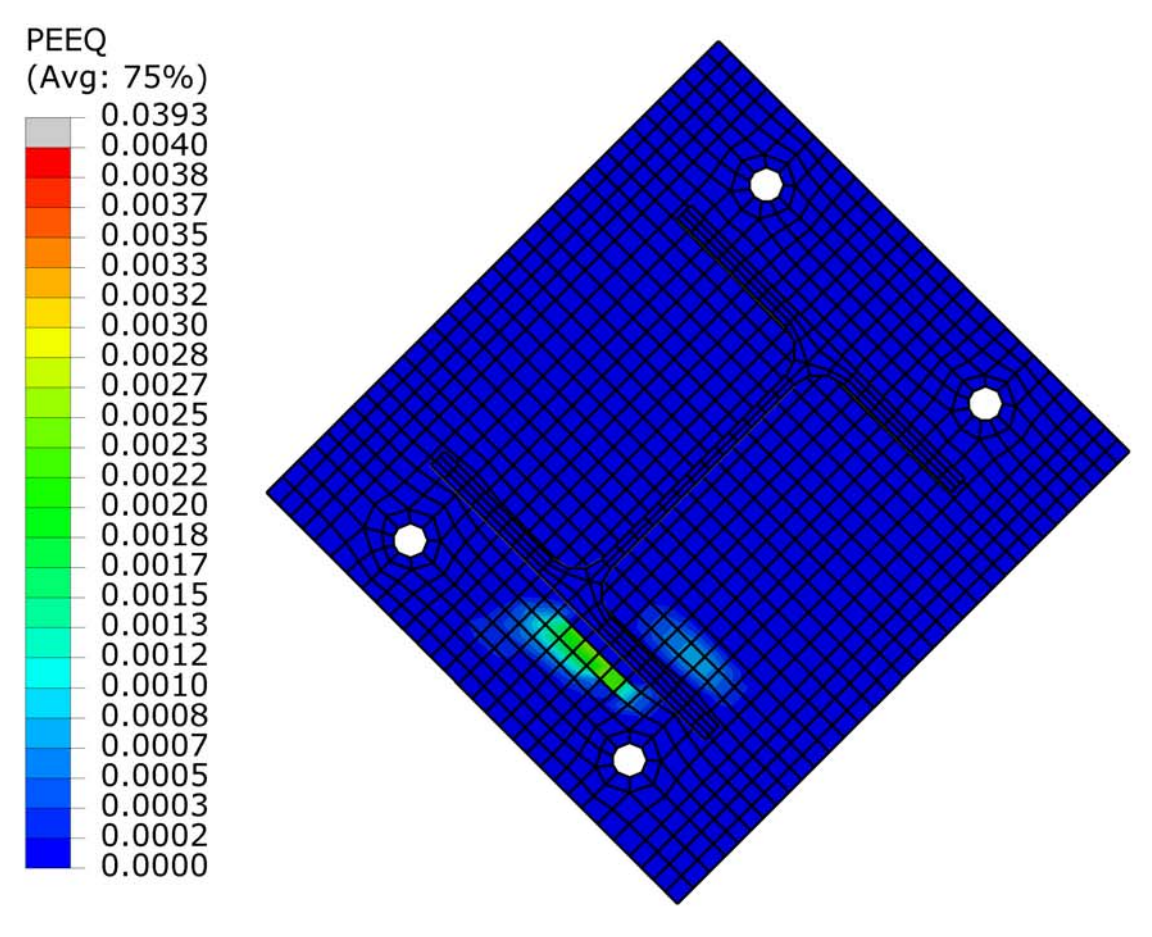
PEEQ
(Avg: 75%)
0.0393
0.0040
0.0038
0.0037
0.0035
0.0033
0.0032
0.0030
0.0028
0.0027
0.0025
0.0023
0.0022
0.0020
0.0018
0.0017
0.0015
0.0013
0.0012
0.0010
0.0008
0.0007
0.0005
0.0003
0.0002
0.0000

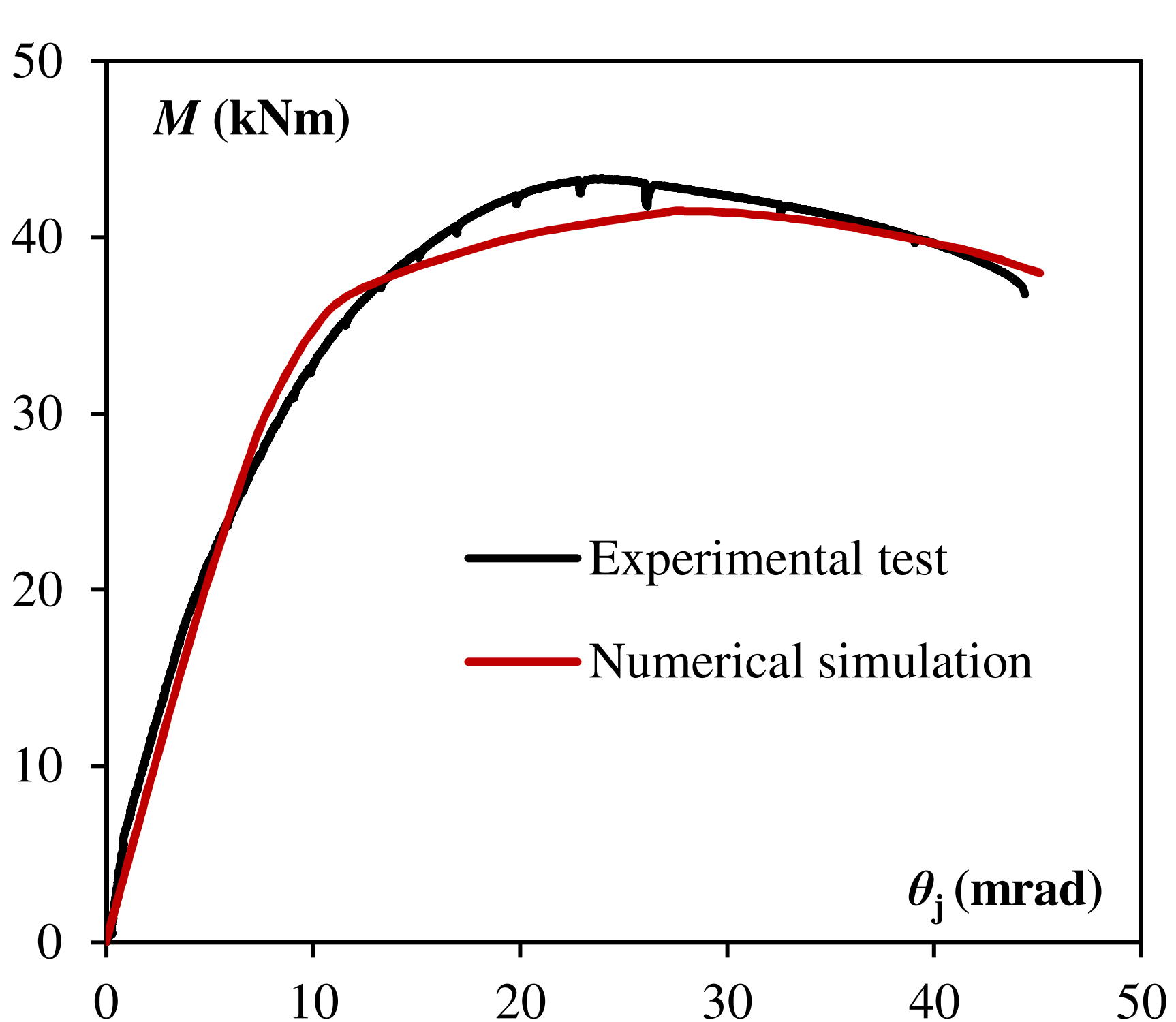
M (kNm)
50
40
30
20
10
0
Experimental test
Numerical simulation
θj (mrad)
0
10
20
30
40
50

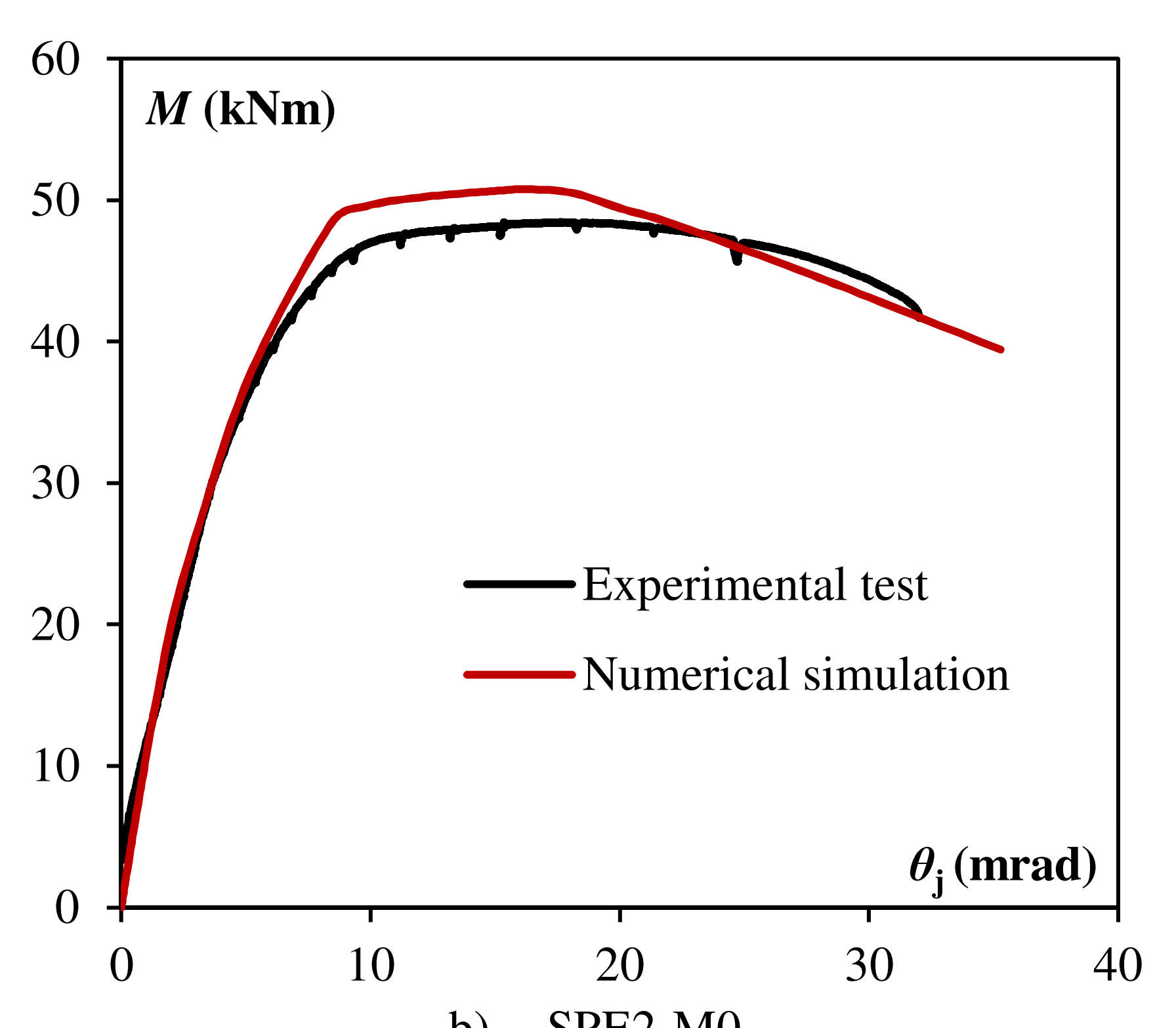
60
50
40
30
20
10
0
M (kNm)
Experimental test
Numerical simulation
θj (mrad)
0
10
20
30
40

b) SRF2-M0

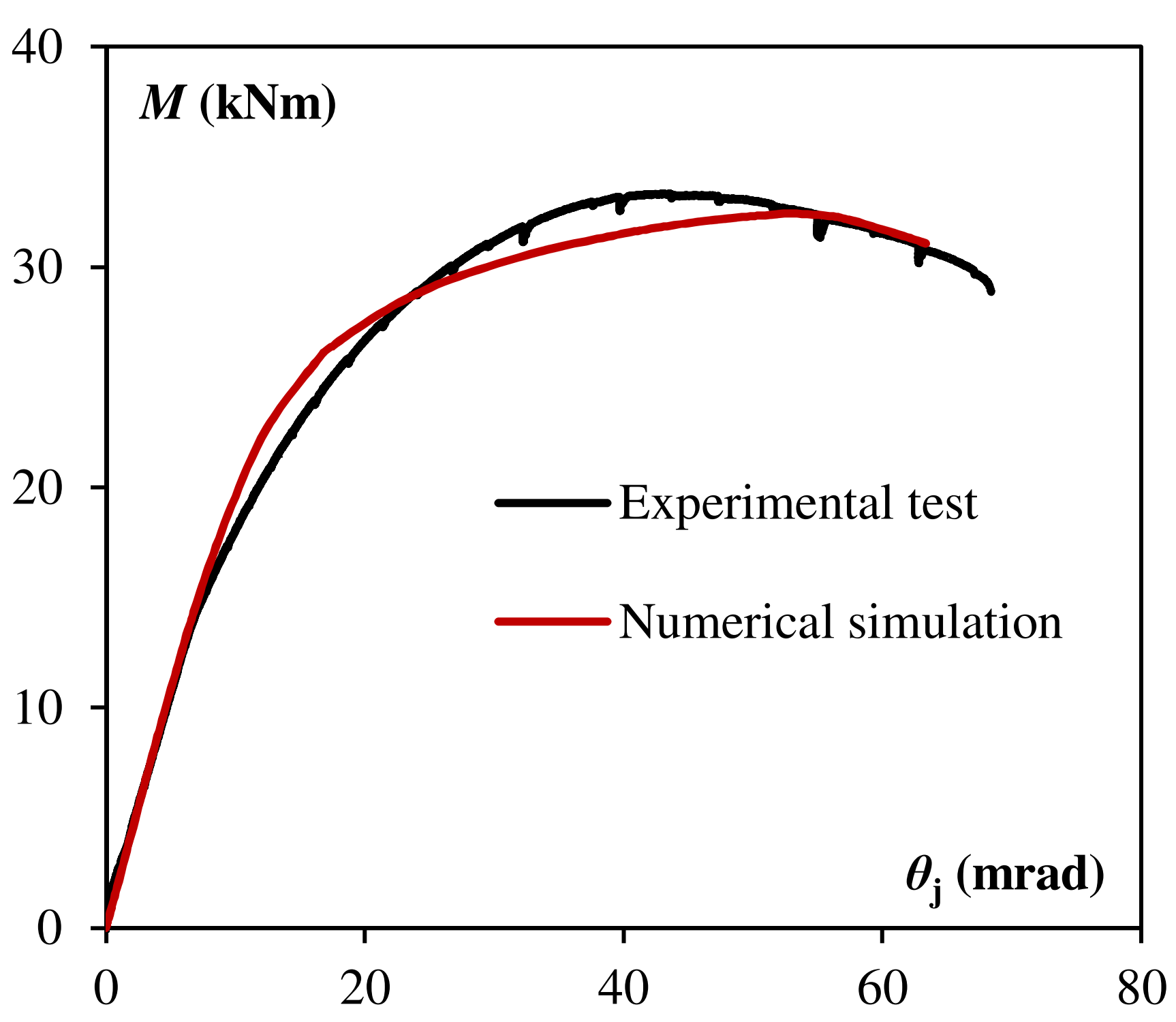
40
30
20
10
0
M (kNm)
Experimental test
Numerical simulation
θj (mrad)
0
20
40
60
80

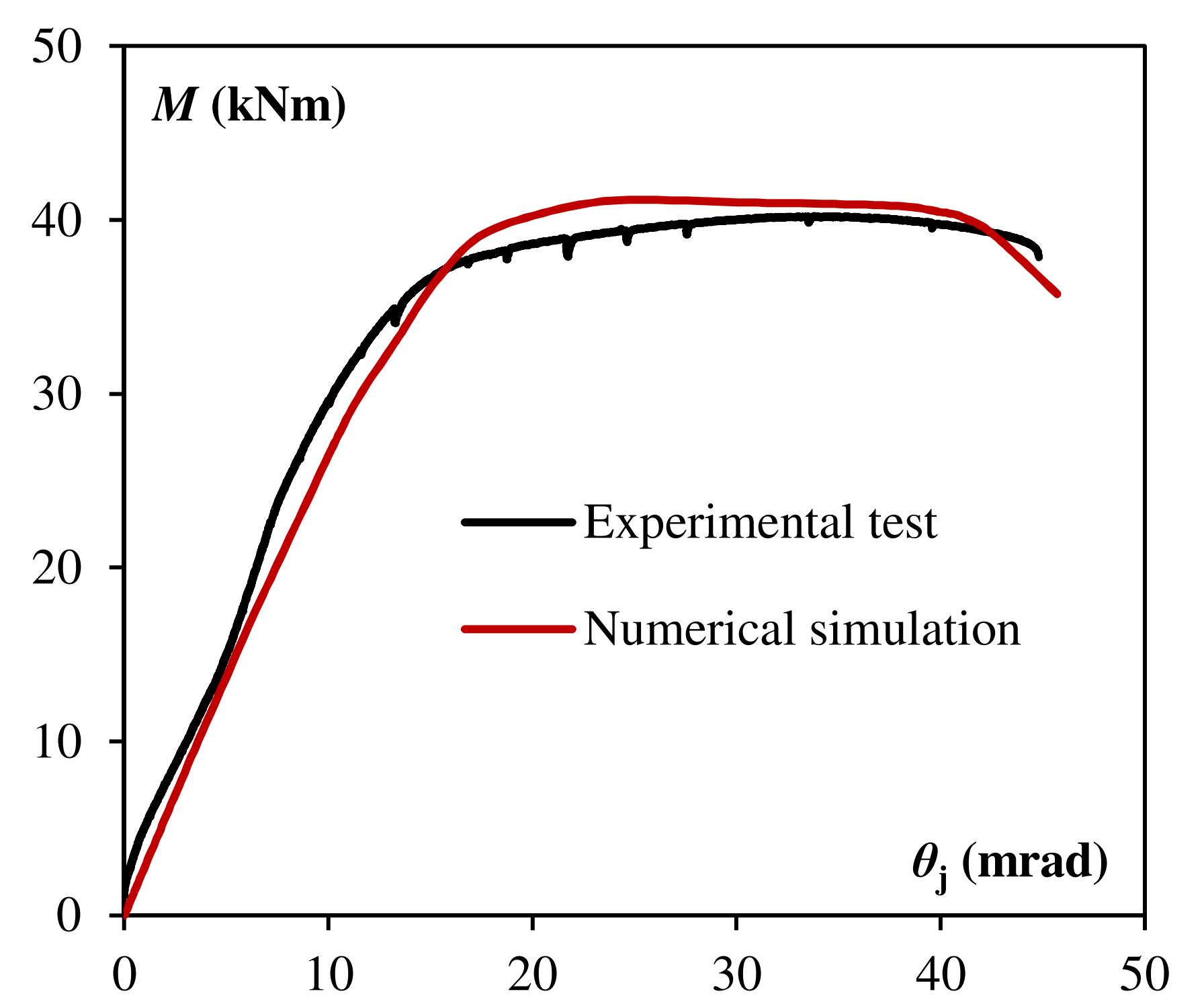
M (kNm)
50
40
30
20
10
0
Experimental test
Numerical simulation
θj (mrad)
0
10
20
30
40
50

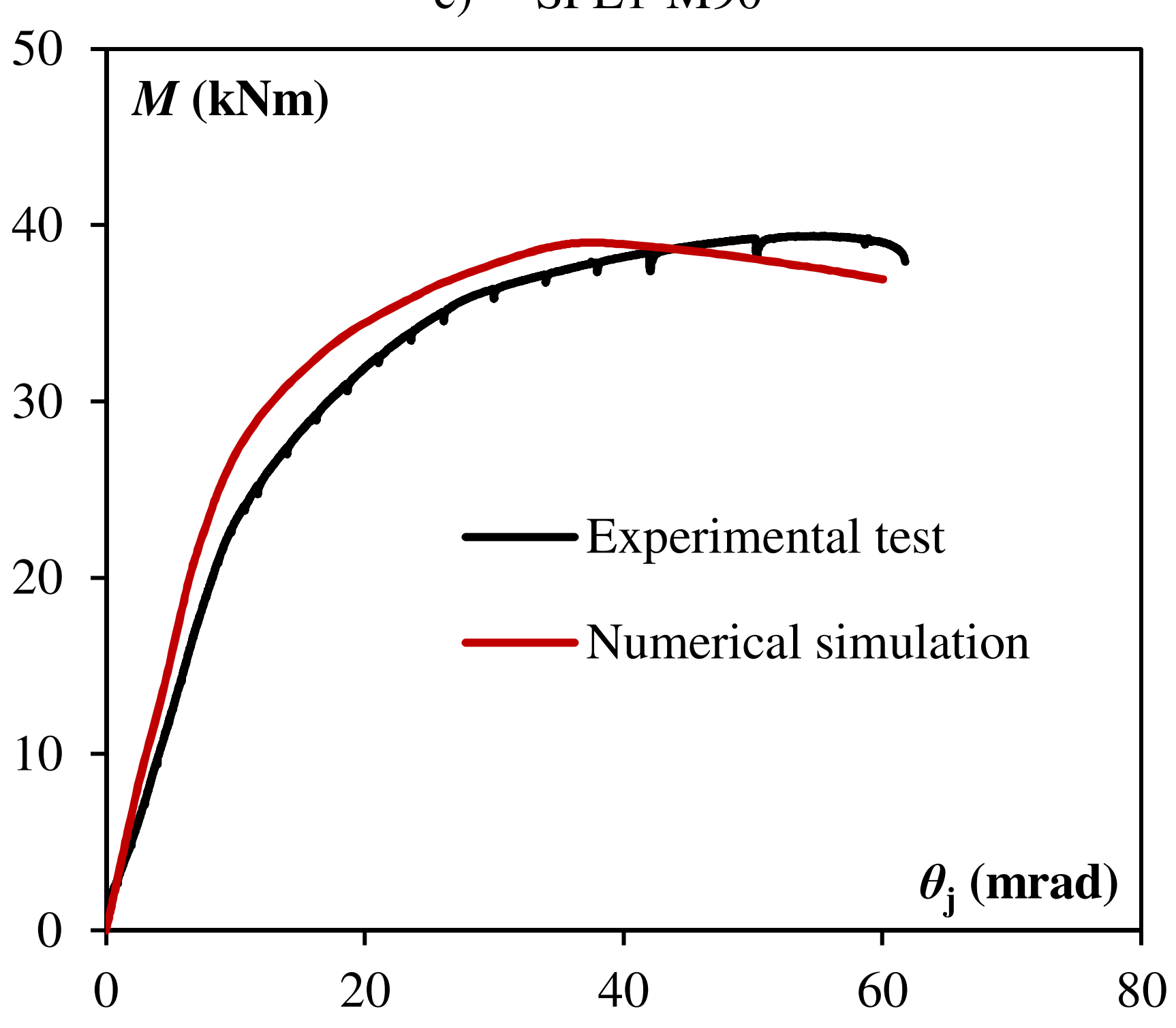
c) – SPEP-M90
M (kNm)
50
40
30
20
10
0
0
20
40
60
80
Experimental test
Numerical simulation
θj (mrad)

d) SPE2-M90

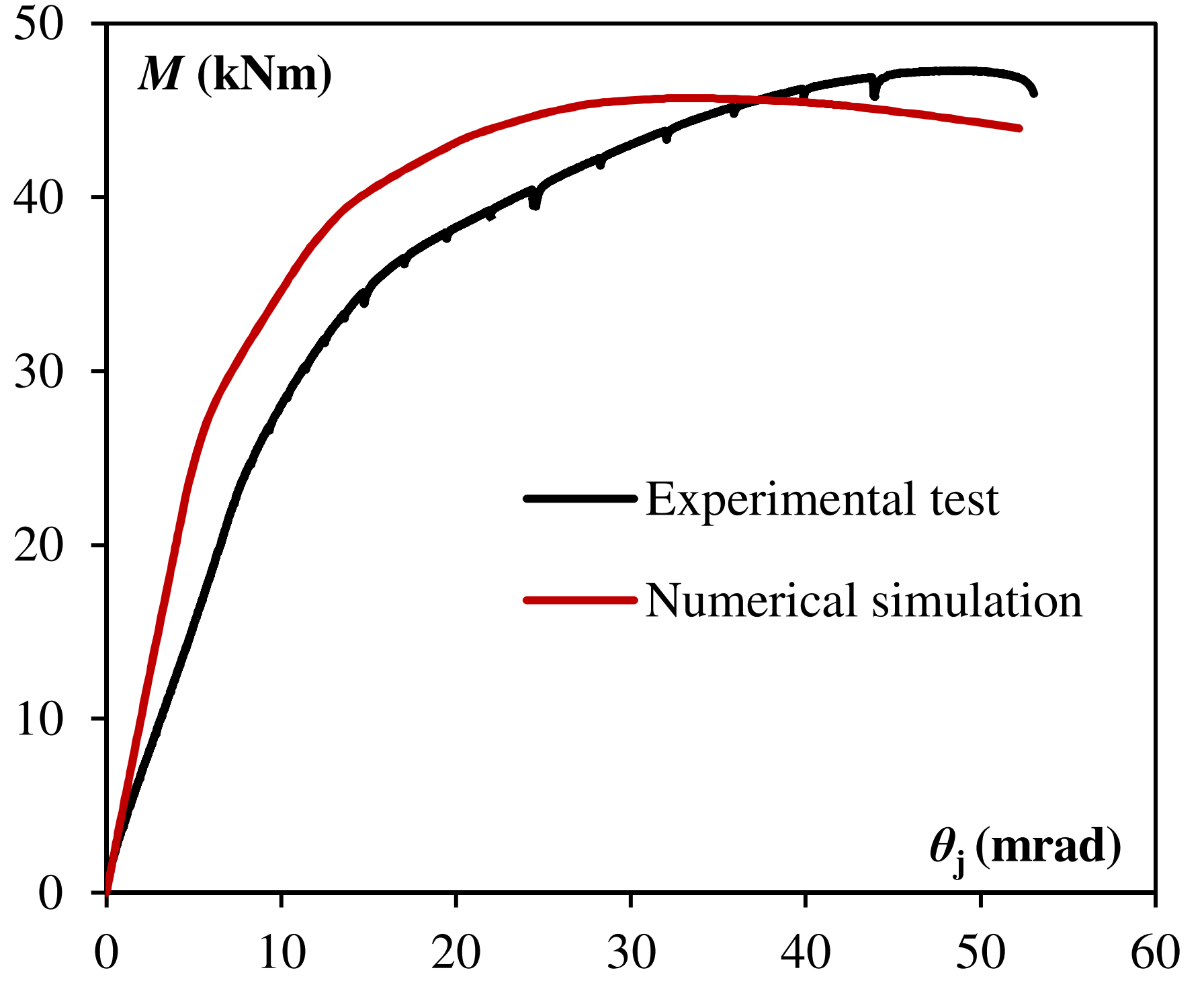
M (kNm)
50
40
30
20
10
0
0
10
20
30
40
50
60
Experimental test
Numerical simulation
θj (mrad)

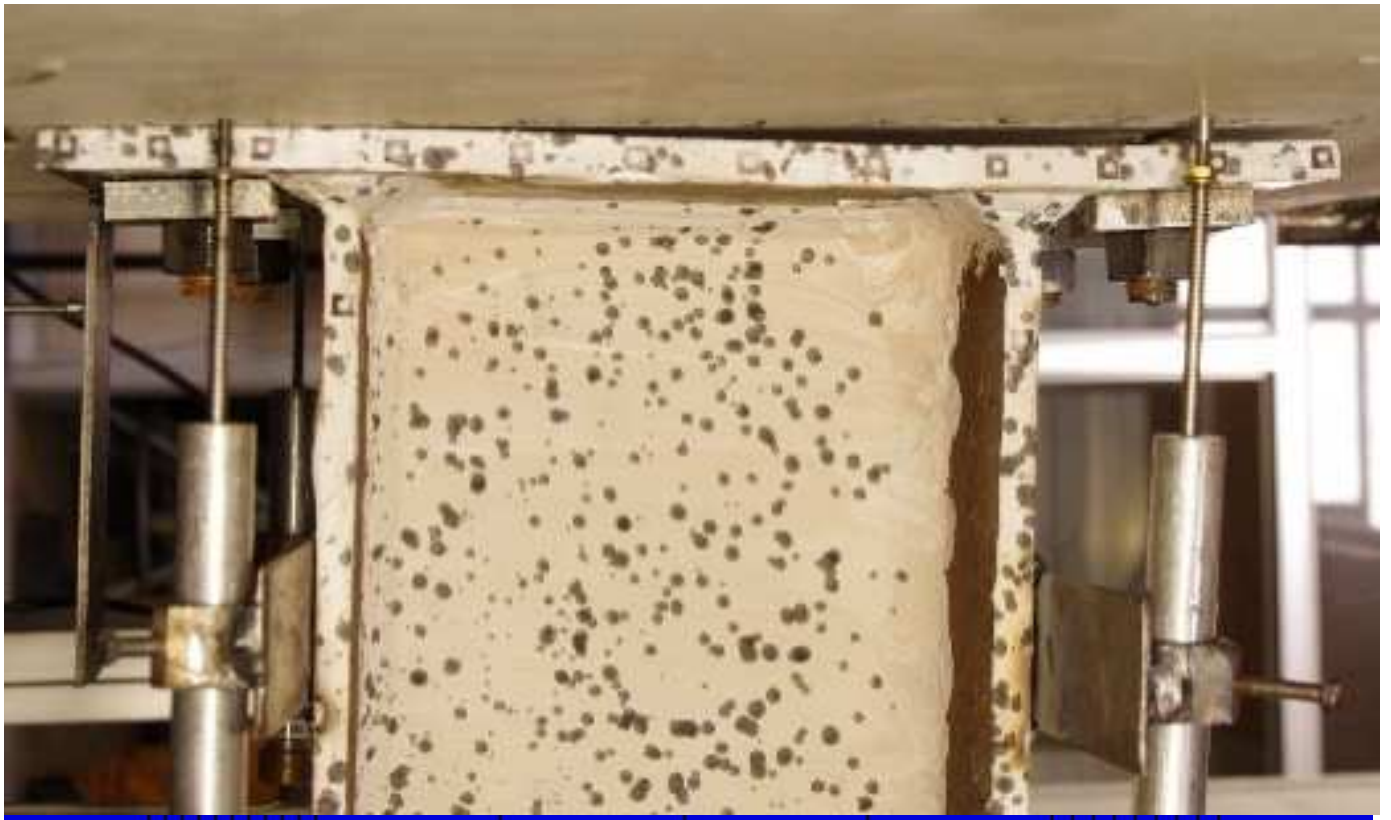

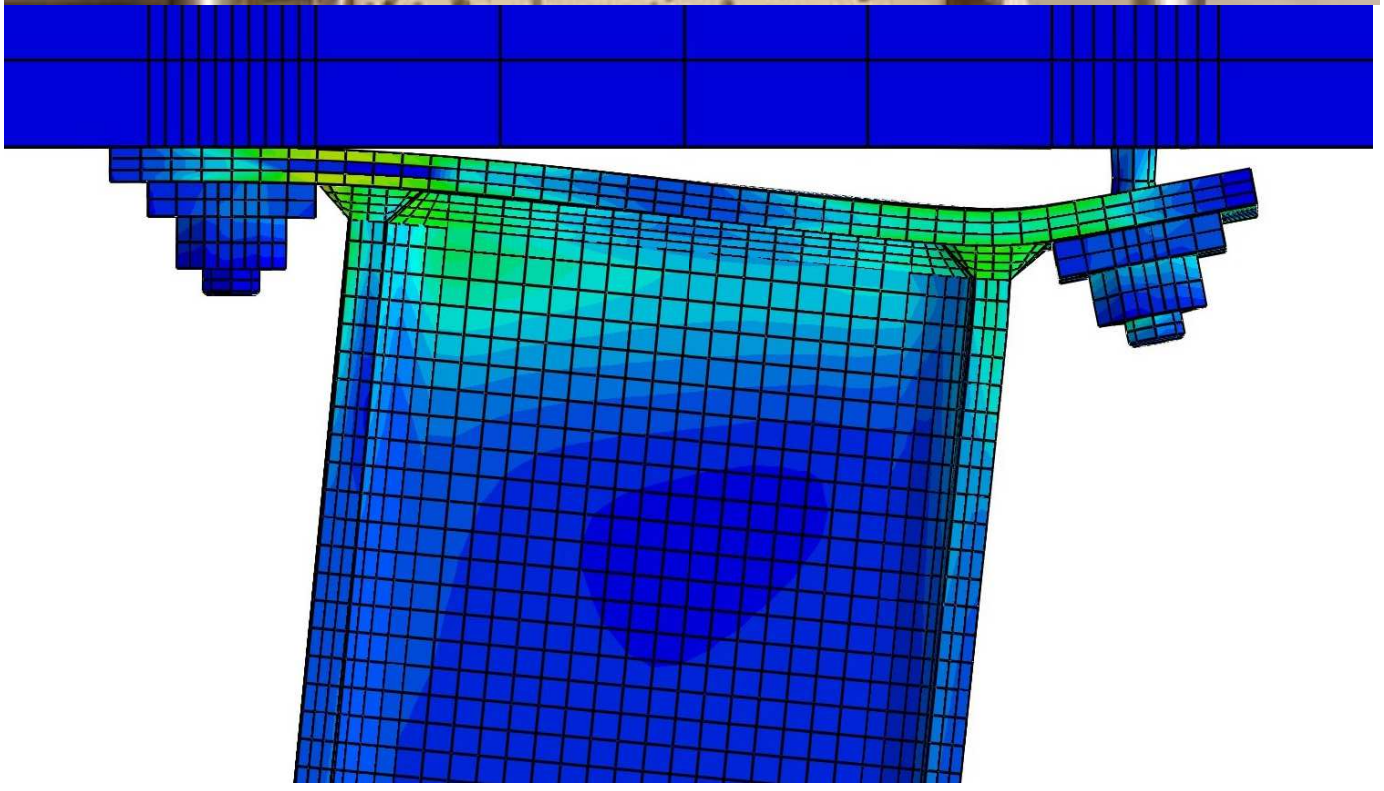

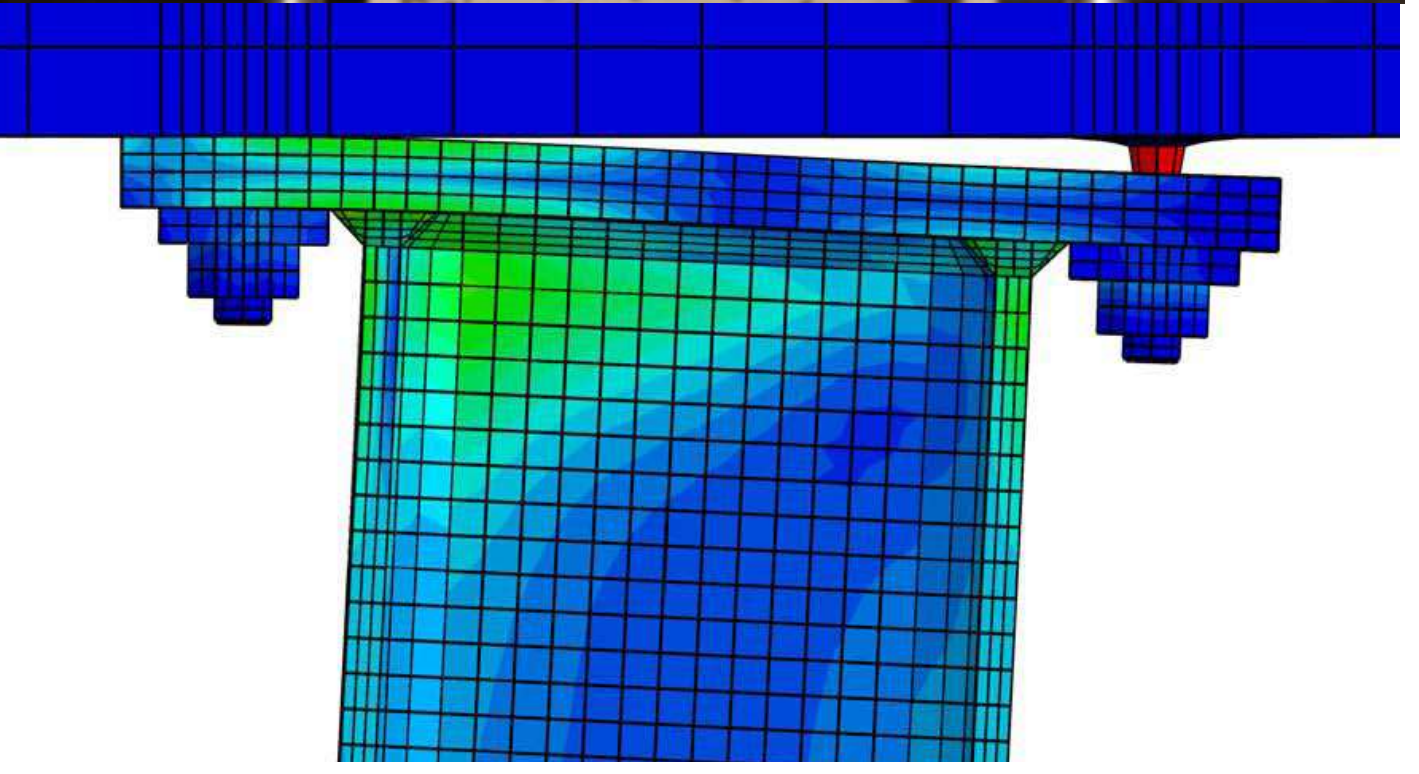

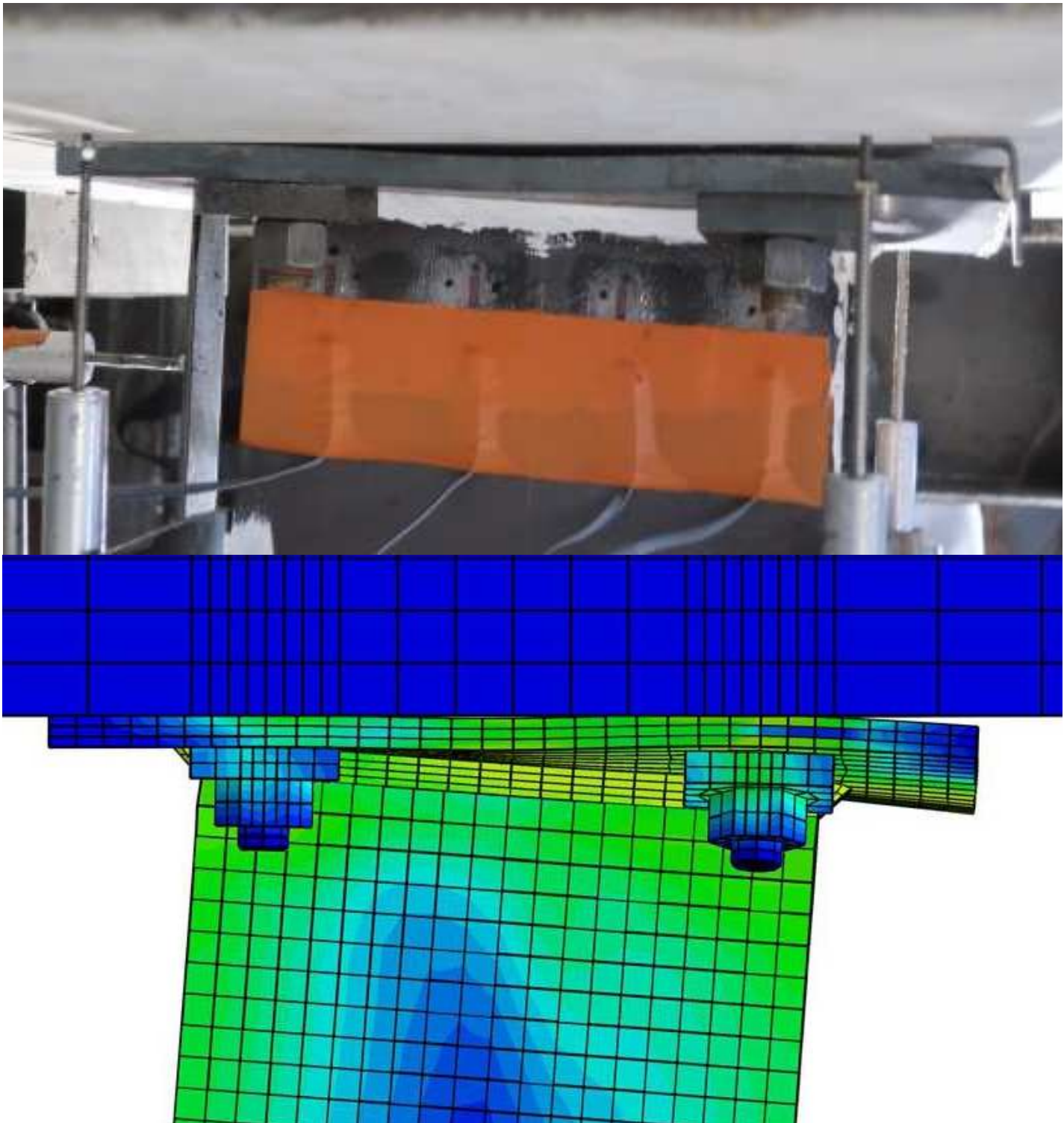


FC-S-10

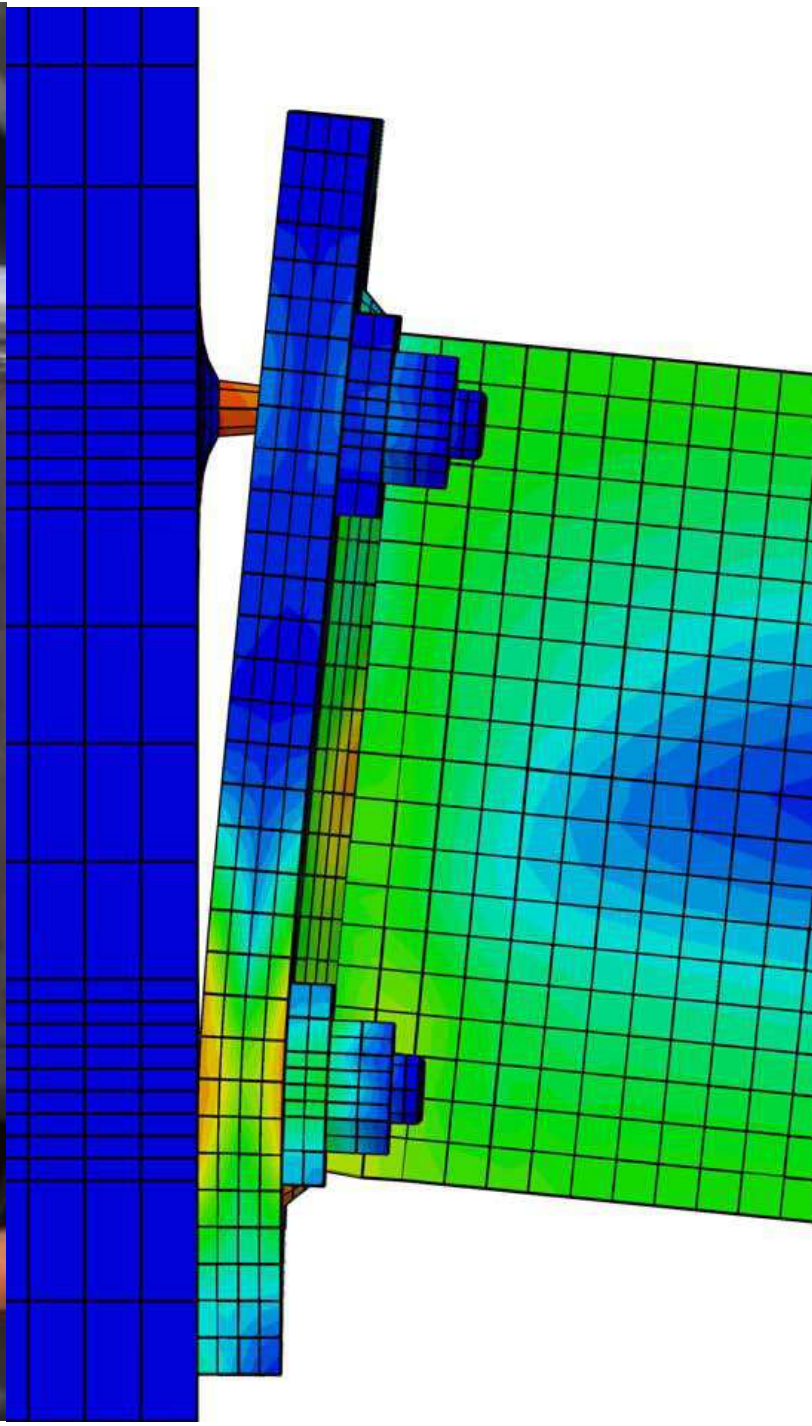

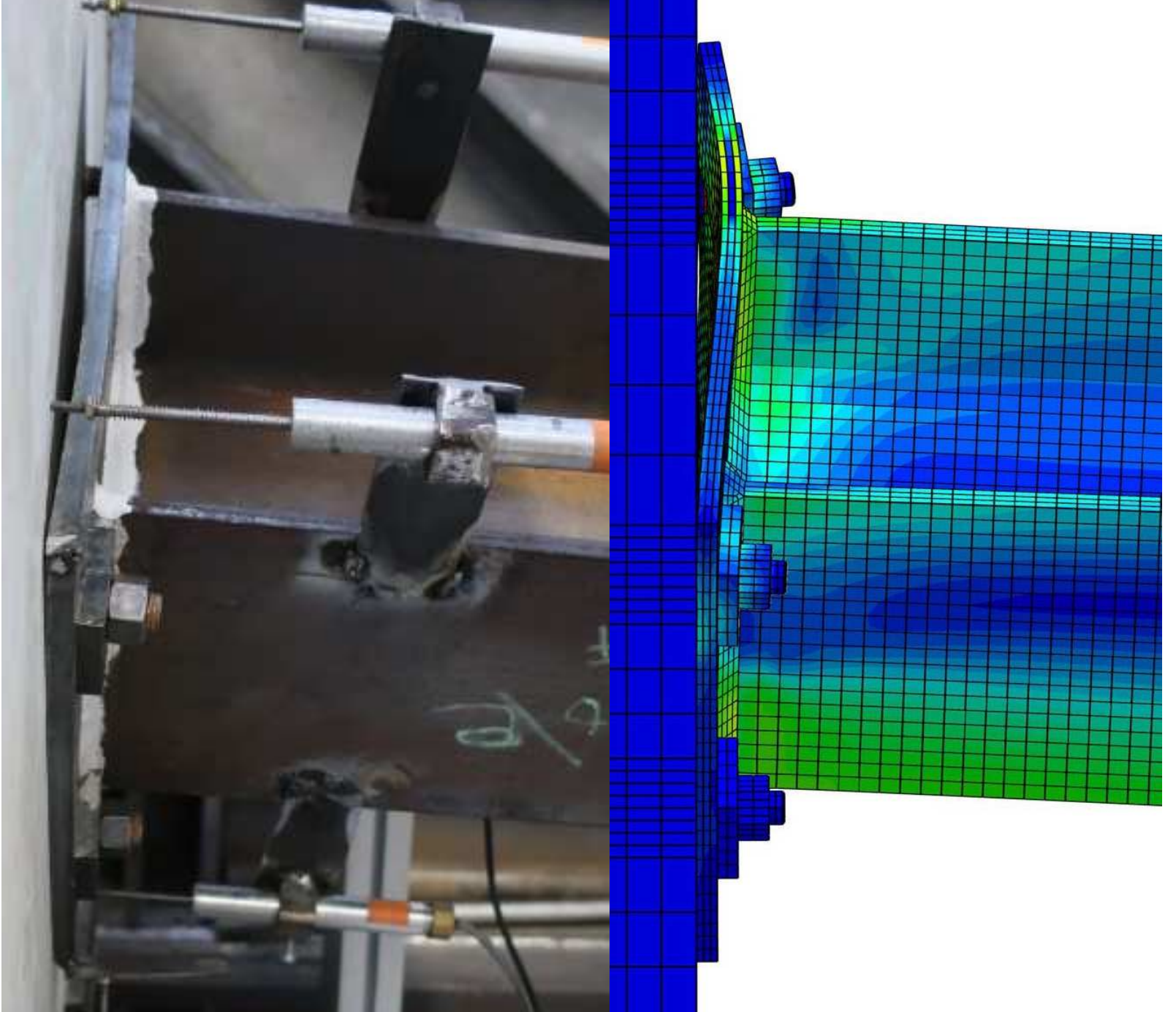

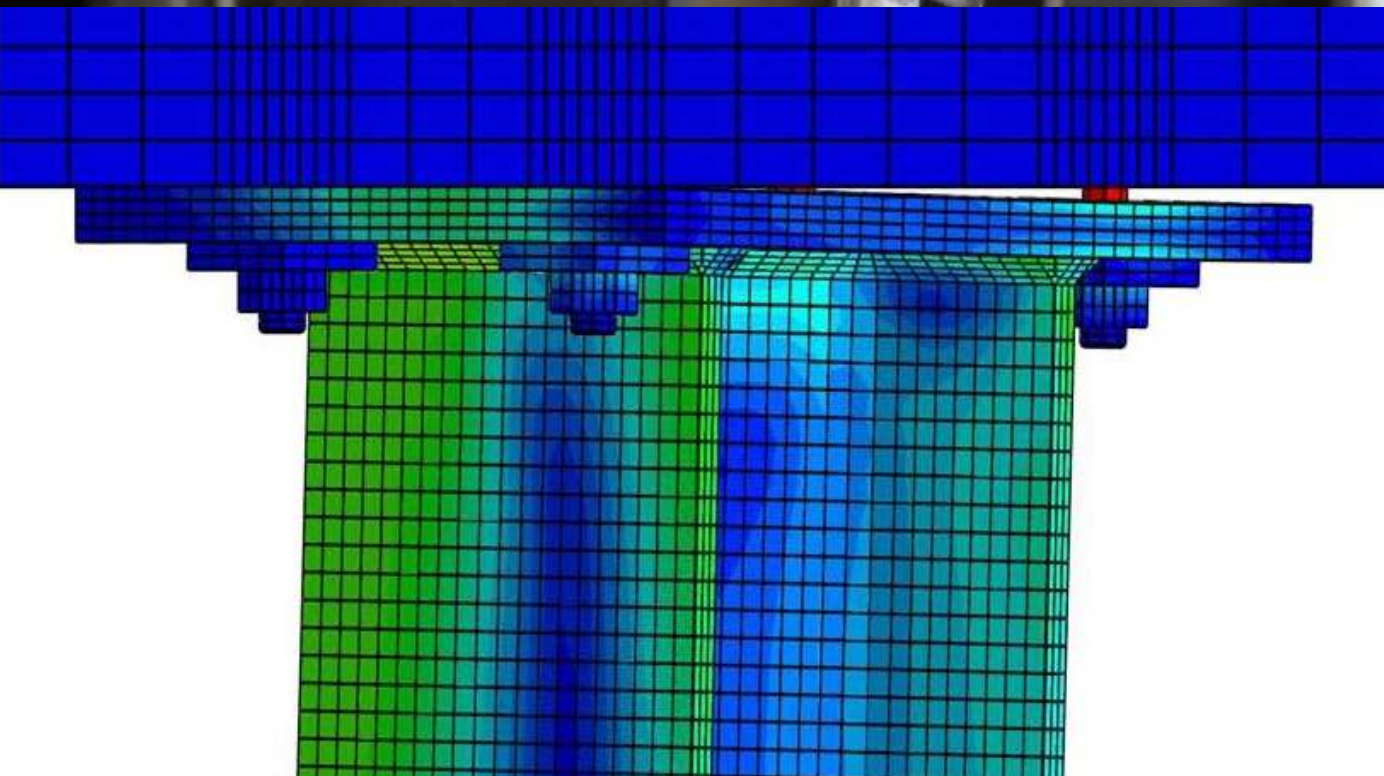

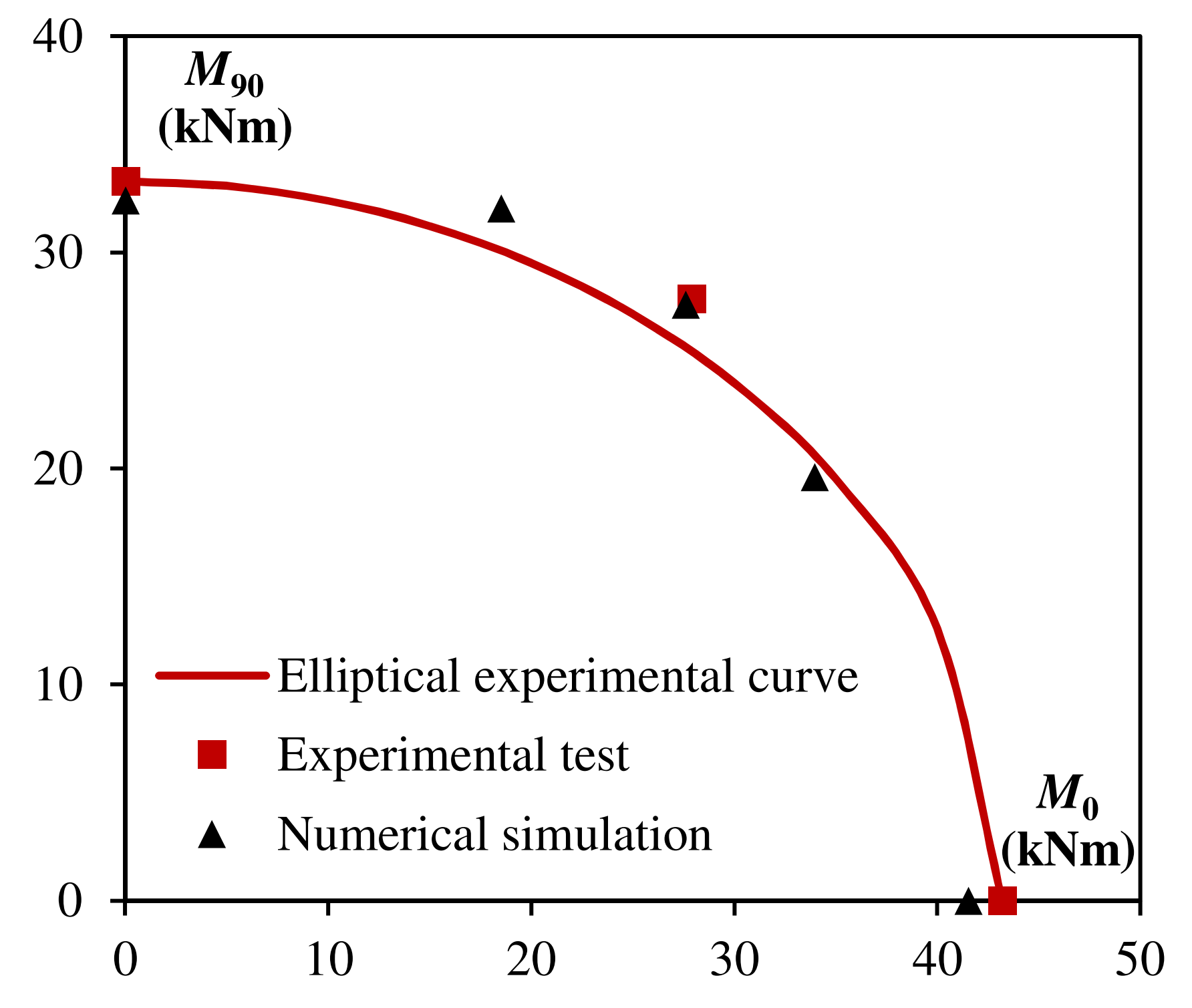
40
30
20
10
0
M_{90} (kNm)
Elliptical experimental curve
Experimental test
Numerical simulation
M_0 (kNm)
0
10
20
30
40
50

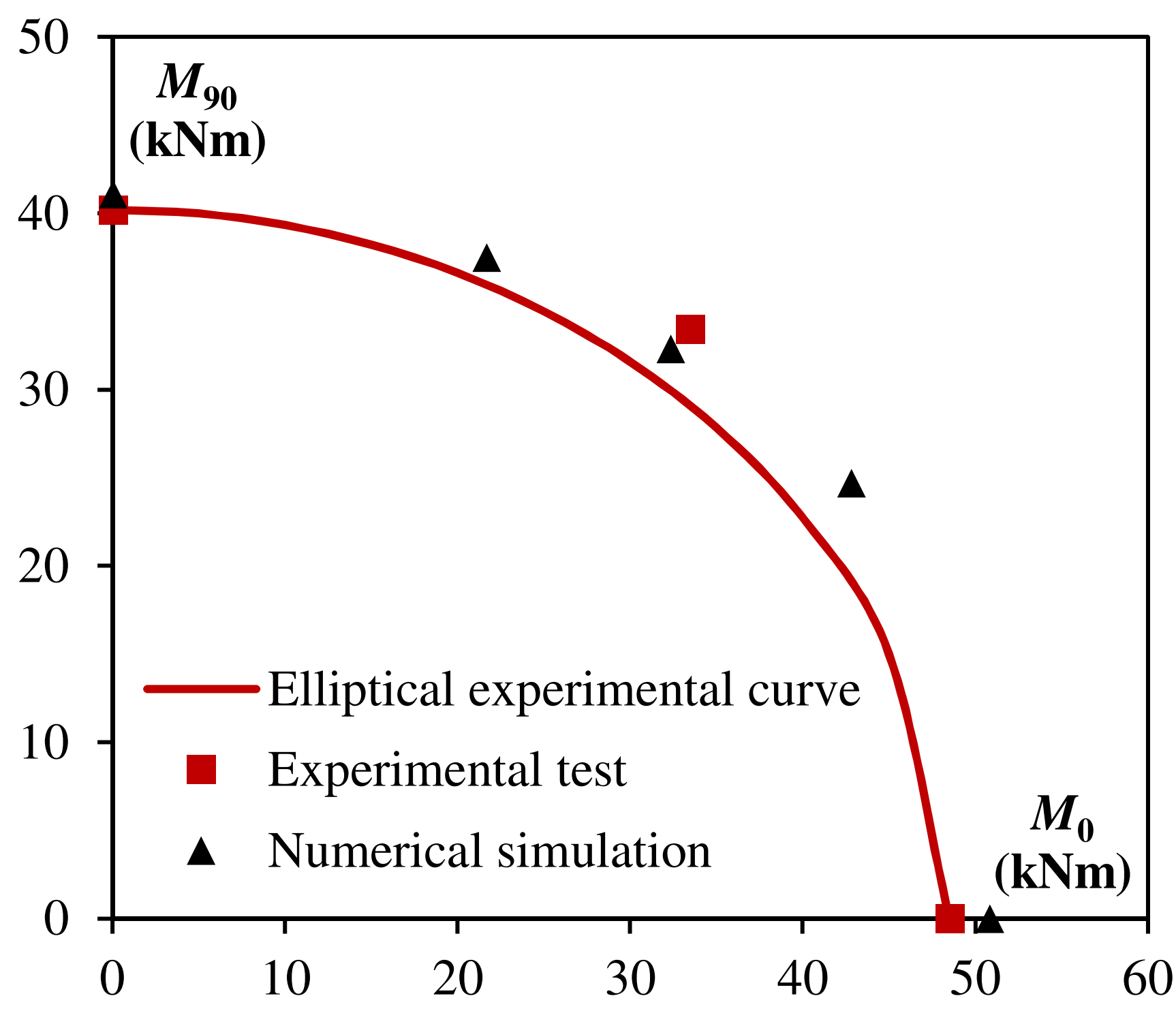
50
40
30
20
10
0
M_{90} (kNm)
Elliptical experimental curve
Experimental test
Numerical simulation
M_0 (kNm)
0
10
20
30
40
50
60

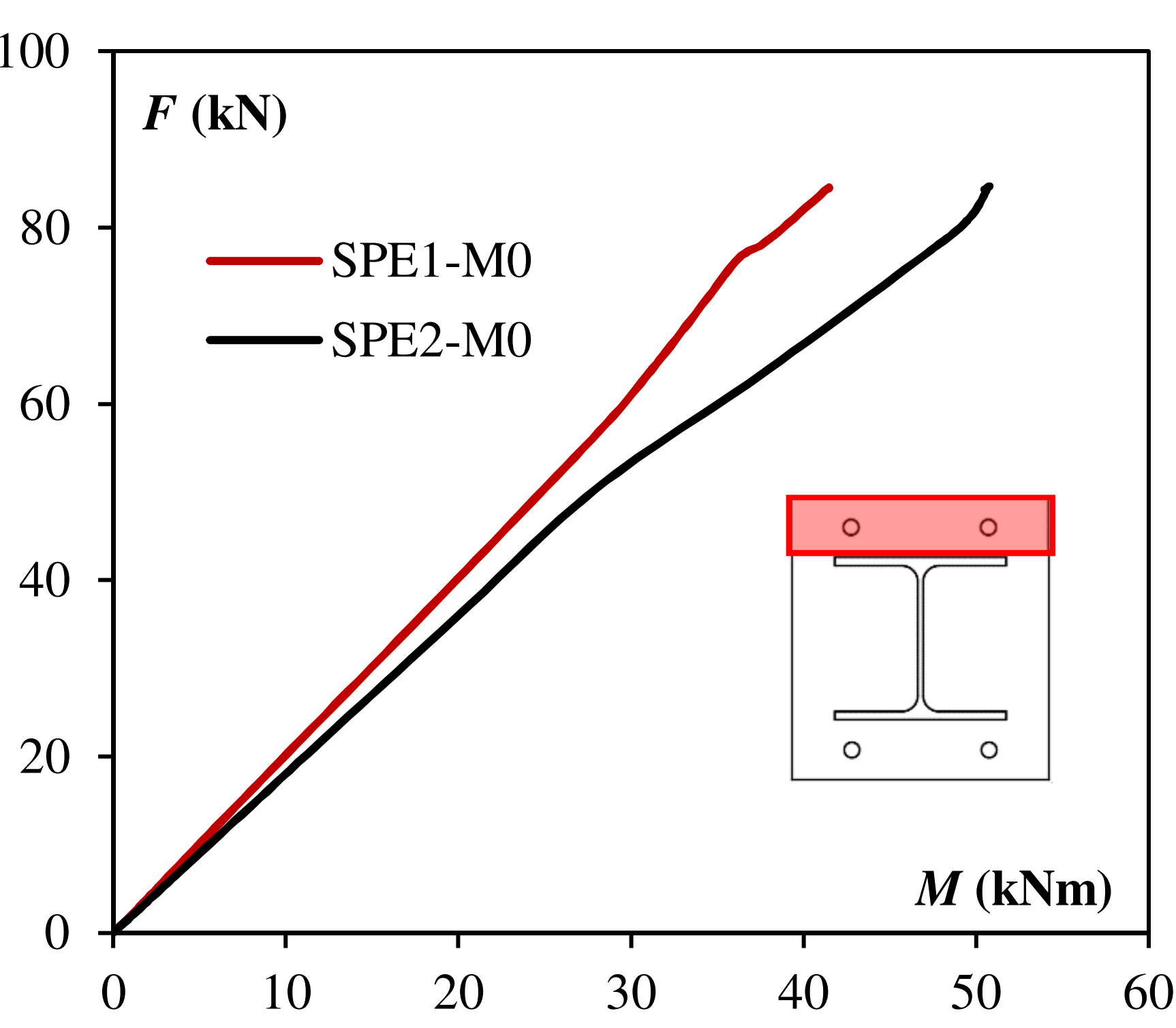
F (kN)
SPE1-M0
SPE2-M0
M (kNm)
100
80
60
40
20
0
0
10
20
30
40
50
60

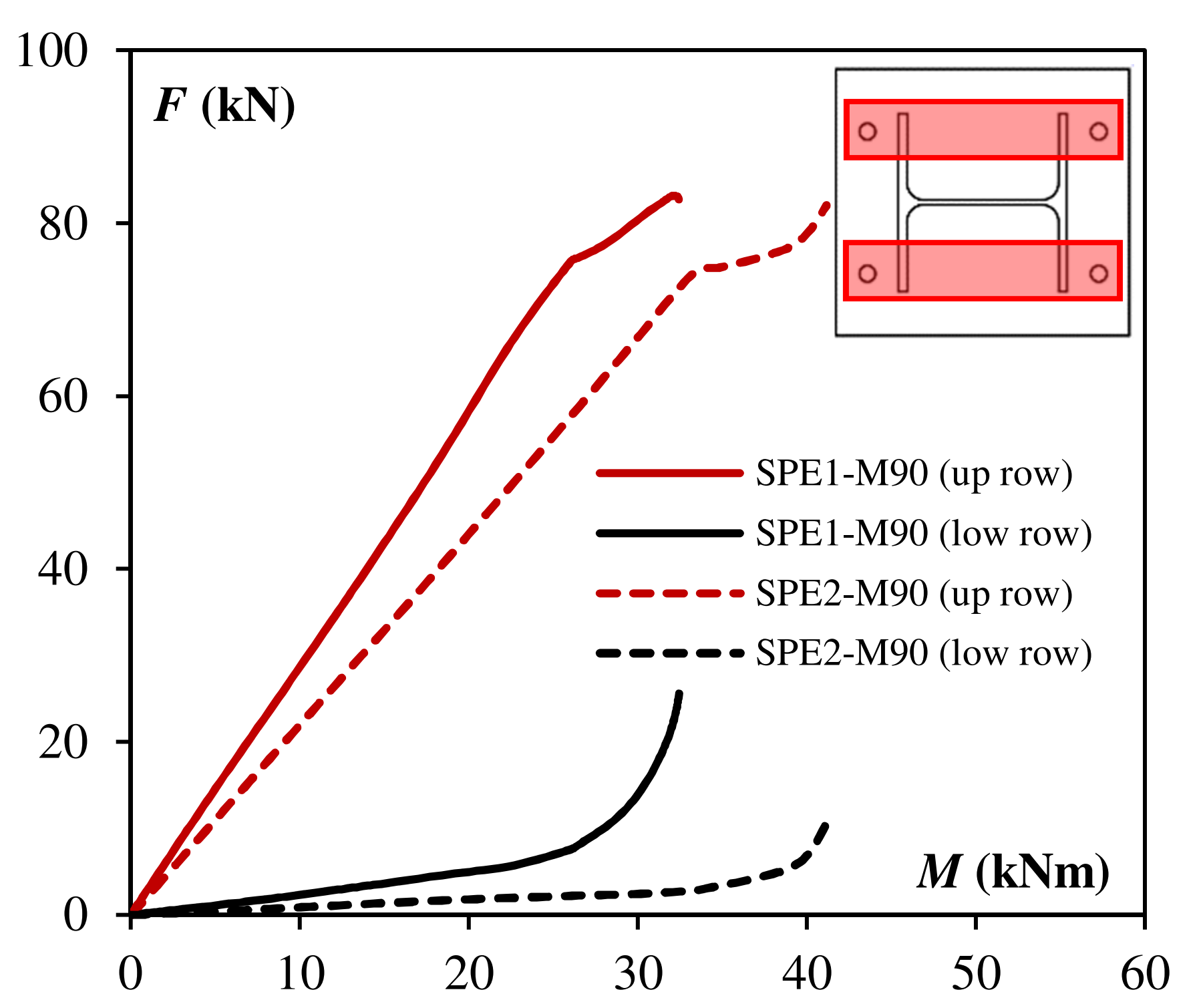
F (kN)
M (kNm)
SPE1-M90 (up row)
SPE1-M90 (low row)
SPE2-M90 (up row)
SPE2-M90 (low row)
0
20
40
60
80
100
0
10
20
30
40
50
60

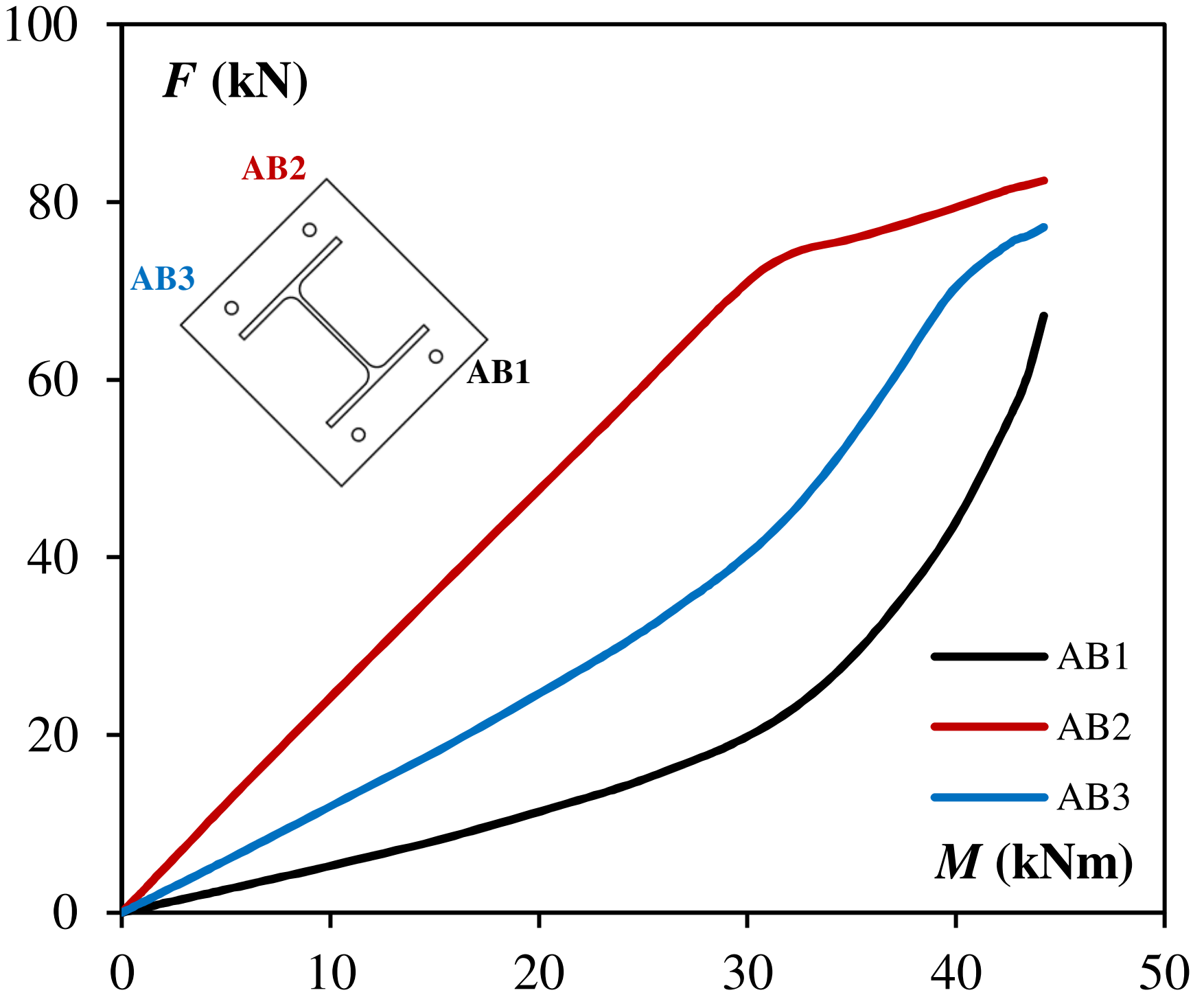
F (kN)
AB2
AB3
AB1
100
80
60
40
20
0
0
10
20
30
40
50
AB1
AB2
AB3
M (kNm)

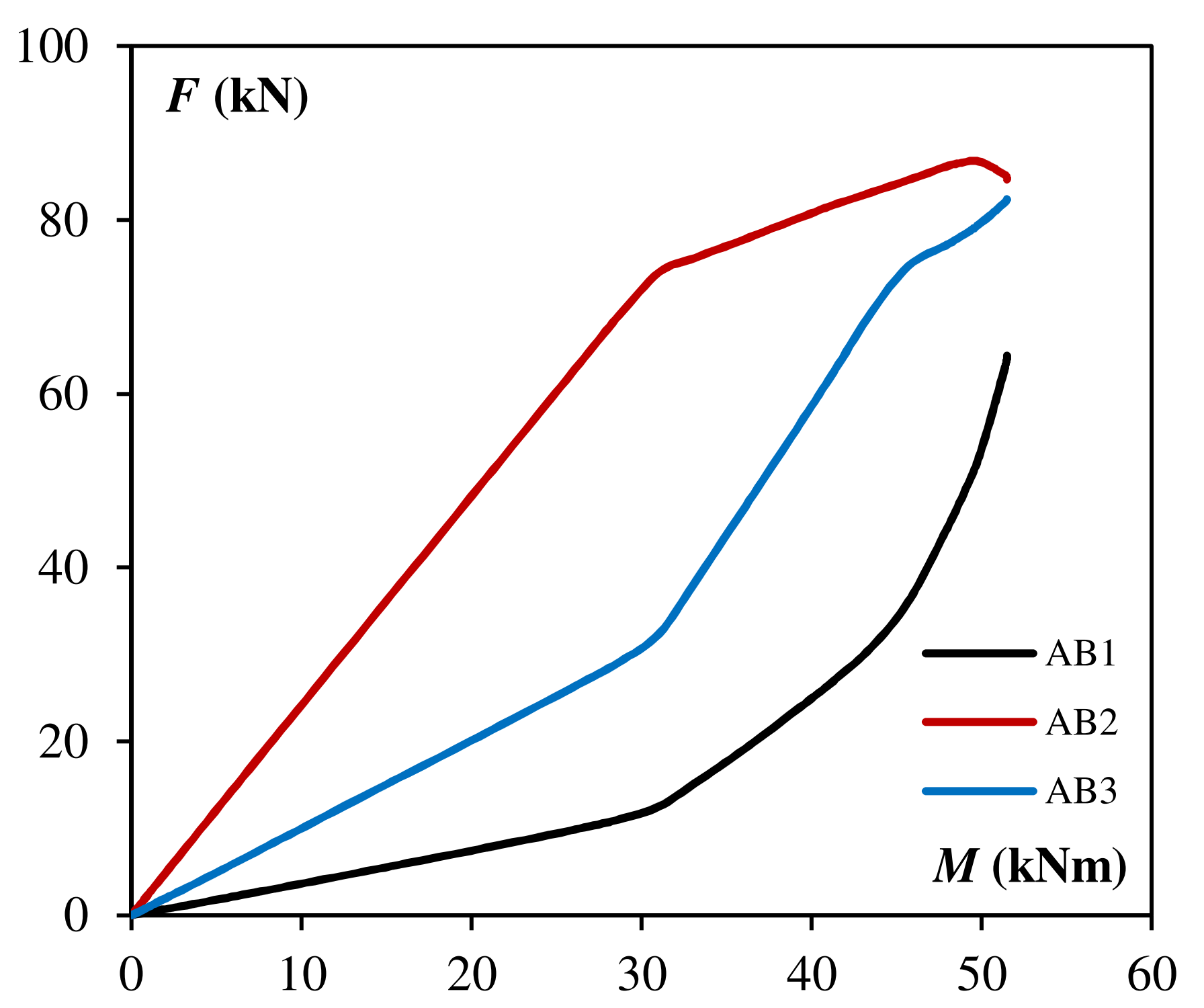
F (kN)
100
80
60
40
20
0
0
10
20
30
40
50
60
AB1
AB2
AB3
M (kNm)

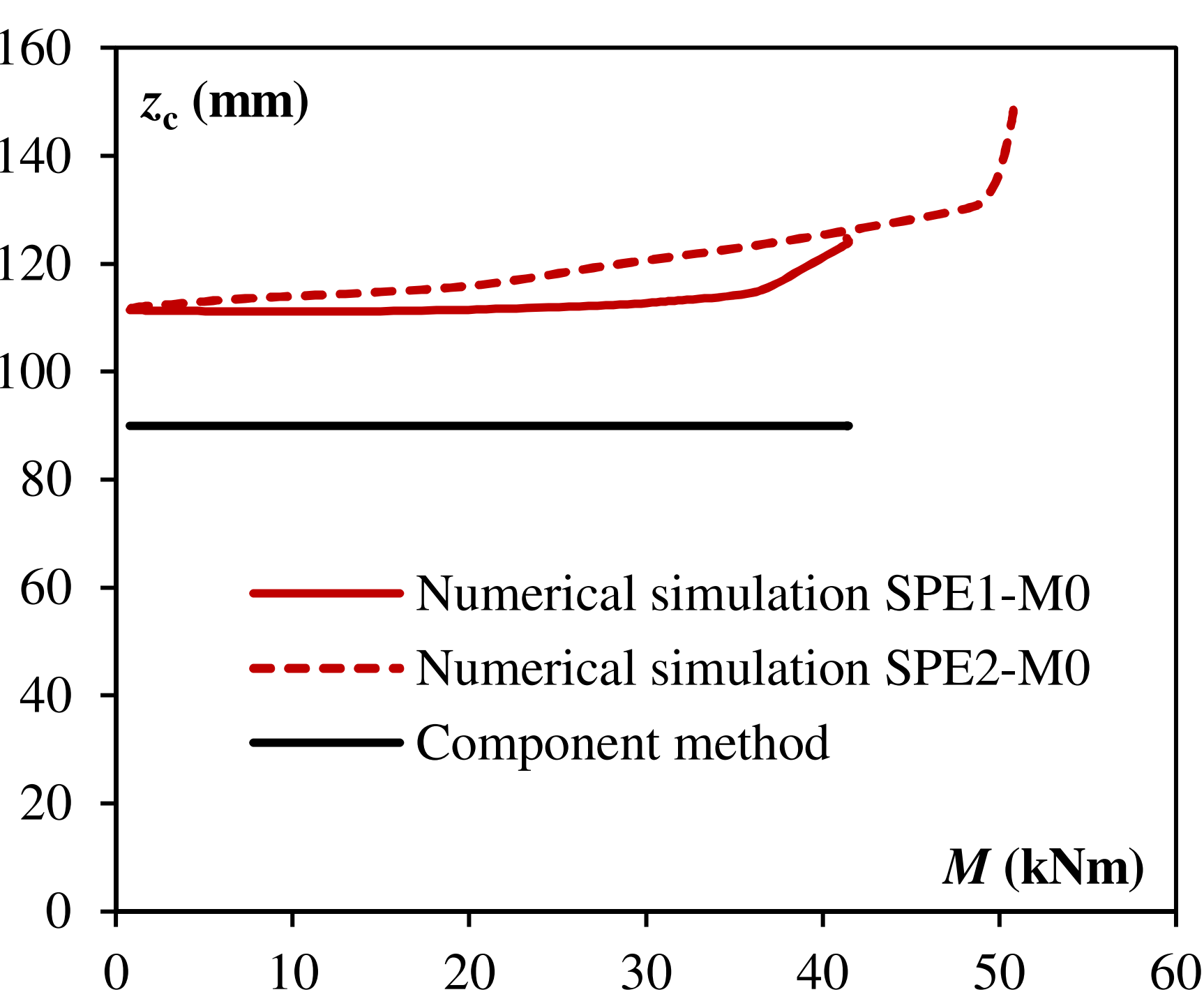
z_c (mm)
160
140
120
100
80
60
40
20
0
Numerical simulation SPE1-M0
Numerical simulation SPE2-M0
Component method
M (kNm)
0
10
20
30
40
50
60

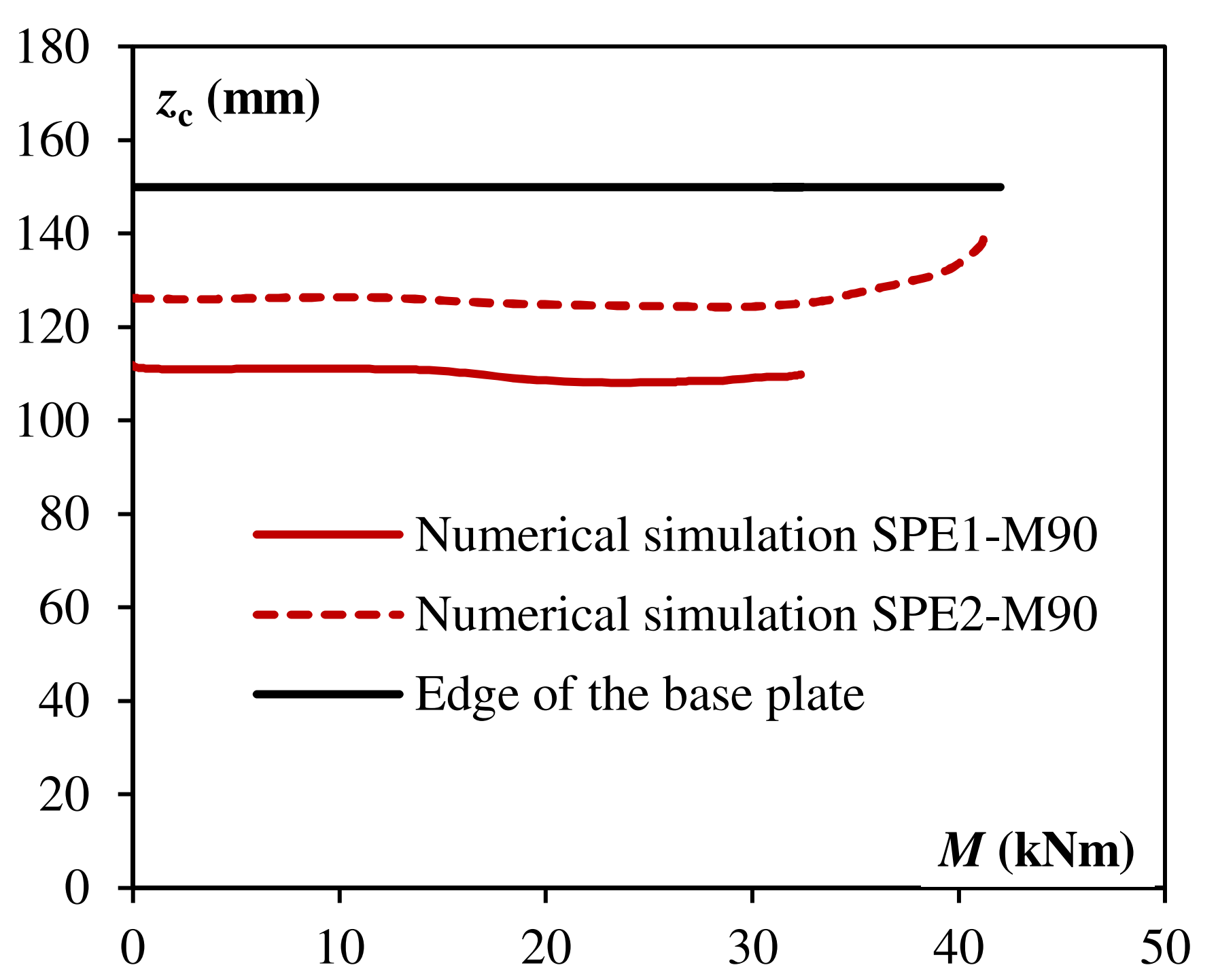
180
160
140
120
100
80
60
40
20
0
z_c (mm)
Numerical simulation SPE1-M90
Numerical simulation SPE2-M90
Edge of the base plate
M (kNm)
0
10
20
30
40
50

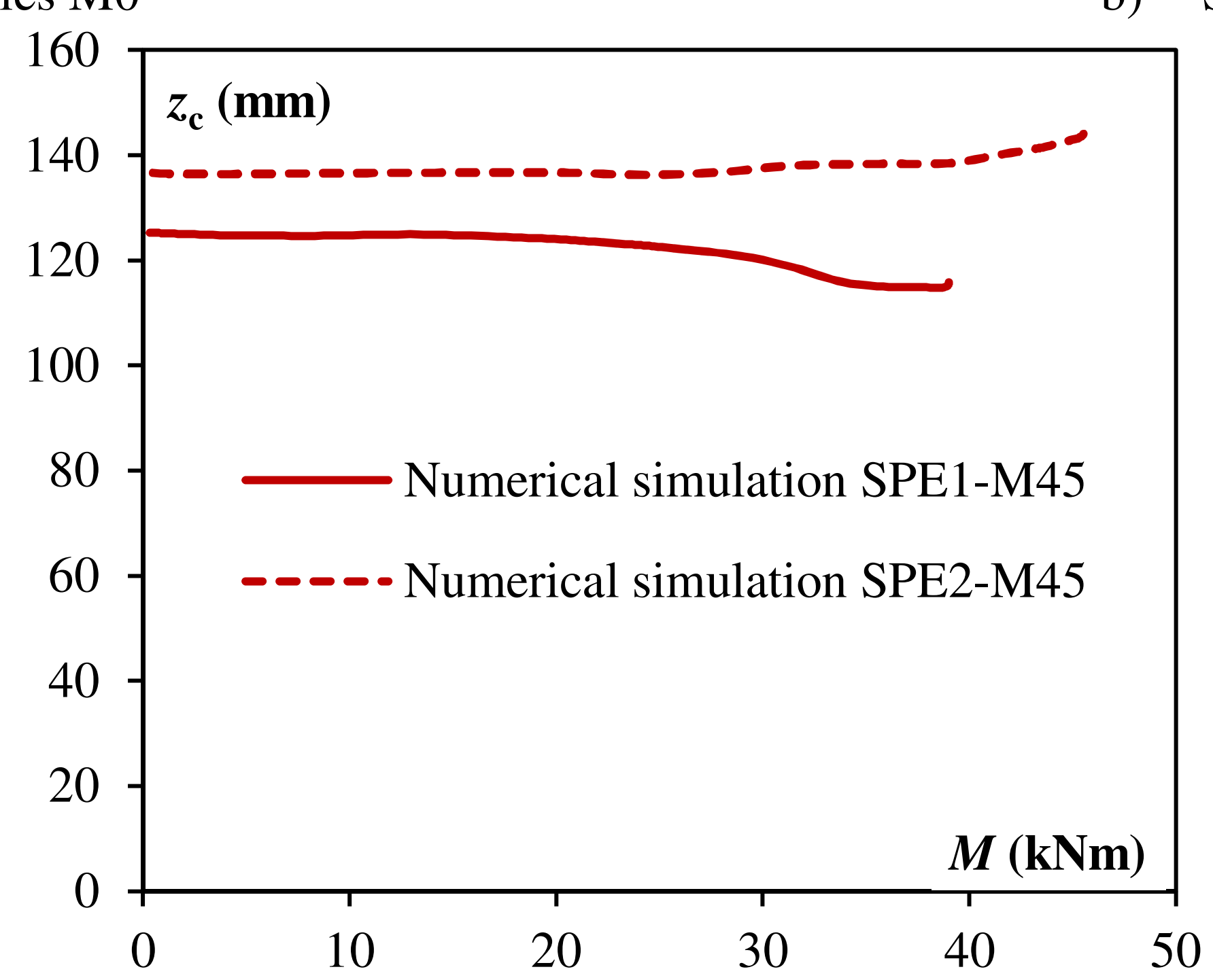
z_c (mm)
160
140
120
100
80
60
40
20
0
Numerical simulation SPE1-M45
Numerical simulation SPE2-M45
M (kNm)
0
10
20
30
40
50

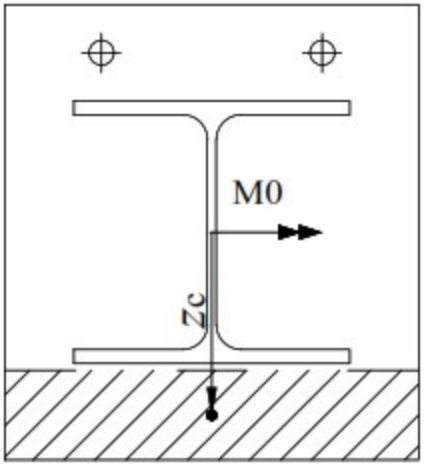
M0
Zc

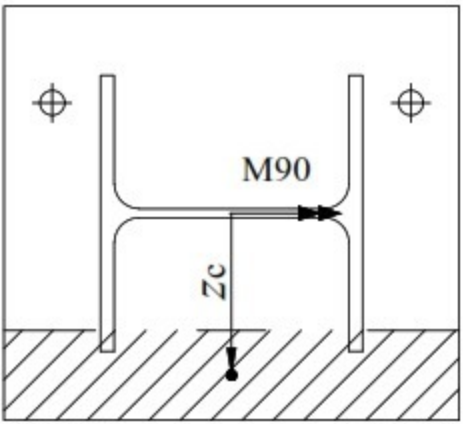
M90
Zc

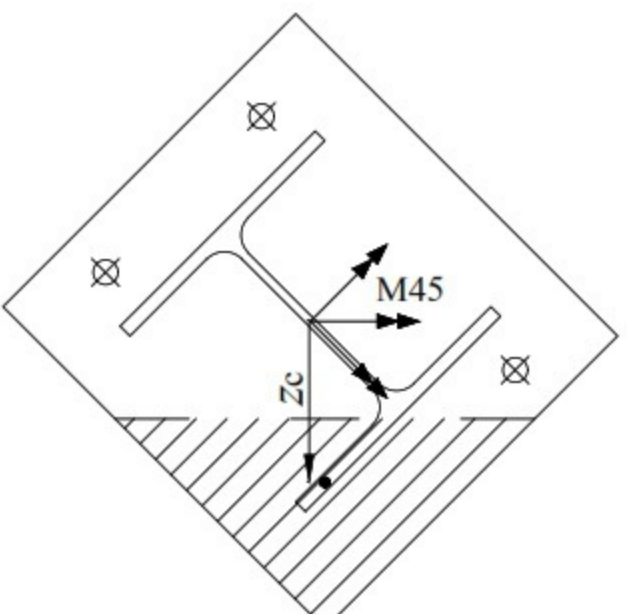
M45
Zc

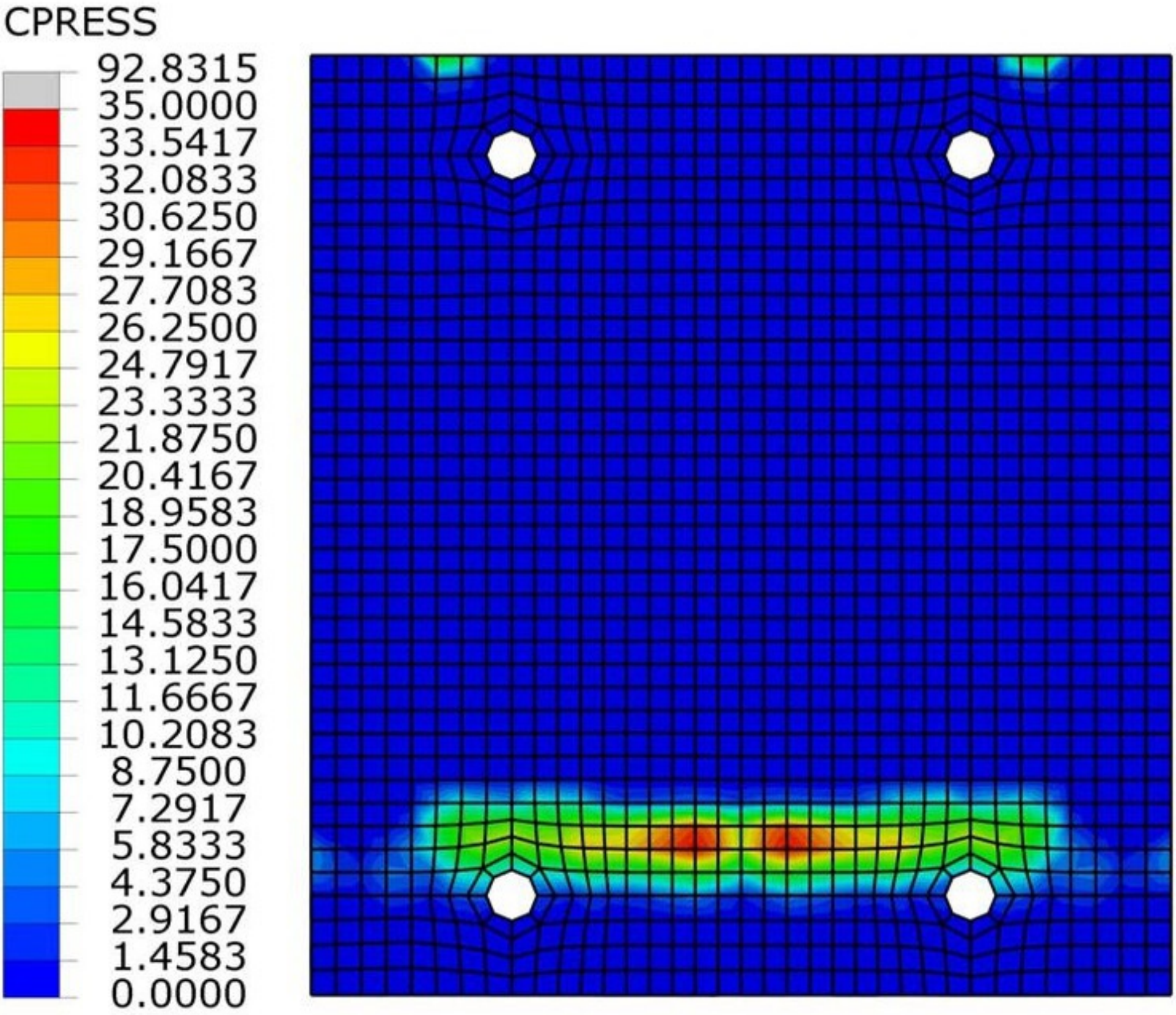
CPRESS
92.8315
35.0000
33.5417
32.0833
30.6250
29.1667
27.7083
26.2500
24.7917
23.3333
21.8750
20.4167
18.9583
17.5000
16.0417
14.5833
13.1250
11.6667
10.2083
8.7500
7.2917
5.8333
4.3750
2.9167
1.4583
0.0000

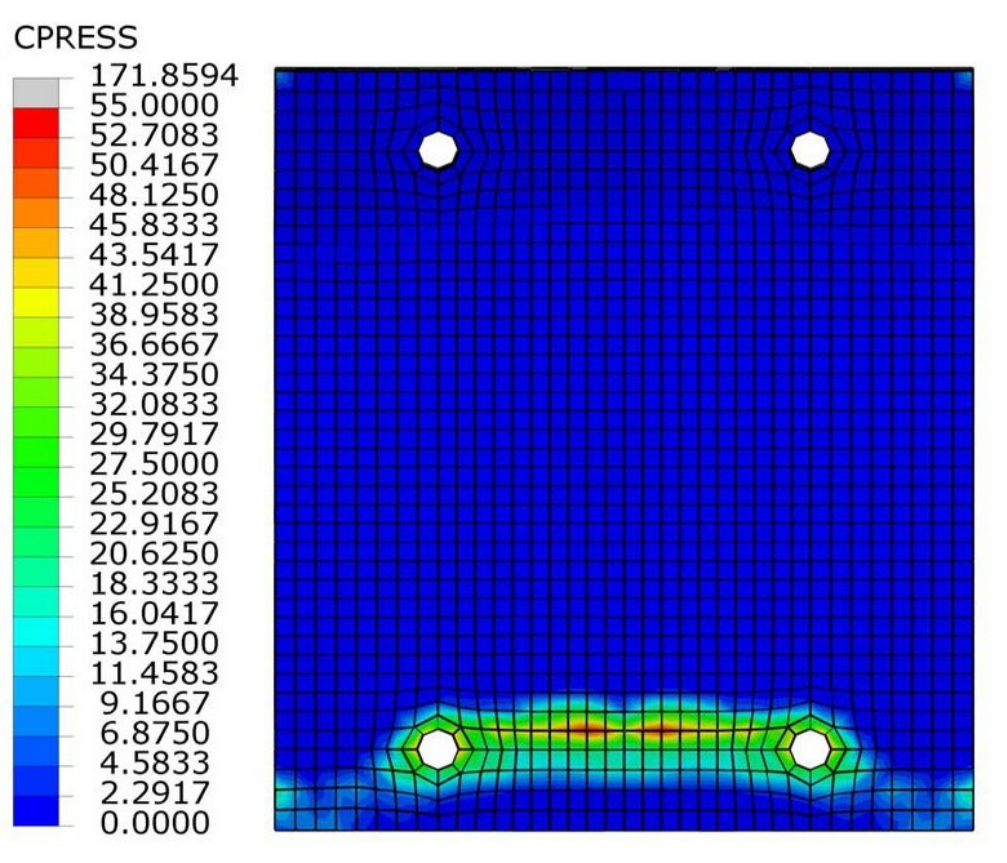
CPRESS
171.8594
55.0000
52.7083
50.4167
48.1250
45.8333
43.5417
41.2500
38.9583
36.6667
34.3750
32.0833
29.7917
27.5000
25.2083
22.9167
20.6250
18.3333
16.0417
13.7500
11.4583
9.1667
6.8750
4.5833
2.2917
0.0000

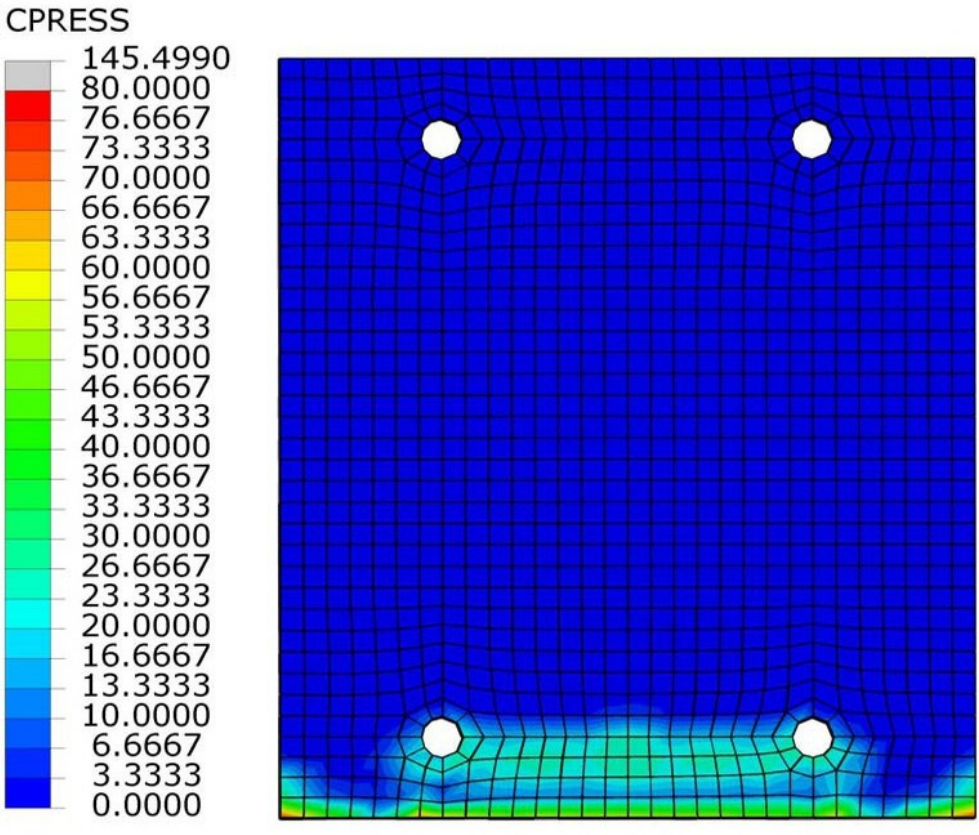
CPRESS
145.4990
80.0000
76.6667
73.3333
70.0000
66.6667
63.3333
60.0000
56.6667
53.3333
50.0000
46.6667
43.3333
40.0000
36.6667
33.3333
30.0000
26.6667
23.3333
20.0000
16.6667
13.3333
10.0000
6.6667
3.3333
0.0000

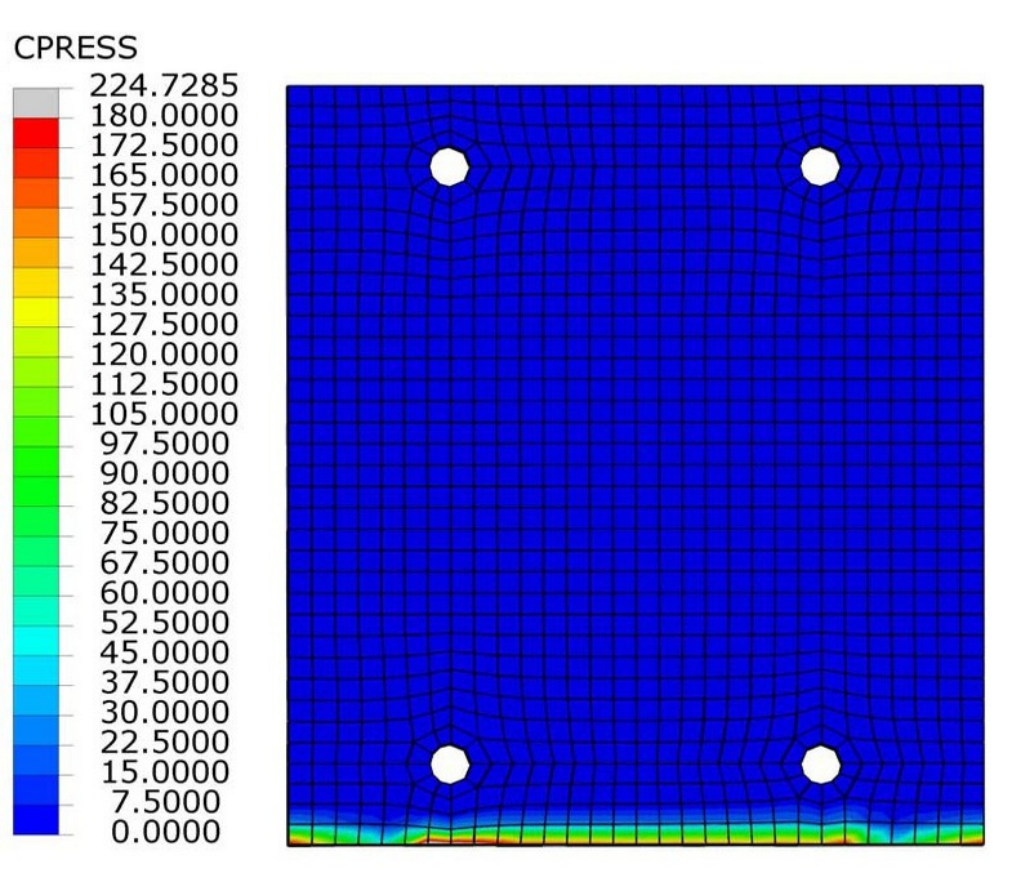
CPRESS
224.7285
180.0000
172.5000
165.0000
157.5000
150.0000
142.5000
135.0000
127.5000
120.0000
112.5000
105.0000
97.5000
90.0000
82.5000
75.0000
67.5000
60.0000
52.5000
45.0000
37.5000
30.0000
22.5000
15.0000
7.5000
0.0000

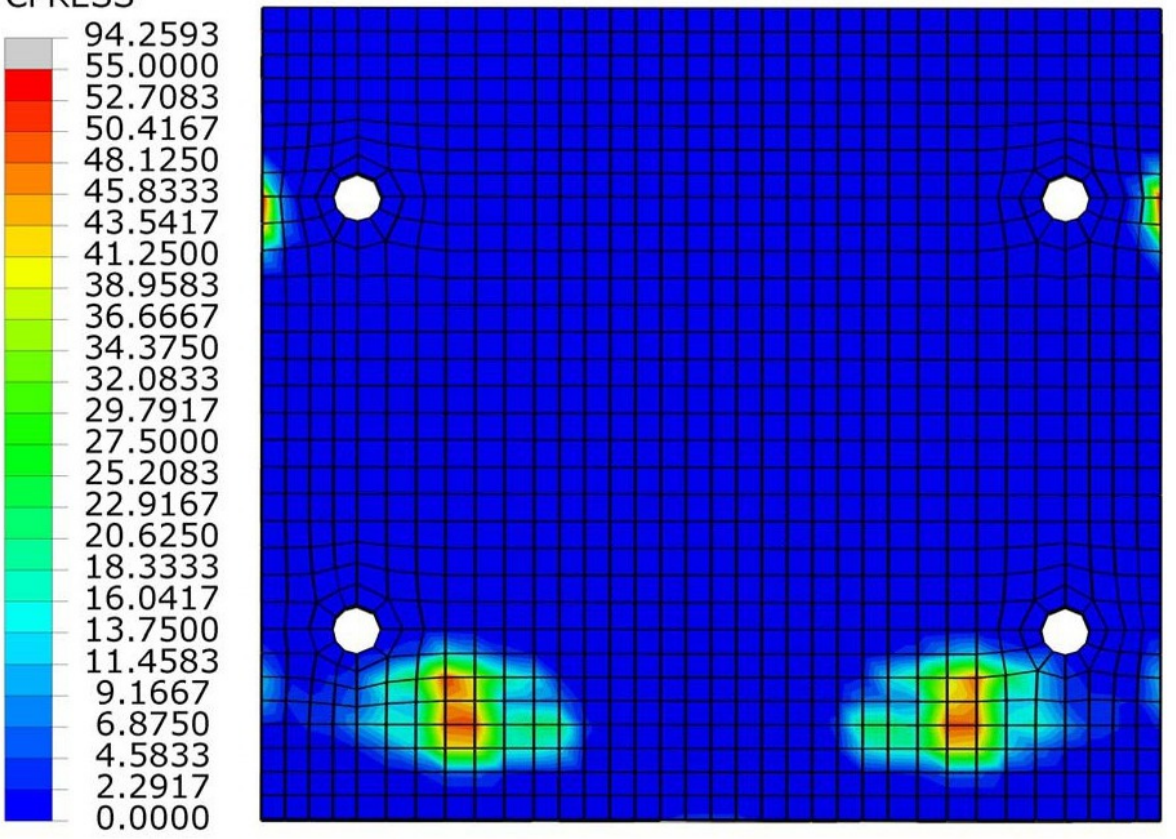
CPRESS
94.2593
55.0000
52.7083
50.4167
48.1250
45.8333
43.5417
41.2500
38.9583
36.6667
34.3750
32.0833
29.7917
27.5000
25.2083
22.9167
20.6250
18.3333
16.0417
13.7500
11.4583
9.1667
6.8750
4.5833
2.2917
0.0000

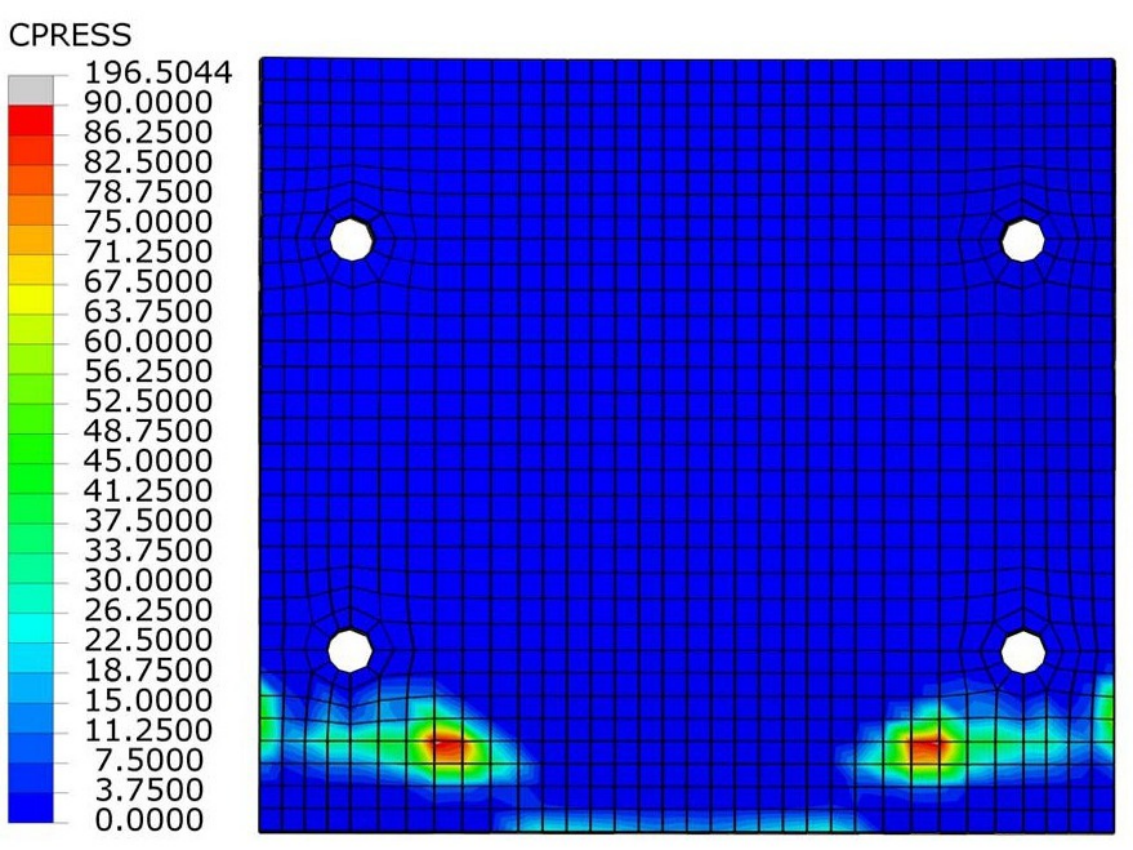
CPRESS
196.5044
90.0000
86.2500
82.5000
78.7500
75.0000
71.2500
67.5000
63.7500
60.0000
56.2500
52.5000
48.7500
45.0000
41.2500
37.5000
33.7500
30.0000
26.2500
22.5000
18.7500
15.0000
11.2500
7.5000
3.7500
0.0000

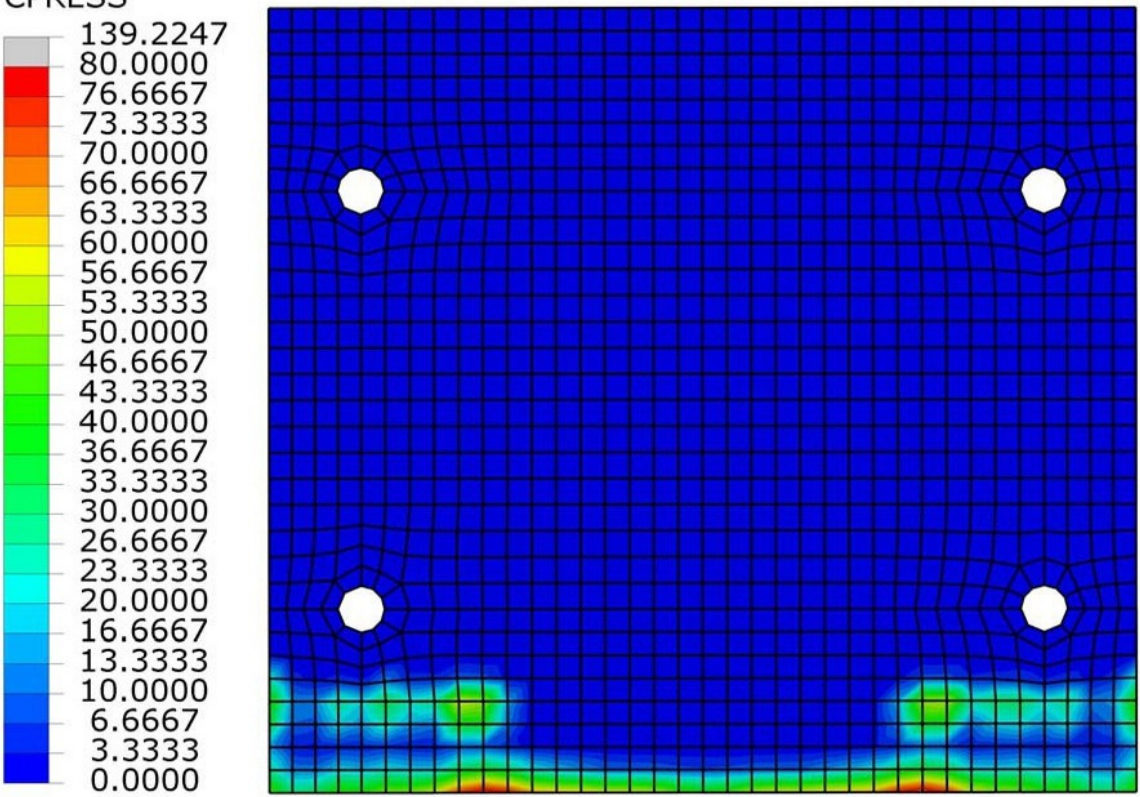
CPRESS
139.2247
80.0000
76.6667
73.3333
70.0000
66.6667
63.3333
60.0000
56.6667
53.3333
50.0000
46.6667
43.3333
40.0000
36.6667
33.3333
30.0000
26.6667
23.3333
20.0000
16.6667
13.3333
10.0000
6.6667
3.3333
0.0000

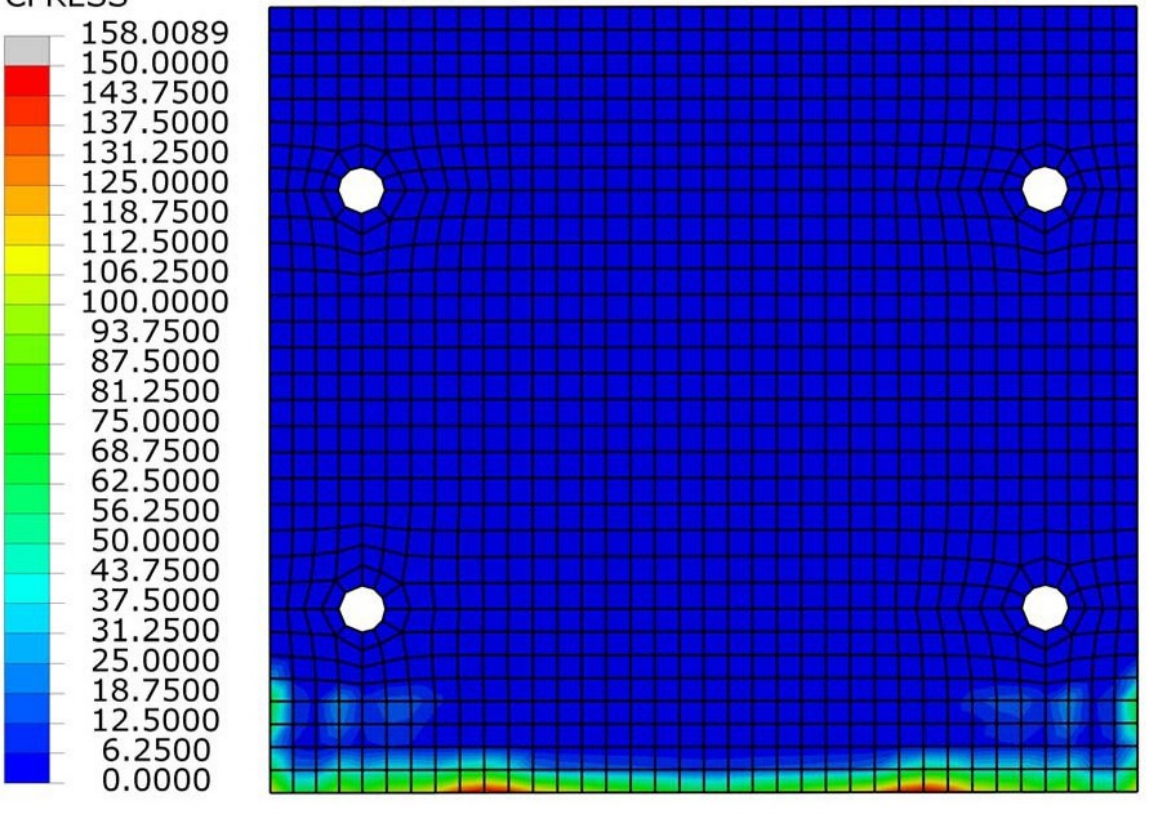
CPRESS
158.0089
150.0000
143.7500
137.5000
131.2500
125.0000
118.7500
112.5000
106.2500
100.0000
93.7500
87.5000
81.2500
75.0000
68.7500
62.5000
56.2500
50.0000
43.7500
37.5000
31.2500
25.0000
18.7500
12.5000
6.2500
0.0000

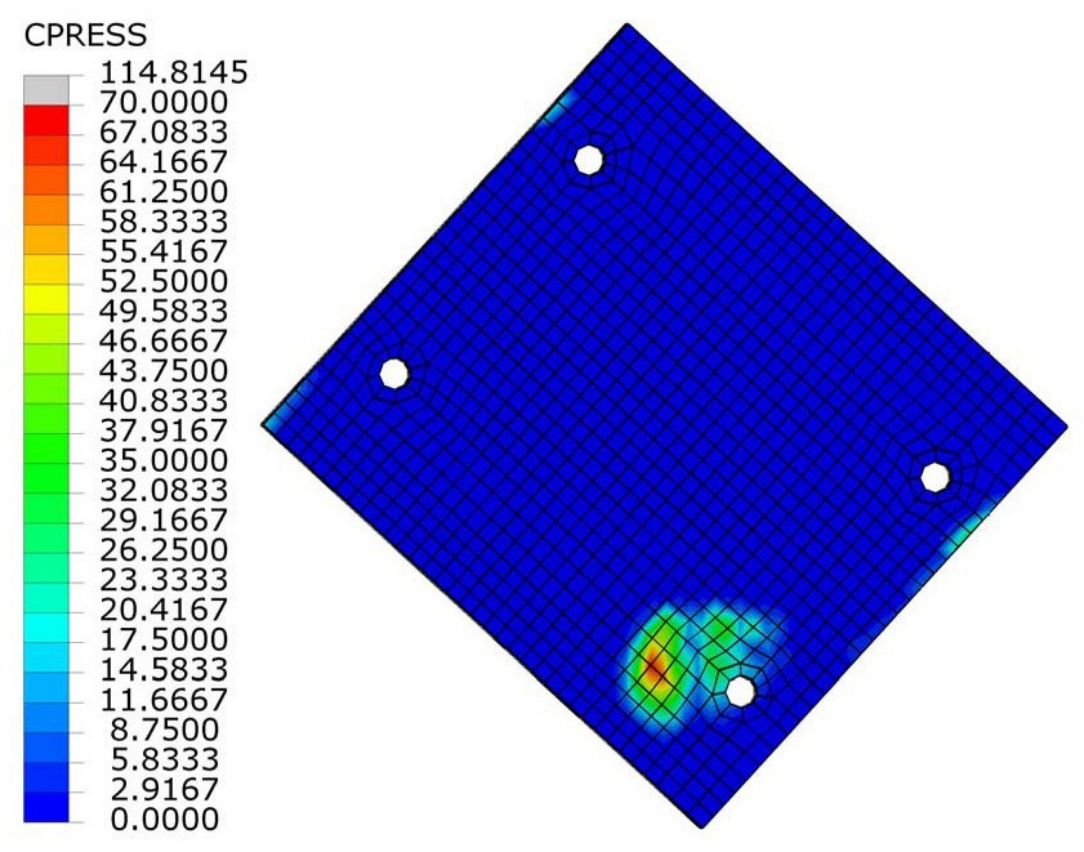
CPRESS
114.8145
70.0000
67.0833
64.1667
61.2500
58.3333
55.4167
52.5000
49.5833
46.6667
43.7500
40.8333
37.9167
35.0000
32.0833
29.1667
26.2500
23.3333
20.4167
17.5000
14.5833
11.6667
8.7500
5.8333
2.9167
0.0000

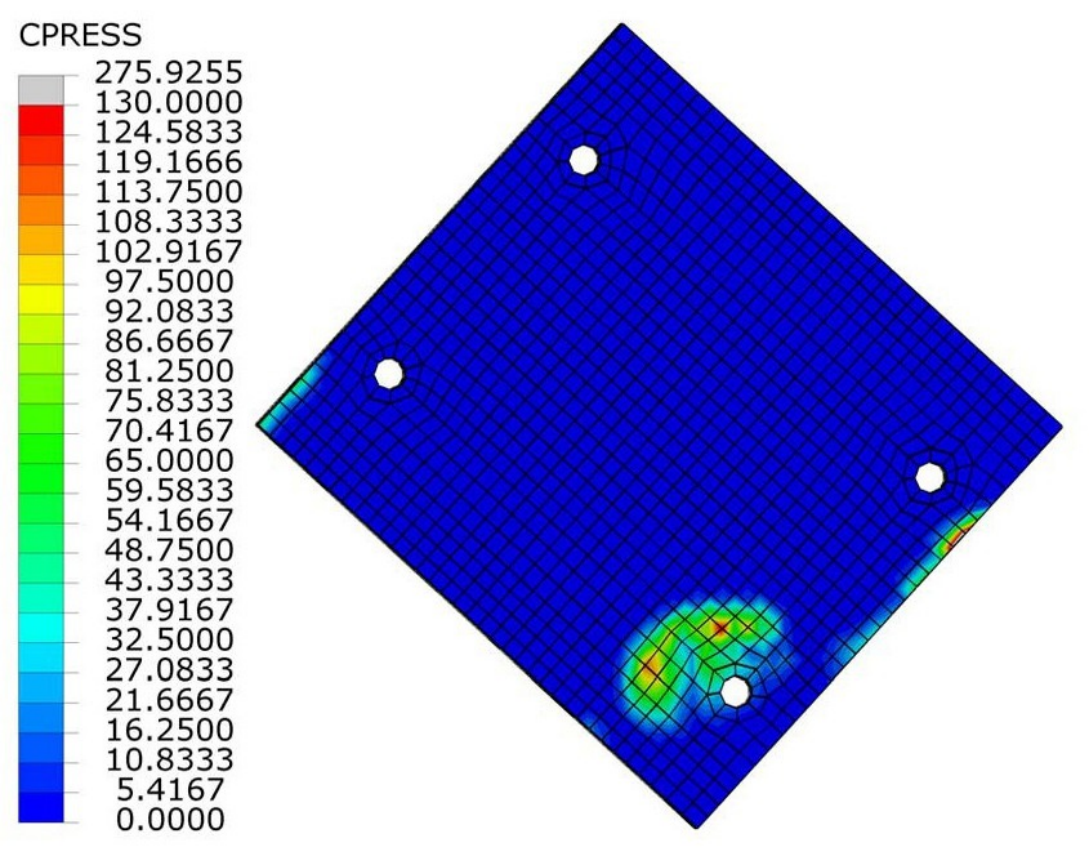
CPRESS
275.9255
130.0000
124.5833
119.1666
113.7500
108.3333
102.9167
97.5000
92.0833
86.6667
81.2500
75.8333
70.4167
65.0000
59.5833
54.1667
48.7500
43.3333
37.9167
32.5000
27.0833
21.6667
16.2500
10.8333
5.4167
0.0000

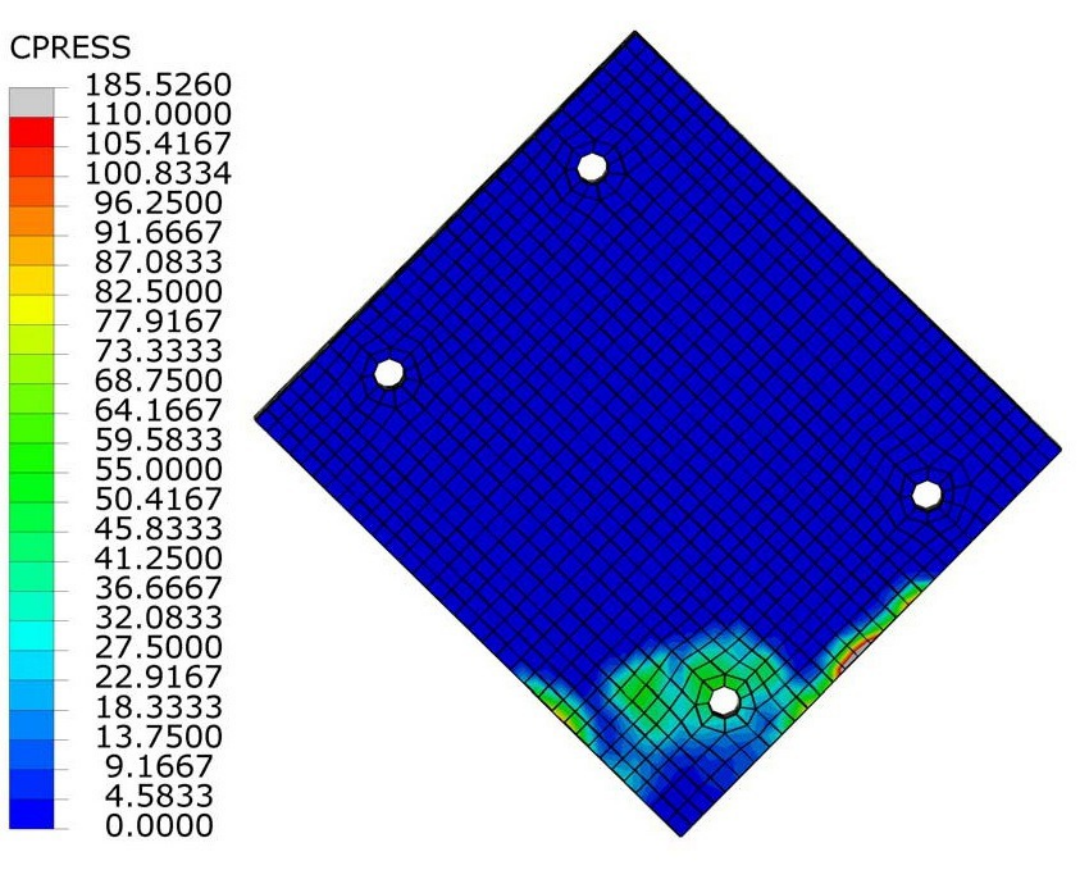
CPRESS
185.5260
110.0000
105.4167
100.8334
96.2500
91.6667
87.0833
82.5000
77.9167
73.3333
68.7500
64.1667
59.5833
55.0000
50.4167
45.8333
41.2500
36.6667
32.0833
27.5000
22.9167
18.3333
13.7500
9.1667
4.5833
0.0000

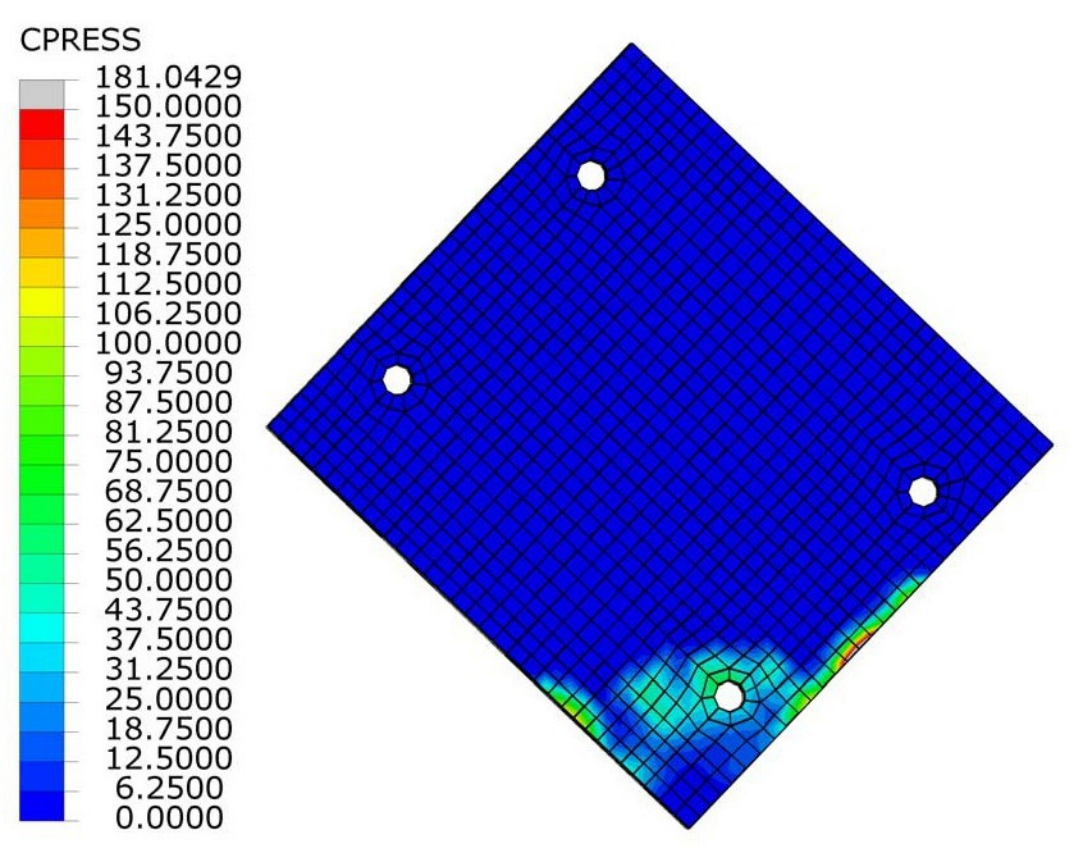
CPRESS
181.0429
150.0000
143.7500
137.5000
131.2500
125.0000
118.7500
112.5000
106.2500
100.0000
93.7500
87.5000
81.2500
75.0000
68.7500
62.5000
56.2500
50.0000
43.7500
37.5000
31.2500
25.0000
18.7500
12.5000
6.2500
0.0000

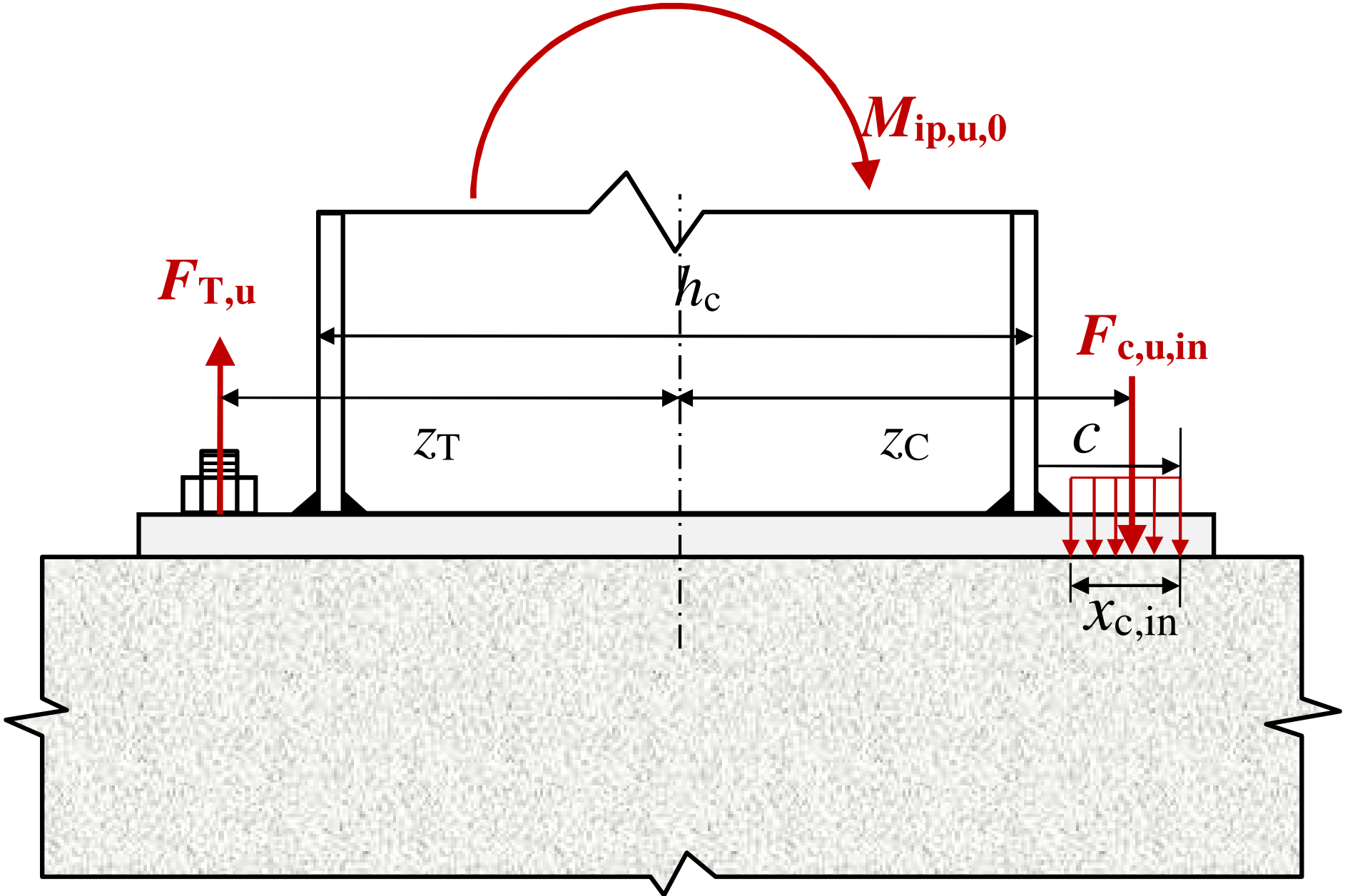
$M_{ip,u,0}$
$F_{T,u}$
h_c
$F_{c,u,in}$
z_T
z_C
c
$x_{c,in}$

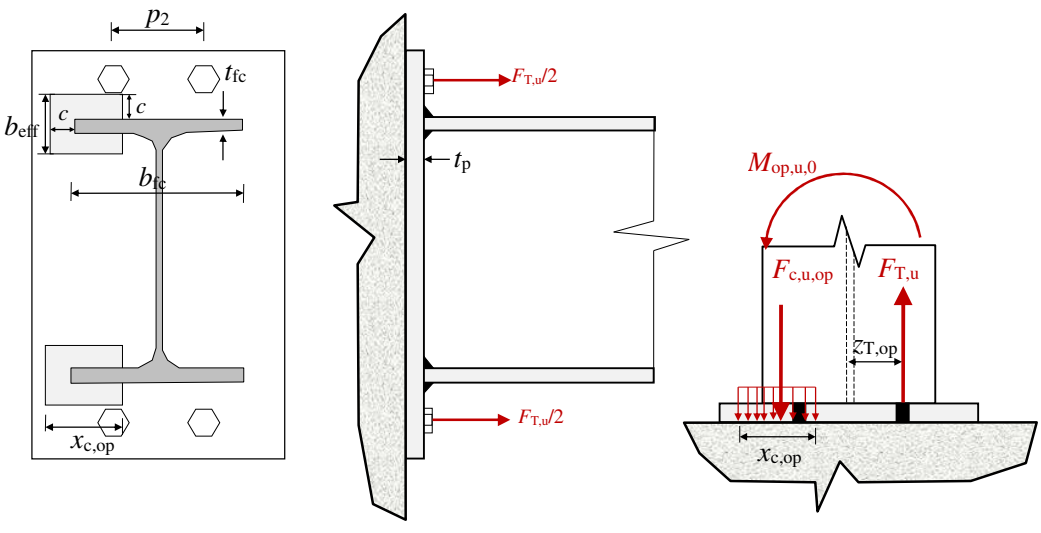
p_2
t_{fc}
c
c
b_{eff}
b_{fc}
$x_{c,op}$
$F_{T,u}/2$
t_p
$F_{T,u}/2$
$M_{op,u,0}$
$F_{c,u,op}$
$F_{T,u}$
$z_{T,op}$
$x_{c,op}$

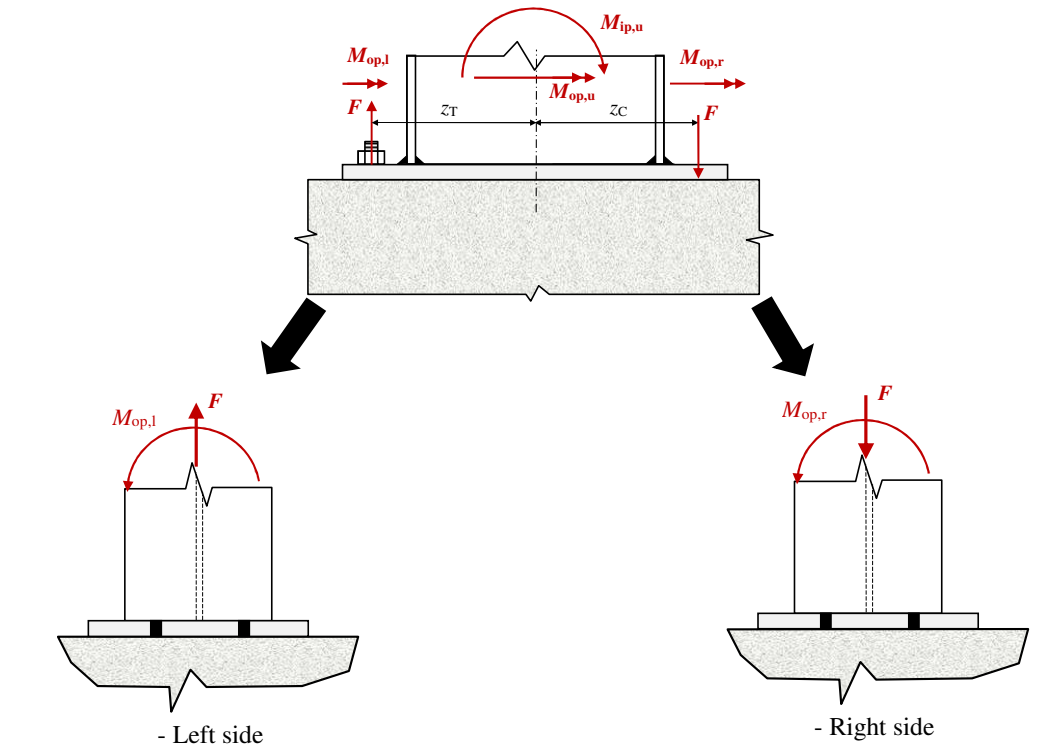

- Left side

- Right side

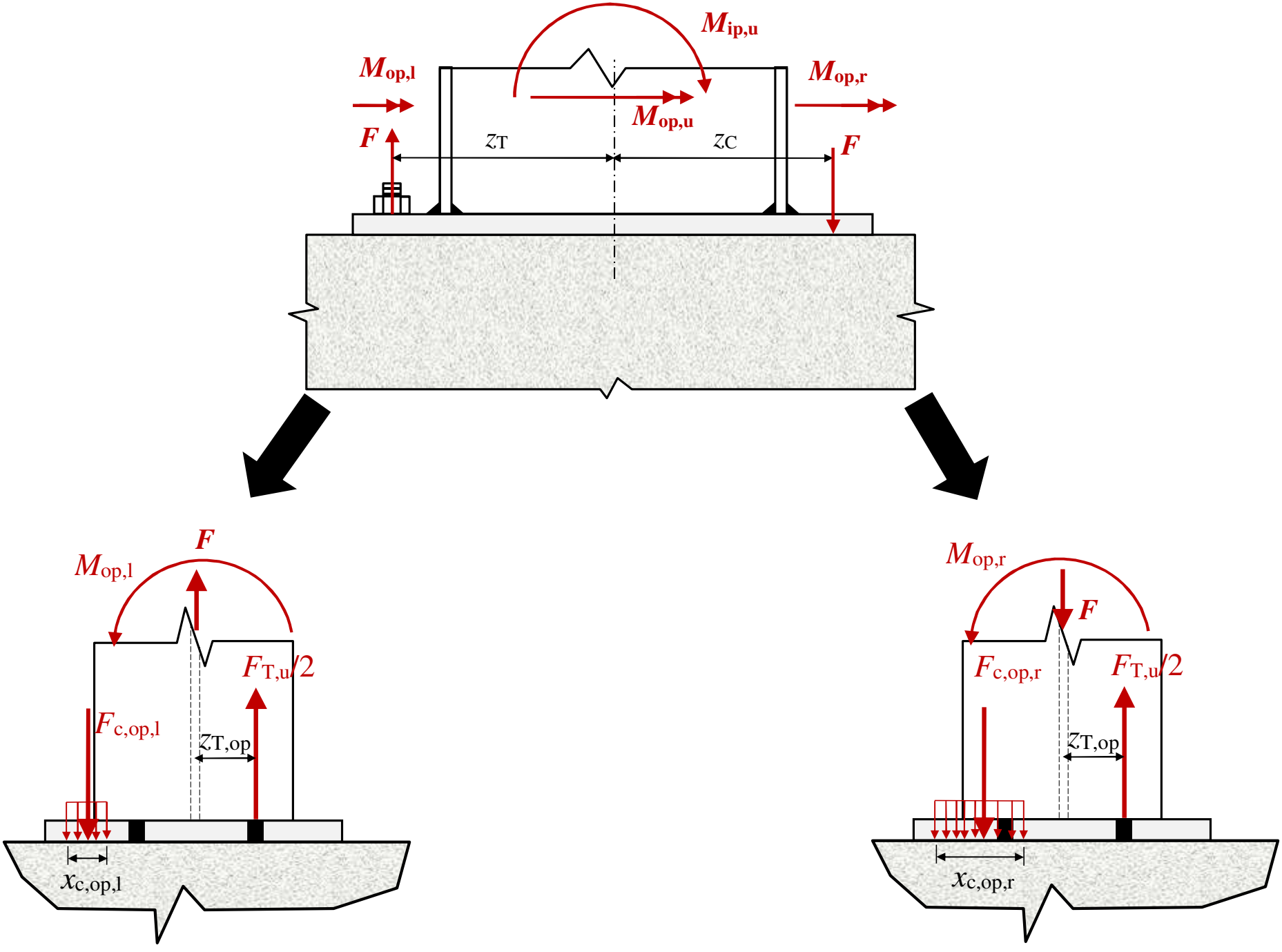
$M_{ip,u}$
$M_{op,l}$
$M_{op,r}$
$M_{op,u}$
F
F
z_T
z_C
F
$M_{op,l}$
$F_{T,u}/2$
$F_{c,op,l}$
$z_{T,op}$
$x_{c,op,l}$
$M_{op,r}$
F
$F_{c,op,r}$
$F_{T,u}/2$
$z_{T,op}$
$x_{c,op,r}$

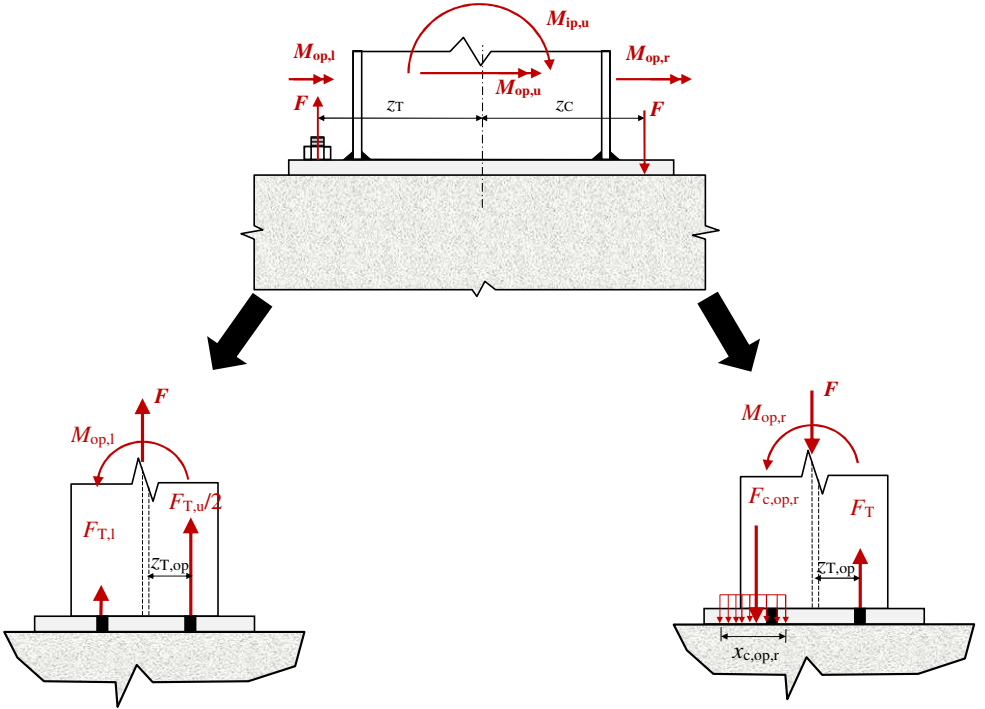
$M_{ip,u}$
$M_{op,l}$
$M_{op,r}$
$M_{op,u}$
F
z_T
z_C
F
F
$M_{op,l}$
$F_{T,u}/2$
$F_{T,l}$
$z_{T,op}$
F
$M_{op,r}$
$F_{c,op,r}$
F_T
$z_{T,op}$
$x_{c,op,r}$

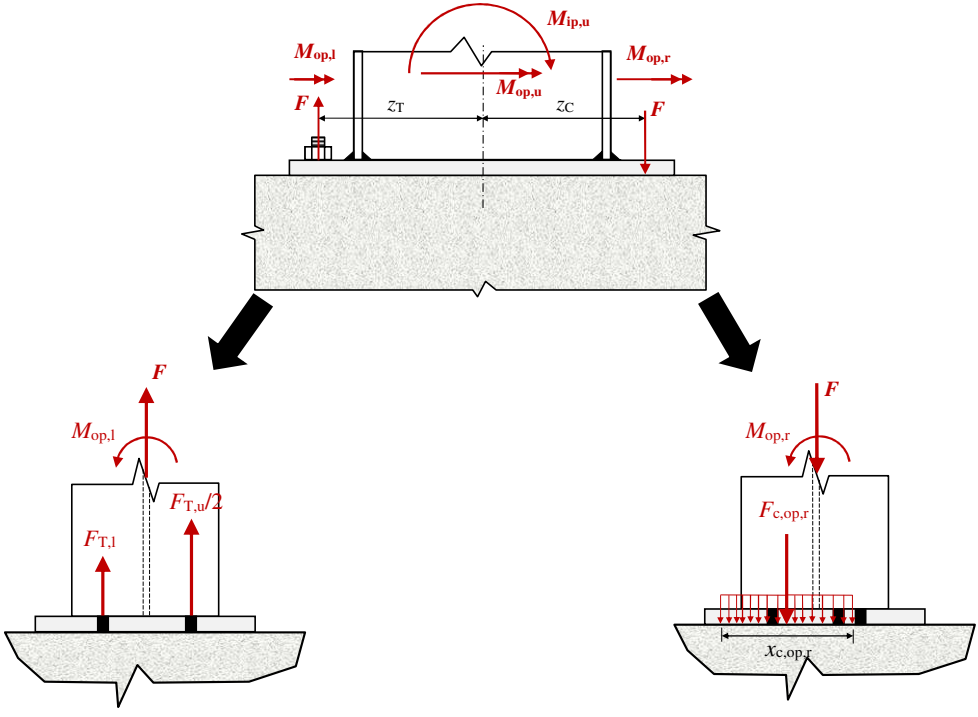
$M_{ip,u}$
$M_{op,l}$
$M_{op,r}$
$M_{op,u}$
F
z_T
z_C
F
F
$M_{op,l}$
$F_{T,u}/2$
$F_{T,l}$
F
$M_{op,r}$
$F_{c,op,r}$
$x_{c,op,r}$

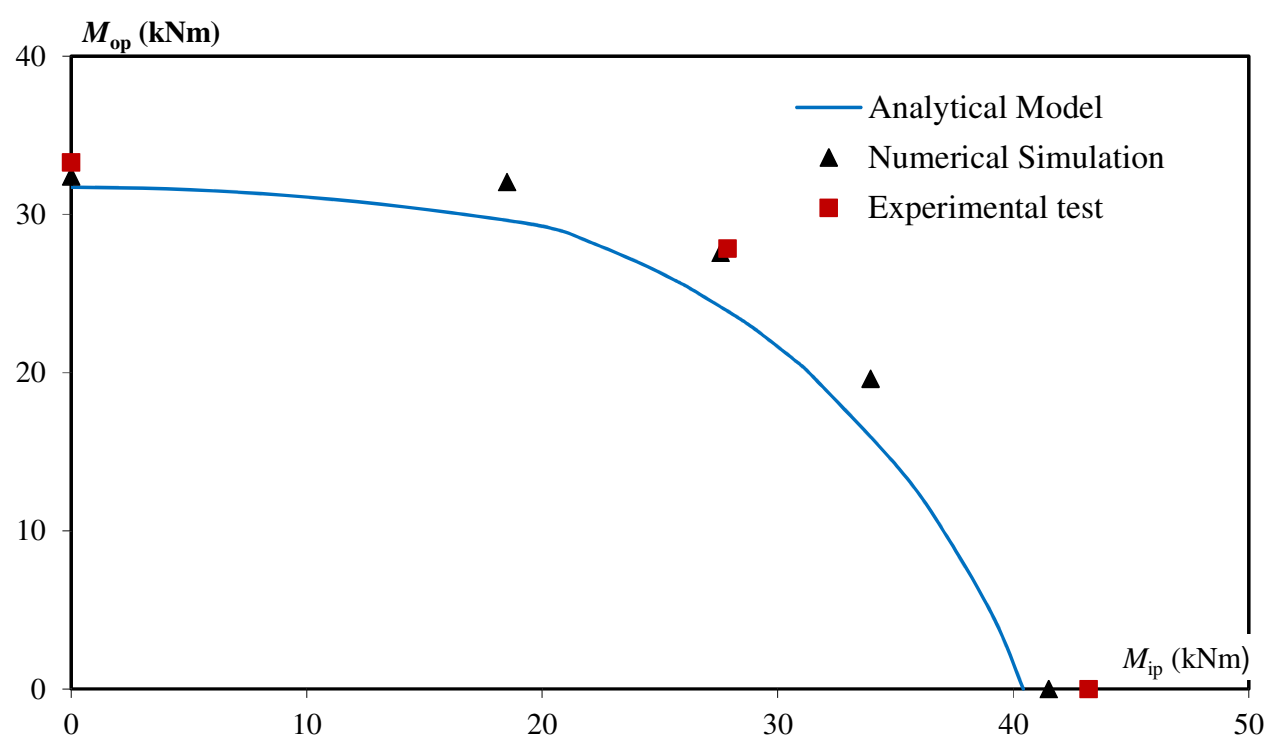
M_{op} (kNm)
40
30
20
10
0
0
10
20
30
40
50
M_{ip} (kNm)
Analytical Model
Numerical Simulation
Experimental test

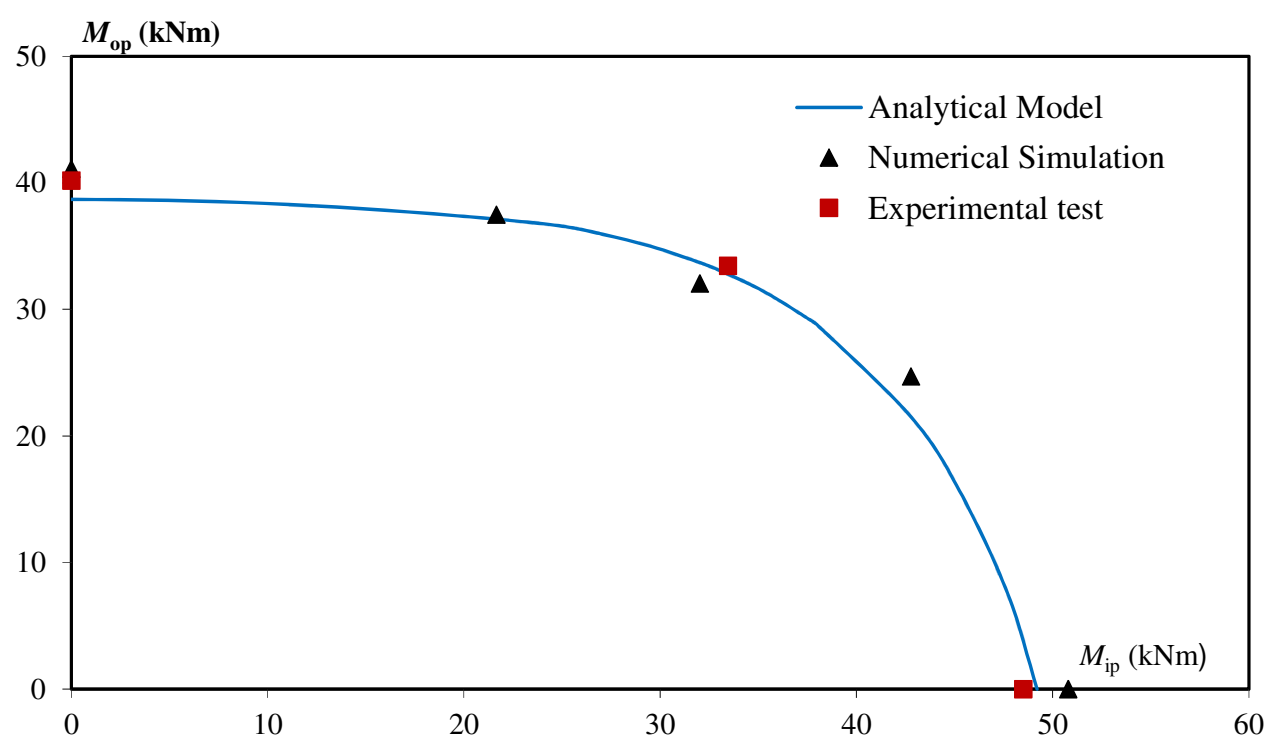
M_{op} (kNm)
50
40
30
20
10
0
0
10
20
30
40
50
60
M_{ip} (kNm)
Analytical Model
Numerical Simulation
Experimental test